Author:
Gregorie, Alice E

Title:
Resolution of channel movement underlying opening and closing of hERG1a potassium channels

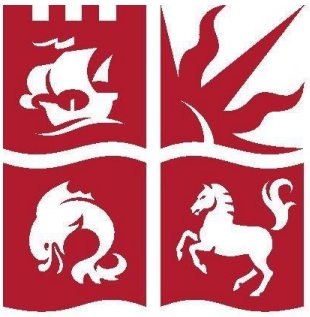

University of BRISTOL

Resolution of channel movement underlying opening and closing of hERG1a potassium channels

Alice Gregorie

A dissertation submitted to the University of Bristol in accordance with the requirements for award of the degree of MSc by Research in Physiology and Pharmacology in the Faculty of Life Sciences and the school of School of Physiology, Pharmacology and Neuroscience

September 2019

Word Count: 26,061

Abstract

The hERG1a potassium channel is a voltage-gated potassium channel which underlies the fast inwardly rectifying current in the cardiac action potential. The channel's voltage sensing domain (the S4 helix) contains positively charged residues which enable it's movement in response to membrane depolarisation to open the channel. The neutralisation of R528, one of the positive S4 residues, should alter S4 movement and therefore the gating currents used to record said movement.

Whole-cell voltage clamp was used to characterise the ionic and gating current of WT-hERG1a and R528C-hERG1a, and the gating currents of the N588K-hERG1a inactivation-deficient mutant when transiently expressed in mammalian tsA201 cells. The voltage-dependence of R528C-hERG1a activation and inactivation was positively shifted relative to WT-hERG1a current, reflecting the loss of a positively charged S4 residue. R528C-hERG1a current had accelerated activation and inactivation kinetics but slower deactivation kinetics, indicating that the mutation had destabilised the deactivated state of the S4 helix and accelerated its movement into the activated state. The reversal potential of R528C-hERG1a was also positively shifted, reflecting the ~1.5-fold increase in the P_{Na}/P_K ratio of the mutant, providing evidence of an interaction between S4 movement and the channel's selectivity filter.

The majority of WT-hERG1a gating currents were classed as asymmetric with the on gating current being of smaller amplitude than the off, while the majority of R528C-hERG1a and N588K-hERG1a gating currents were classed as symmetric. This was attributed to WT-hERG1a channels opening slowly over the pulse resulting in a smaller on gating current, in contrast to the fast activation of R528C-hERG1a and N588K-hERG1a which resulted in a larger initial on gating current.

Atomic Force Microscopy was used to image a tetrameric structure on the fixed cell membrane of the hERG-HEK293 stable cell line, which was believed to be the extracellular structure of the hERG channel in its native conformation.

Abstract word count: 300

I would like to thank Professor Neil Marrion for his supervision, support and cricket updates throughout the year, his guidance has been invaluable throughout this project. I would also like to thank Professor Mervyn Miles and Dr. Rob Harniman for their help with AFM imaging despite the many problems which had to be overcome. Thank you to Dr. Kevin Wilkinson and Karolina Talandyte for their molecular biology expertise and to Dr. Chris Dempsey for providing insights and figures regarding the structure of hERG. I'd also like to thank Professor Jules Hancox and Professor David Sheppard for their advice throughout the project.

I'd like to thank the friends who found themselves in Bristol for a fourth year, their reminders that an infected flask of cells is not the end of the world has been much appreciated. Finally, thank you to my family for their unwavering support, I promise I'll get a job eventually.

Author’s declaration

I declare that the work in this dissertation was carried out in accordance with the requirements of the University's Regulations and Code of Practice for Research Degree Programmes and that it has not been submitted for any other academic award. Except where indicated by specific reference in the text, the work is the candidate's own work. Work done in collaboration with, or with the assistance of, others, is indicated as such. Any views expressed in the dissertation are those of the author.

SIGNED: ..... DATE: .....

Table of Contents

List of figures

List of tables

List of abbreviations

A_f	Total current fitted by τ_f of deactivation
A_s	Total current fitted by τ_s of deactivation
AFM	Atomic Force Microscopy
ANOVA	Analysis of Variance
C	Cysteine residue
°C	Degrees Celsius
Ca^{2+}	Calcium ions
CNBD	Cyclic Nucleotide Binding Domain
CNBHD	Cyclic Nucleotide Binding Homology Domain
CNG	Cyclic Nucleotide Gated
Cryo-EM	Cryo-electron Microscopy
D	Aspartic acid residue
dH_2O	Deionized water
ddH_2O	Double-distilled water
DMEM	Dulbecco's Minimum Essential Medium with Glutamax-1
eag	ether-à-go-go
eGFP	Enhanced Green Fluorescent Protein
EGTA	Ethylene glycol-bis(2-aminoethylether)-N,N,N′,N′-tetraacetic Acid
ErgTx1	Ergtoxin 1
E_{Rev}	Reversal Potential
F	Phenylalanine residue
FBS	Foetal Bovine Serum
FM-AFM	Frequency-Modulation AFM
H	Histidine residue
HCN	Hyperpolarisation-activated Cyclic Nucleotide-gated
HEK 293 cell	Human Embryonic Kidney 293 cells
hERG	Human *ether-à-go-go-related* gene
HS-AFM	High Speed-AFM
I	Isoleucine residue
iGluRs	Ionic glutamate receptors
I_{hERG}	hERG current
I_{Kr}	Rapid delayed rectifier K^+ current
I-V relation	Current-Voltage Relation
K	Lysine residue
K^+	Potassium ion
k	Slope factor
KCNH2	Potassium voltage-gated channel subfamily H member 2
kHz	kilohertz
K_V channel	Voltage-Gated Potassium Channel
LB	Lysogeny Broth
LQTS	Long QT Syndrome
m	milli ($x10^{-3}$)
MiRP1	MinK-related peptide 1
mg	milligram
mL	millilitre
mM	millimole.$^{-1}$
mm	millimetre
ms	millisecond
mV	millivolt
MT	3-(4,5-dimethylthiazol-2-yl)-5-(3-carboxymethoxyphenyl)-2-(4-sulfophenyl)-2H-tetrazolium

MTSET	2-(Trimethylammonium)ethyl methanethiosulfonate
Na^+	Sodium ion
N	Asparagine residue
n	nano ($x10^{-9}$)
ng	nanogram
nm	nanometre
NMDG	N-Methyl-D-Glucamine
p	pico ($x10^{-12}$)
PAS domain	Per-Arnt-Sim domain
PBS	Phosphate Buffered Saline
pCMBS	p-Chloromercuribenzenesulfonate
PCR	Polymerase Chain Reaction
PEI	Polyethylenimine
pH	$-Log_{10}$ (H^+ concentration)
P/S	Penicillin/Streptomycin
Q	Glutamine residue
R	Arginine residue
RPM	Revolutions per minute
RMS	Root Mean Squared
SCA	Sudden Cardiac Arrest
SEM	Standard Error of the Mean
SOC	Super Optimal broth with Catabolite repression
SQTS	Short QT Syndrome
T	Threonine residue
τ	Time constant
τ_f	Fast time constant
τ_s	Slow time constant
TEA	Tetraethylammonium
TRPP2	TRP channel polycystin-2
µ	micro ($x10^{-6}$)
µL	microlitre
µm	micrometre
$V_{0.5}$	Half-maximal voltage
V_m	Membrane Voltage
VCF	Voltage-Clamp Fluorimetry
VSD	Voltage-sensing domain
W	Tryptophan residue
WT	Wild type
Y	Tyrosine residue

1. Introduction

1.1 The hERG potassium ion channel

The human *ether-à-go-go related gene* (HERG, or alternatively *KCNH2*) encodes the pore-forming α subunit of the hERG potassium channel (protein name $K_V11.1$) (Vandenberg et al., 2012). The most notable function of hERG is as a delayed rectifier potassium channel in the heart where it is vital in the repolarisation of the cardiac action potential (Vandenberg et al., 2001).

It must be noted that hERG is also expressed in smooth muscle, neuroendocrine cells and neurones under normal physiological conditions and overexpressed in the plasma membranes of cancer cells, where it is believed to regulate some aspects of neoplastic progression such as cell proliferation and cancer metastasis (Warmke et al., 1994; Chiesa et al., 1997; M Smith et al., 2002; Farrelly et al., 2003; Arcangeli and Becchetti, 2017). However, hERG is highly expressed in cardiac myocytes and it is here where its role and pathologies arising from its mutation, are most studied and understood (Sanguinetti and Tristani-Firouzi, 2006).

1.2 hERG channel structure

Like other voltage-gated potassium (K_V) channels, hERG is a tetrameric channel with 6 α-helical transmembrane domains (S1-S6) in each subunit, with four subunits coming together to form the central pore domain. S1-S4 are believed to form the voltage-sensing domain (VSD) while S5-S6 form the pore domain (Subbiah et al., 2004; Vandenberg et al., 2012). The K^+ selectivity filter on the extracellular side of the pore has the residue sequence Ser-Val-Gly-Phe-Gly (SVGFG), in contrast to Thr-Val-Gly-Tyr-Gly (TVGYG) found in most K_v channels (Gravel et al., 2013). Despite this K^+ selectivity filter hERG is not fully selective for potassium and does conduct Na^+ ions at a $p_K : p_{Na} > 100:1$ ratio (Morais-Cabral et al., 2001; Ceccarini et al., 2012; Vandenberg et al., 2012).

hERG, being a large 1,159 amino acid protein, has extensive intracellular amino-terminal and carboxy-terminal domains. The COOH terminus of each subunit contains a cyclic nucleotide-binding homology domain (CNBHD), similar to the cyclic-nucleotide-binding domain (CNBD) found in hyperpolarisation-activated cyclic nucleotide-regulated and cyclic nucleotide-gated channels (HCN and CNG channels, respectively). Despite the CNBHD, hERG channels are not activated by the binding of cyclic nucleotides. (Tammaro et al., 2008; Li et al., 2016).

The NH_2 terminus of hERG subunits contains a Per-Arnt-Sim (PAS) domain which is considered to be a defining characteristic of the *ether-à-go-go (eag)* subfamily of K_V channels and is believed to have some regulatory function on the channel (Warmke et al., 1994; Morais Cabral et al., 1998; Sanguinetti and Tristani-Firouzi, 2006; Vandenberg et al., 2012). Interactions between the PAS domain and the CNBHD are related to channel deactivation (see section 1.3.2) and may be modulated by an 'intrinsic ligand' residue sequence found proximal to the CNBHD (Codding and Trudeau, 2019).

Until recently the crystal structure of hERG was not known. Instead the amino acid sequence of hERG was mapped onto the crystal structure of bacterial K_V channels, but given differences between hERG and most K_V channels such as pharmacology and gating kinetics there were limitations to this methodology. In 2017 W. Wang and R. MacKinnon used cryo-electron microscopy (cryo-EM) to obtain the molecular structure of a truncated form of hERG (deletion of large, flexible amino acid sequences at positions 141-350 and 871-1005 enabled imaging) (see figure 1-1). This proved the similarities between hERG and other K_V channels, but likewise proved that there were as many structural differences such as hydrophobic pockets within the central cavity (theorised to be related to drug binding), the movement of S4 and S5 and changes in the selectivity filter structure (Wang and MacKinnon, 2017). Obtaining the cryo-EM structure is a substantial achievement in the field, and though it represents only one conformation of the channel it has enabled extensive research into hERG channel structure.

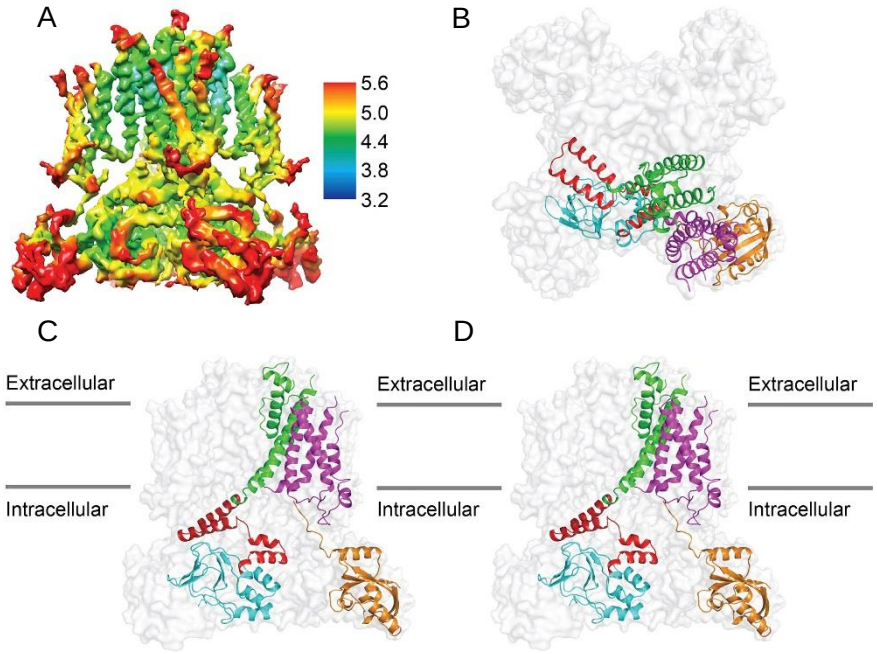

Figure 1-1. The structure of hERG obtained using cryo-EM, with *A* being a density map and *B, C and D* showing the α helix of each domain. Red represents the C-linker, green the pore domain, purple the VSD, orange the NH_2 terminus and blue the CNBHD in the COOH terminus. Adapted from Wang and MacKinnon, 2017.

hERG is known to have 3 isoforms (1a, 1b and 3.1) resulting from three different transcription initiation sites. hERG1a is the primary isoform found expressed in cardiac myocytes while

hERG1b and 3.1 are expressed at much lower levels. hERG1a and 1b have been found to form heterotetramers in cardiac tissue which alters the sensitivity of the channel to various pharmacological compounds as well as oxidative stress, thyrotropin releasing hormone and cyclic guanosine monophosphate (cGMP) (Vandenberg et al., 2012; Perissinotti et al., 2018).

hERG is known to interact with accessory β subunits such as KCNE1/MinK and KCNE2/MiRP1 (MinK-related protein 1). Accessory subunits have been shown modulate I_{hERG} (current conducted by the hERG channel) kinetics, voltage dependence, current density through modulation of channel degradation, single channel conductance and the channel's response to some pharmacological compounds (Vandenberg et al., 2001, 2012; Anantharam and Abbott, 2005; Zhang et al., 2012). Though relevant, especially when looking at clinical samples, for the purposes of this master's project only hERG1a as a homotetramer with no auxiliary subunits will be characterised.

1.3 hERG gating kinetics

The hERG channel has unusual gating kinetics compared with those of other voltage-gated channels. Firstly, the activation and deactivation transitions are considerably slower, reputedly taking place over hundreds of milliseconds whereas in *Shaker* potassium channels the same transition occurs over a fraction of that time (Bezanilla et al., 1994a; Sanguinetti et al., 1995b; Sanguinetti and Tristani-Firouzi, 2006; Cheng and Claydon, 2012).

Secondly, transition of the channel into the non-conducting inactivated state is rapid (occurring over tens of milliseconds) and voltage dependent, while the same applies to its transition out of the inactivated state (see figure 1-2). This rapid inactivation gives rise to hERG's characteristic inward rectification; as the membrane potential becomes more depolarised the amplitude of I_{hERG} decreases (Sanguinetti et al., 1995b; Vandenberg et al., 2001, 2012; Cheng and Claydon, 2012). These transitions between closed, open and inactivated are believed to proceed in a linear manner, as seen in figure 1-2. Therefore to inactivate the channel must first

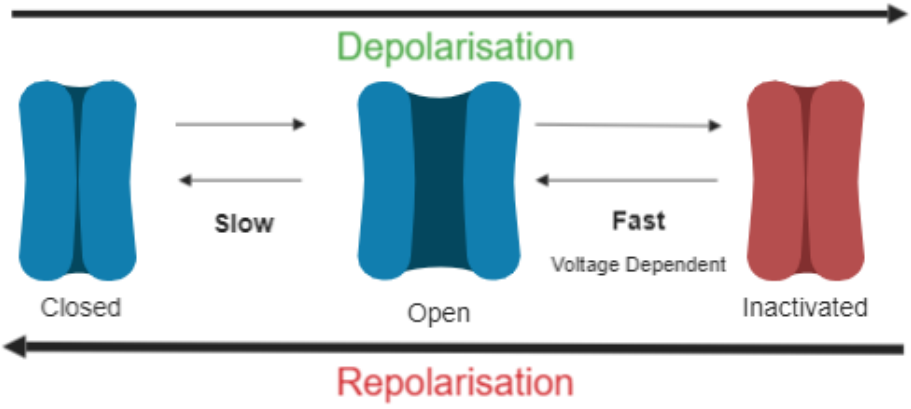

Figure 1-2. The unusual gating kinetics of hERG. Activation and deactivation transitions are slow, but the transition into and recovery from inactivation are rapid and voltage dependent.

be opened by depolarisation and cannot proceed to the inactivated state directly from the closed state (Bett et al., 2011b).

These kinetics give rise to the characteristic hERG 'tail currents' seen upon repolarisation. During a depolarising pulse channels will slowly open and then rapidly inactivate resulting in little current being conducted. Upon repolarisation the recovery from inactivation occurs much faster than the transition into the deactivated state, resulting in a brief large-amplitude current known as a tail current, see figure 1-3 (Zhou et al., 1998; Vandenberg et al., 2001; Cheng and Claydon, 2012).

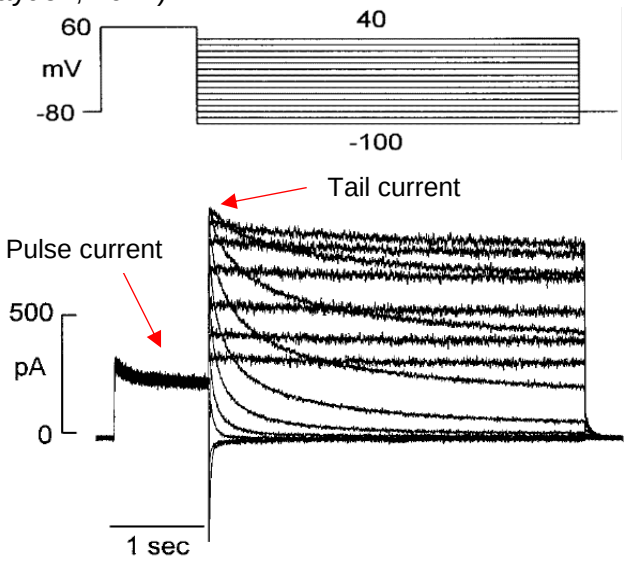

Figure 1-3. hERG pulse current is elicited by a depolarising pulse (see voltage protocol) which opens and then inactivates channels, resulting in the 'pulse current'. Channels then quickly recover from inactivation upon repolarisation, resulting in tail currents being recorded before the channels inactivate. Adapted from Zhou et al., 1998.

1.3.1 The activation and deactivation of hERG

Activation and deactivation of the hERG channel occur as a result movement of the S4 voltage sensor in response to changes in membrane voltage. This is hypothesised to put strain upon the S4-S5 linker which in turn causes the activation gate, reportedly the S6 transmembrane helix, to move and therefore opening of the channel (see figure 1-4) (Tristani-Firouzi et al., 2002; Vandenberg et al., 2012).

The S4 voltage sensor is an α helix with a positively charged residue (arginine or lysine) located every three amino acids. The diameter of the α helix results in the positively charged residues lining one side of the helix, creating an area of concentrated positive charge (Catterall, 2010). The positively charged S4 helix is repelled by membrane depolarisation and therefore moves out of the lipid bilayer, facilitating the opening of the channel. Through charge neutralisation studies and accessibility studies it was concluded that only the 3 outermost positive residues of the hERG1a S4 helix contribute to gating charge (lysine 525 and arginine 528 and 531). Arginine 534 and 537 and lysine 538 are considered to be embedded too deep within the membrane to contribute to gating charge (see figure 1-4) (Subbiah et al., 2004; Zhang et al., 2004).

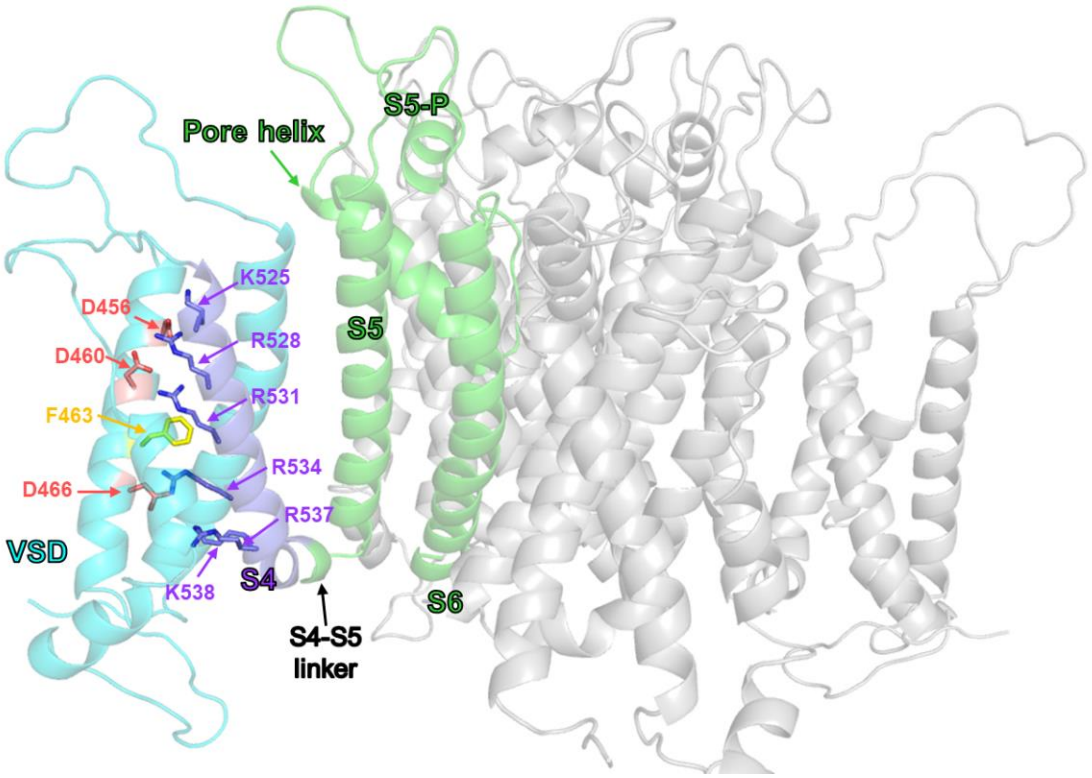

Figure 1-4. The transmembrane domain of the hERG1a channel based on the cryo-EM structure obtained by Wang and MacKinnon, 2017. Highlighted is one subunit of the tetramer for clarity, with the remaining three subunits shown in grey. The is VSD shown in blue (with labelled negative residues) with the S4 domain (and labelled positive residues) in purple and S5, S5-P, pore helix and S6 shown in green. Provided by Dr. Christopher Dempsey (University of Bristol).

The positive S4 residues also interact with negatively charged residues located in the S1-S3 domains. Mutations of residues such as aspartate at positions 456, 460 and 466 in S2 (see figure 1-4) and aspartate at 509 in S3 affected the voltage dependence and kinetics of hERG activation, leading to the conclusion that the residues form salt bridges with the positive residues in S4. The salt bridges aid stabilisation of S4 in either the up or down state and so in turn stabilise either the open or closed state of the channel (see figure 1-5) (Liu et al., 2003; Zhang et al., 2005; Vandenberg et al., 2012).

The slow activation kinetics of hERG are theorised to be due to either slow movement of the S4 voltage sensor or rate-limiting steps after S4 movement such as conformational changes of transmembrane domains and opening of the ion channel pore (Es-Salah-Lamoureux et al., 2010; Cheng and Claydon, 2012; Wang et al., 2013). Considerable research into hERG activation has taken place using a variety of techniques such as fluorescence, the rate of modification of gating currents by MTSET and the recording of gating currents in both oocytes and mammalian cells. A general theory is that while S4 voltage sensor movement is slow in

comparison to other K_V channels, there are also shifts in the conformation of cytosolic domains through multiple closed states before the channel pore can open, accounting for the slow activation rate (Cheng and Claydon, 2012; Wang et al., 2013; Goodchild et al., 2015; Dou et al., 2017).

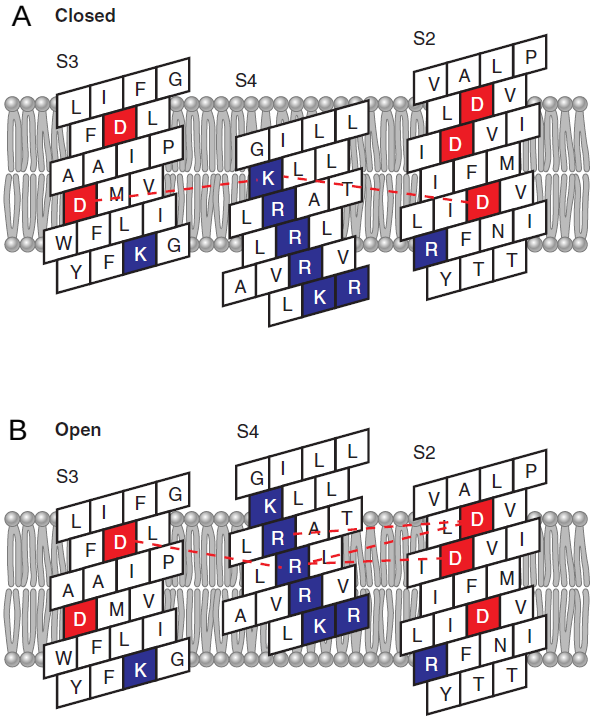

Figure 1-5. Positive residues in S4 form salt bridges with negative residues in S2 and S3. Theorised salt bridges are shown by red dotted lines and serve to stabilise S4 when it is in the closed (*A*) and open (*B*) state. Adapted from Vandenberg et al., 2012.

The slow deactivation kinetics of hERG are less understood but are known to be more complex than other K_V channels. Deletion of the amino-terminal PAS domain accelerates channel deactivation, which can then be slowed again through addition of a recombinant PAS domain (Morais Cabral et al., 1998; Gustina and Trudeau, 2009). Deletion of the carboxy-terminal CNBHD was found to also accelerate deactivation as did deletion of both the PAS domain together with the CNBHD. The accelerated deactivation kinetics from deletion of both domains were not slowed following addition of a recombinant PAS domain. This suggests that an interaction between the two cytosolic domains is essential for the slow deactivation seen in the hERG channel (Gustina and Trudeau, 2012).

1.3.2 The inactivation of hERG

K_V channels inactivate primarily by one of two mechanisms; C-type or N-type inactivation. N-type inactivation involves a 'ball and chain' mechanism, where residues from the NH_2 terminus occlude the pore of the ion channel to prevent conduction, while C-type inactivation is supposedly due to collapse of the selectivity filter which then occludes the conduction pathway (Hoshi et al., 1990; Bett et al., 2011a; Hoshi and Armstrong, 2013). C-type inactivation is slowed by the application of external TEA (tetraethylammonium); it is theorised that the binding

of TEA to the outer vestibule of the channel prevents the constriction of the selectivity filter and so delays C-type inactivation (Andalib et al., 2004; Subbiah et al., 2004). Application of external TEA slows hERG inactivation while deletion of the NH_2 terminus has no effect on the inactivation of the channel (Choi et al., 2011; Goodchild et al., 2015). Therefore hERG inactivation is thought to be analogous of C-type inactivation found in other K_V channels despite the difference in kinetics (Vandenberg et al., 2012).

The uniquely fast kinetics of hERG inactivation may be due to a difference in the GFG sequence of the selectivity filter relative to the GYG sequence found in other K_V channels. The F627 residue (of the GFG sequence) in hERG changes the position of the selectivity filter, whilst an inactivation deficient hERG mutant (S631A) was found to have a selectivity filter structure more closely resembling other K_V channels (Wang and MacKinnon, 2017). This led to the proposal that the fast inactivation of hERG may be due to this altered shape of the filter which could allow it to collapse at a faster rate.

Given that mutations at positions H587 and N588 in the S5-P linker both alter hERG channel inactivation and ionic selectivity, it could be assumed that the S5-P linker (also known as the turret region) has a role in channel inactivation through modulation of the selectivity filter (Jiang et al., 1999; McPate et al., 2005). It was proposed that upon upward movement of the S4 helix, the S5-P linker is shifted towards the pore, and therefore the selectivity filter. The ensuing interaction between the two domains can block the conduction of ions resulting in channel inactivation (Jiang et al., 2005). Furthermore, this would link the voltage sensing of activation to inactivation, suggesting a mechanism behind the apparent voltage sensitivity of inactivation. Mutations in the S5-P linker (such as N588K) alter the interaction of the linker with the selectivity filter, accounting for the differences in both ionic selectivity and channel inactivation seen in S5-P linker mutants (McPate et al., 2005; Colenso et al., 2013).

1.4 hERG and the cardiac action potential

In the cardiac action potential hERG is responsible for the rapid component of the delayed rectifier current (I_{Kr}) (Sanguinetti et al., 1995a; Trudeau et al., 1995). The unique gating kinetics of hERG allow it to perform its main physiological role of repolarising the cardiac action potential in cardiac myocytes (although it must be noted that many potassium channels are involved in this process) (Nerbonne and Kass, 2005). Upon depolarisation of the membrane by inward Na^+ current hERG channels slowly open and then rapidly transition into the inactivated state. As a result, little to no current is conducted by hERG channels, allowing the cardiac action potential to plateau and enter a phase of slow repolarisation (see figure 1-6).

This gives sufficient time for Ca^{2+} ions to enter myocytes, enabling efficient excitation-contraction coupling (Vandenberg et al., 2001; Sanguinetti and Tristani-Firouzi, 2006).

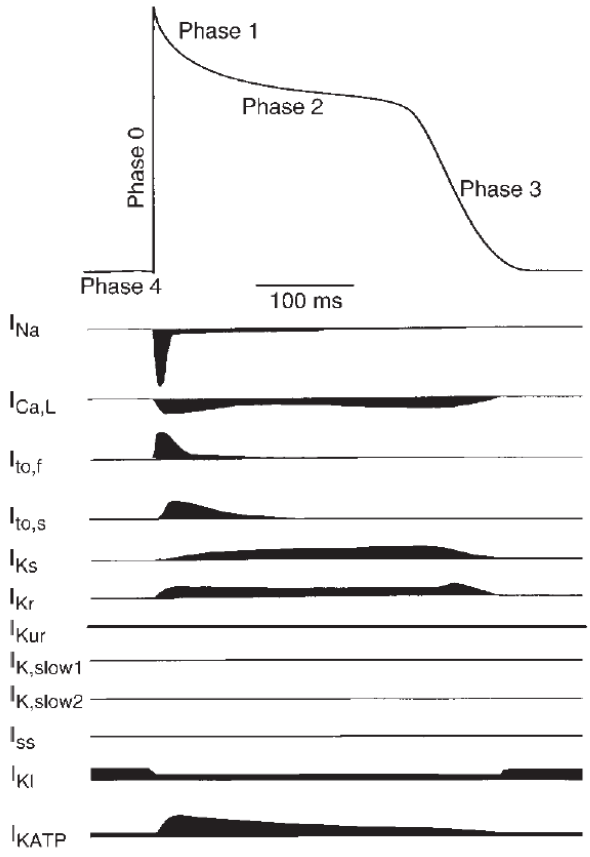

Figure 1-6. The ionic currents underlying the (ventricular) cardiac action potential. Many potassium currents are involved in the repolarisation phases, I_{Kr} (sixth from the top), the rapid delayed rectifying current is an outward potassium current conducted by the hERG channel. Adapted from Nerbonne and Kass, 2005.

Once the membrane potential has sufficiently repolarised hERG channels quickly transition out of inactivation into the conducting active state. The outward K^+ current repolarises the cell membrane which allows more hERG channels to open; this positive feedback loop enables fast repolarisation of cardiac myocytes. hERG channels then remain open for a period before slowly closing, but due to the decreasing K^+ driving force little current is conducted (Nerbonne and Kass, 2005).

The slow deactivation of hERG channels is also crucial for the suppression of premature beats which could lead to arrhythmia (Perrin et al., 2008). In the case of a premature stimulus the outward K^+ current will increase in amplitude due to channels remaining open and a larger K^+ driving force, but will quickly decay as a result of hERG inactivation. This large outward K^+ current opposes depolarisation of the cardiac myocytes preventing the propagation of premature beats and the ensuing arrhythmia (Sanguinetti and Tristani-Firouzi, 2006).

1.5 Clinical relevance of the hERG ion channel

1.5.1 hERG mutations lead to cardiac arrhythmia

Owing to the importance of the I_{Kr} current conducted by hERG, genetic mutations in the corresponding *KCNH2* gene can lead to serious ventricular arrhythmias and sudden cardiac arrest (SCA). Loss of function mutations where repolarisation is delayed due to defects in hERG channel synthesis, trafficking, gating (decreased activation or increased inactivation) or conductance result in an extended QT interval, known as Long QT Syndrome (LQTS) (Nerbonne and Kass, 2005). The QT interval is the time required for ventricular repolarisation within the duration of the surface electrocardiogram, and a QT interval greater than 440ms is considered to be indication of LQTS (Vandenberg et al., 2001).

Although 16 forms of congenital LQTS have been identified, LQTS due to mutations in *KCNH2* (LQTS type 2) is the second most common form, responsible for approximately 25-30% of cases (Giudicessi et al., 2018). Furthermore, within LQTS type 2 there will be phenotypic variations due to different point mutations within the gene (Vandenberg et al., 2012). Approximately 1 in every 2,500 live births will have some form of LQTS, although with proper diagnosis and treatment (usually a form of β-blocker) a patient's prognosis is generally promising (Crotti et al., 2008).

Inherited Short QT Syndrome (SQTS) as a result of hERG point mutations has a much lower occurrence compared with inherited LQTS, with only a few families identified worldwide (Brugada et al., 2004; Vandenberg et al., 2012). N588K and T618I mutations have been identified to cause SQTS and when characterised were found to be inactivation deficient at physiologically relevant potentials (McPate et al., 2005; Grunnet et al., 2008; El Harchi et al., 2012). As a consequence, when expressed in human cardiac myocytes the hERG mutants conduct more repolarising K^+ current during the plateau phase of the cardiac action potential, leading to its premature termination (Vandenberg et al., 2012).

1.5.2 Acquired LQTS

Pharmacological inhibition of hERG channels leading to a delay in ventricular repolarisation is also associated with ventricular arrhythmia and SCA and is referred to as acquired LQTS (aLQTS). A wide range of drugs of different classes and structures have been reported to inhibit hERG channels such as some psychoactive agents, antiarrhythmic agents, antimicrobials, the anti-histamine terfenadine and the gastrointestinal prokinetic cisapride (Vandenberg et al., 2001). The latter two drugs have been withdrawn from general sale due to the proarrhythmic risks far outweighing any benefit to the patient (Sanguinetti and Tristani-Firouzi, 2006).

The promiscuity of the hERG channel with its ability to bind to a wide variety of drugs, both cardiac and non-cardiac compounds, prompted legislation to come into effect which requires potential compounds to be screened for activity at the hERG channel at the preclinical stage (Sanguinetti and Tristani-Firouzi, 2006; Vandenberg et al., 2012). The origin of hERG's ability to bind to so many compounds is unclear, however its cryo-EM structure revealed the presence of four deep hydrophobic pockets together with a concentrated negative charge inside the central cavity of the channel. Both structures were suggested to contribute to the channel's ability to bind drugs (Wang and MacKinnon, 2017).

1.6 Aims of this master's project

In regards to electrophysiology, the aims of this project were:

- Characterise the ionic current of WT-hERG1a when expressed in a mammalian cell line.
- Produce the R528C-hERG1a mutant, which owing to its loss of a positively charged residue in the voltage sensor was likely to have an altered S4 movement upon channel activation and deactivation.
- Characterise the ionic current of R528C-hERG1a when expressed in a mammalian cell line and compare this with the WT channel.
- Record gating currents from WT-hERG1a, which would be representative of the charge movement of S4 upon channel activation and deactivation.
- Record gating currents from the R528C mutant to identify whether the loss of the charged residue was reflected by a change in the gating currents when compared with WT-hERG1a.
- Record gating currents from the inactivation-deficient mutant N588K-hERG1a to identify whether the loss of inactivation affected the gating currents.

The aims of AFM imaging were:

- Image WT-hERG1a while being expressed in a mammalian cell membrane. If it were possible to visualise the structure of the hERG channel, comparisons would be made between the structure of the channel in its activated and deactivated state.

2. Materials and methods

2.1 Molecular Biology

2.1.1 The hERG1a plasmid

The wild type (WT) hERG1a insert used the 'pcDNA3.0 L15' vector to carry the hERG1a cDNA sequence, which was inserted between HindIII and EcoRI restriction enzyme sites, see figure 2-1.

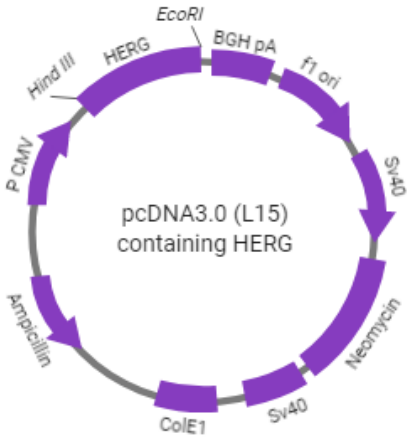

Figure 2-1. The hERG1a-containing pcDNA3.0 (L15) plasmid

The plasmid (kindly provided by Professor Jules Hancox of the University of Bristol) was amplified using transformation of DH5α E. coli bacteria. 20µL of thawed bacteria was incubated with 1µL plasmid for approximately 20 minutes in a 1mL Eppendorf tube left on ice. The solution was heat-shocked for 45 seconds in a water bath heated to 42°C and then returned to ice for a further 2 minutes. 80µL of SOC media (super optimal broth with catabolite repression; 0.5% yeast extract, 2% tryptone, 10mM NaCl, 2.5mM KCl, 10mM $MgCl_2$, 10mM $MgSO_4$, 20mM glucose) was added and the Eppendorf flicked to mix the solution. This solution was used to inoculate an agar plate supplemented with 100µL/100mL ampicillin using a sterile plastic inoculation loop. This plate was then placed upside-down (to prevent the drying out of the agar plate as condensation would otherwise accumulate on the underside of the lid) overnight in an incubator set to 37°C.

After 24 hours, 1 colony from the plate was selected and seeded into a sterile 250mL conical flask containing 50mL LB (lysogeny broth) medium supplemented with 100µL/100mL ampicillin using a sterile Gilson tip. This flask was placed in a shaker incubator at 37°C and incubated overnight.

The culture was then centrifuged at 48,000g for 20 minutes and the supernatant removed. The plasmid DNA was extracted from the remaining precipitate using a GeneJET plasmid MidiPrep Kit (Thermofisher Scientific, MA, USA). The concentration of the resulting plasmid was

measured via absorbance to be 1467ng/µL using a NanoDrop spectrophotometer. Approximately half of this aliquot was diluted with elution buffer to 100ng/µL for cell transfection, while the other half was kept at the initial concentration for the purposes of molecular biology.

2.1.2 Site-directed mutagenesis

The R528C point mutation was introduced into the hERG1a coding sequence using PCR (Polymerase Chain Reaction) primers designed using the QuikChange® Primer Design Program (Agilent Technologies, CA, USA) and synthesised by Sigma-Aldrich (Irvine, UK) (see table 2-1). Before use primers were diluted to 100µM concentration using dH_2O (deionized water).

	Primer sequence
Forward	5'-ATCGGGCTGCTGAAGACTGCGTGTCTGCTGCGGCTGGTGCGCGTG-3'
Reverse	3'-TAGCCCGACGACTTCTGACGCACAGACGACGCCGACCACGCGCAC-5'

Table 2-1. The reverse and forward primer sequence used for the R528C mutation of hERG1a

For PCR, the KOD Hot Start DNA Polymerase (a PCR amplification kit, Sigma Aldrich, Irvine, UK) reagents and protocol were used. The reaction setup was as follows: 5µL 10x reaction buffer, 3µL 25mM $MgSO_4$, 5µL of 2mM dNTPs, 1.5µL of each 10µM primer (forward and reverse), 50ng of template DNA (WThERG1a) and 1µL of DNA polymerase. The total reaction volume was made up to 50µL using dH_2O.

A Peltier Thermal Cycler PTC-200 (MJ Research) was used to carry out the PCR reaction, with the PCR protocol being described in table 2-2. The cycle was repeated 40 times in order to obtain a high number of copies.

	Step	Temperature (°C)	Duration (s)
1	Polymerase Activation	95	2 minutes
2	Denature	95	20 seconds
3	Annealing	65	10 seconds
4	Extension	70	4 minutes 10 seconds
5	Reaction termination	6	-

Table 2-2. The sequence of the PCR cycle used to introduce the R528C point mutation into the WT-hERG1a channel plasmid

When the reaction was completed 1µL of Dpn I restriction enzyme was added to the reaction mixture and incubated at 37°C for 1 hour in order to digest any parental (methylated) cDNA.

After incubation the PCR product was purified from any remaining parental cDNA using a GeneJet Gel Extraction Kit (Thermofisher Scientific, MA, USA). The resulting cDNA was amplified using bacterial transformation as stated previously in section 2.1.1.

2.1.3 Plasmid sequencing

The WT and R528C hERG1a plasmids were diluted to approximately 70ng/µL using dH_2O before being sequenced by Eurofins Genomics (Ebersberg, Germany). Due to the size of the hERG1a construct several primers were required to obtain a complete read. These primers were designed to initiate at the hERG1a insert-flanking primers (P CMV and BGH) and the nucleotide sequence at positions 300, 500, 1000, 1500, 2000, 2500 and 3000 of the hERG1a construct. ApE software (M.W. Davis, USA) was used to edit the separate sequences together to create a full sequence reading, and the identity of each sequence was confirmed using BLAST software (NCBI, USA). BLAST software was also used to confirm that the arginine (R) residue at position 528 had correctly been mutated to a cysteine (C) residue through alignment of the WT and mutant sequences (see figure 2-2).

2.2 Cell culture

2.2.1 General maintenance and passaging of cell lines

The tsA201 cell line and the HEK293 stable cell line (kindly donated by Prof. Jules Hancox, University of Bristol from a gift from Dr Craig January, University of Wisconsin) were maintained in 8mL Dulbecco's Modified Eagle Medium (DMEM) with Glutamax-1 (Gibco, UK) supplemented with 10% Foetal Bovine Serum (FBS) and 1% Penicillin/Streptomycin (Gibco, UK) and kept in 25cm^2 cell culture flasks (CELLSTAR, Greiner Bio-One, UK). Cells were kept in an incubator maintained at 37°C and 5% CO_2. Upon reaching approximately 80% confluence cells were passaged using supplemented DMEM, phosphate buffered saline (PBS) and enzyme-free, PBS-based cell dissociation buffer (Gibco, UK) preheated to approximately 37°C.

Cells were washed twice with 5mL PBS after removal of old media and then incubated for a maximum of 3 minutes with 2mL dissociation buffer. The addition of 6mL DMEM diluted the dissociation buffer and subsequent aspiration of the solution ensured the majority of cells were removed from the surface of the flask and transferred into suspension.

The resulting suspension was either split into flasks, either a 1:8 dilution (1mL cell suspension to 7mL DMEM) or 1:16 dilution (0.5mL cell suspension to 7.5mL DMEM) or seeded into 35 x 10mm tissue culture dishes (Falcon, Corning, UK) using approximately 1-2 drops of cell suspension and 2mL DMEM. Dishes were incubated for a minimum of 24 hours before transient transfection.

HEK-293 cells stably expressing the WT hERG1a channel were maintained identically to the tsA201 cells, with the exception of being seeded onto poly-L-lysine treated glass coverslips in the 35mm tissue culture dishes for the purposes of AFM.

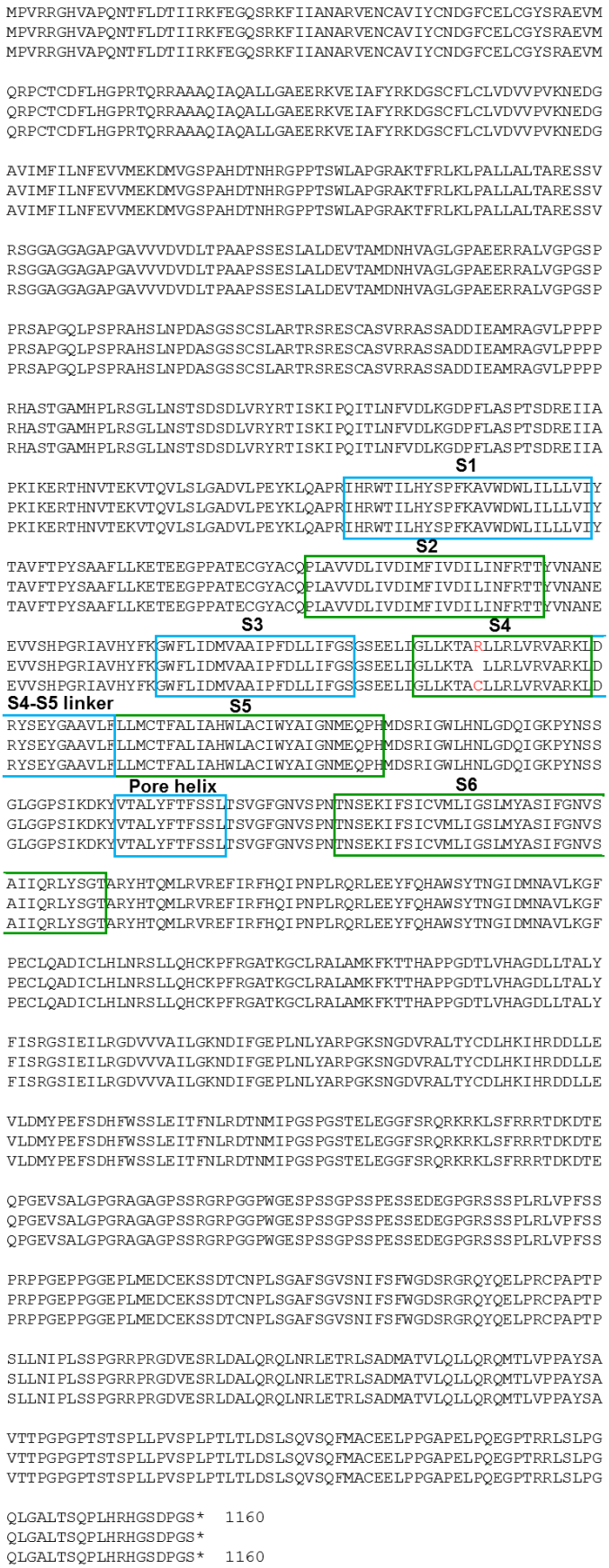

Figure 2-2. Amino acid sequence alignment of the WT-hERG1a (top line) and the R528C mutant (bottom line) which were used in experiments. The middle line represents the sequence alignment, with a blank space indicating a difference in the sequence. Transmembrane regions are outlined in either green or blue, with the arginine residue at position 528 which was mutated to a cysteine shown in red.

2.2.2 Transient Transfection

Cells required for transfection were plated in 35mm tissue culture dishes for a minimum of 24 hours before transfection. Transfection was carried out using polyethylenimine (PEI, Alfa Aesar, USA) at a concentration of 0.2µg/µL. The PEI solid was dissolved by addition of HCl and dH_2O in order to reduce the pH to approximately 2. Once dissolved KOH was added dropwise to raise the pH to 7.4 and the solution passed through a 0.22µm filter under sterile conditions.

The channel plasmid and the marker eGFP (enhanced green fluorescent protein) were incubated in a 2:1 ratio together with 80µL PEI for 10 minutes, and then with 680µL non-supplemented DMEM for 30 minutes. This solution was added dropwise to the tissue culture dishes and the cells left to incubate for 24-48 hours before any electrophysiology experiments took place. The co-transfection of eGFP with the channel plasmid allowed the identification of cells expressing the channel through use of a 510nm emission filter with a 490nm light source. (see figure 2-3).

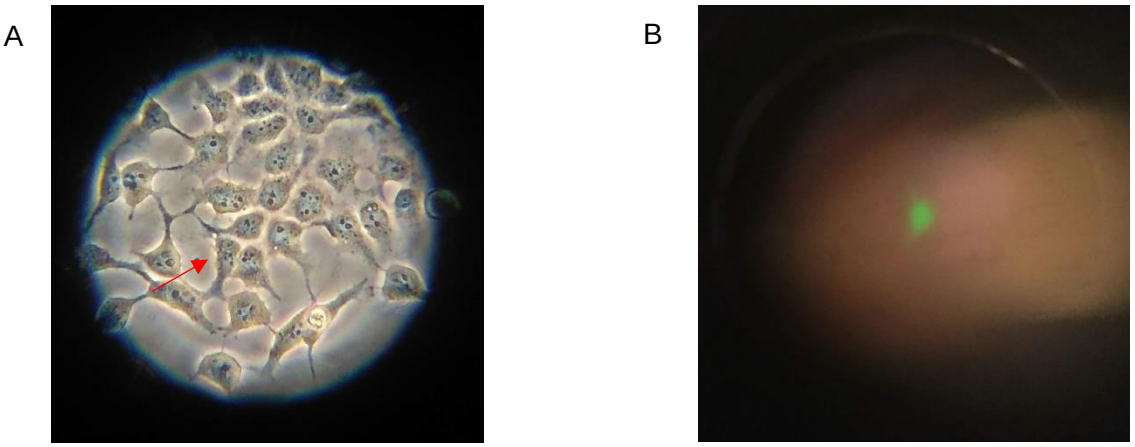

Figure 2-3. The co-transfection of the eGFP plasmid enabled identification of cells which were expressing the channel plasmid. *A,* Cells imaged under a x40 objective, with red arrow indicating the cell positive for the eGFP marker. *B,* the same sample imaged under UV light with the eGFP-positive cell clearly visible.

2.3 Electrophysiology

2.3.1 Recording Solutions

For recording of ionic currents, cells were bathed in an external solution of composition (mM): 144 NaCl, 2.5 KCl, 1.2 MgCl, 2.5 $CaCl_2$, 10 HEPES Acid and 10 D-Glucose. The pH was titrated to 7.4 using 1M KOH and the osmolarity was measured to be 280-295mOsmol using a Wescor Vapor Pressure Osmometer VAPRO (Model 5520). The electrodes were filled with a solution of composition (mM): 130 K.Aspartate, 0.1 EGTA, 3 NaOH, 20 KCl, 50nM $CaCl_2$, 1.5

$MgCl_2$ and 1.5 Na_2ATP (disodium salt) of osmolarity 295mOsmol. This was titrated to pH 7.4 using 1M KOH. The junction potential was measured to be +13mV which was not accounted for.

For gating current recordings, cells were bathed in an external solution of composition (mM): 150 TEA, 10 HEPES Acid, 10 $MgCl_2$ and 2.5 $CaCl_2$. The osmolarity was measured to be 280-290mOsmol and the pH titrated to 7.4 using 1M NaOH. The electrodes were filled with a solution of composition (mM): 150 NMDG (N-Methyl-D-glucamine), 1.5 $MgCl_2$, 0.1 EGTA (Ethylene glycol-bis(2-aminoethylether)-N,N,N′,N′-tetraacetic acid), 5 HEPES Acid, 1.5 MgATP and 50nM $CaCl_2$. The osmolarity was measured to be 280mOsmol, and the pH titrated to 7.3 using 1M HCl. The resulting junction potential was measured to be -8mV which was not accounted for.

2.3.2 Electrodes and recording system set-up

KG-33 glass (1.5 mm OD 1.1 mm ID filamented) electrodes were fabricated using a Narishige Puller (Model PP-830) and fire-polished before being filled with the internal solution to achieve an electrode resistance of 2.5-8MΩ. The filled micropipette was inserted onto an electrode holder comprising of a silver wire coated with a layer of Ag/AgCl. This layer was achieved using electrolysis in a 0.1% NaCl solution, with the chloride anions being attracted to the silver wire when attached to the positive electrode. This process was repeated frequently throughout the project to ensure a complete and even coverage of the silver wire.

Once assembled, the electrode was inserted into a CV201A Headstage (Axon Instruments) which was in turn connected to a PatchStar Micromanipulator (Scientifica). The entire set-up, together with the tissue culture dishes and the inverted microscope with an ultraviolet light source (Zeiss Axiovert 100, Germany) was mounted on a nitrogen air table which vibrationally isolated the equipment.

The tissue culture dishes were mounted on the experimental platform on the microscope and were perfused with the external solution by a constant inflow of solution through the inflow pipe and a constant removal of solution through the outflow pipe. An Ag/AgCl pellet was placed at the edge of the tissue culture dish (yet making contact with the external solution) to act as the ground electrode.

Approximately 50mL of solution was in the perfusion system at any one time, with the entire system being driven by a pump (Watson Marlow 505S). Before recording 50mL of solution was washed through the tissue culture dish and allowed to run to waste in order to fully remove the DMEM in which the cells had been incubated, which would otherwise prevent a seal from forming.

2.3.3 Software and data acquisition

Pulse (HEKA, Germany) was used to apply the voltage protocols, and the resulting currents were recorded using an Axopatch 200A amplifier (Axon Instruments). Currents were low-pass filtered at 1 kHz (ionic currents) or 2 kHz (gating currents) using an 8-pole Bessel filter (Frequency Devices) and acquired at 10 kHz using Pulse at room temperature (approximately 22°C). Additionally, a "-P/4" protocol was used for the online subtraction of leak-current from gating currents.

2.4 Data analysis

The raw data from whole cell recordings was imported into Origin 9.1 Software (OriginLab Corporation, MA, USA) in the form of HEKA data files and used to produce the representative current traces. Current amplitude and charge were measured in Pulse. Pulsefit (HEKA) was used to fit the decay of both on and off gating currents with single- or double-exponential functions (as required).

Current-voltage relationships from both ionic and gating currents were expressed as normalised data and were fitted by a single Boltzmann equation:

$$y = \frac{1}{1 + \exp\left[\frac{V_{0.5} - V_m}{k}\right]}$$

Where $V_{0.5}$ represents the half-maximal activation voltage and k represents the slope factor, a measure of the voltage dependence of the channel.

Where appropriate, current-voltage relationships were fitted with a double-Boltzmann equation:

$$y = \frac{A_1}{1+\exp\left[\frac{V_{0.5-1}-V_m}{k_1}\right]} + \frac{A_2}{1+\exp\left[\frac{V_{0.5-2}-V_m}{k_2}\right]}$$

An alternative form of the Boltzmann equation was used to fit curves in the inactivation experiments in order to calculate the half-maximal inactivation voltage ($V_{0.5}$) and the slope factor for inactivation (k):

$$\frac{I}{I_{max}} = 1 - \frac{1}{1 + \exp\left[\frac{V_{0.5} - V_m}{k}\right]}$$

Where I_{max} was the maximal tail current amplitude of that protocol and I was the tail current amplitude elicited by the membrane voltage (V_m).

The deactivation of I_{hERG} was quantified by fitting the following bi-exponential equation to tail currents:

$$I = A_f exp\left(\frac{-x}{\tau_f}\right) + A_s exp\left(\frac{-x}{\tau_s}\right) + C$$

Where the total current (I) at time x is expressed as the current fitted by the fast (τ_f) and slow (τ_s) components of the deactivation time course (A_f and A_s) together with any residual unfitted current (C).

GraphPad Prism 7.0 Software (Graphpad Inc, La Jolla, CA, USA) was used for the fitting of activation curves and to interpolate data plotted in I/V relations using polynomial functions, where appropriate.

2.4.1 Statistics

All data is presented as mean ± SEM (standard error of the mean). Statistical analysis was performed using GraphPad Prism 7.0 Software and Excel Office 365 (Microsoft, Redmond, WA), with $p<0.05$ considered to be statistically significant. P values were calculated using one or two-way analysis of variance (ANOVA) with Bonferroni post-hoc tests or unpaired t-test. Asterisks indicate statistical significance; *, **, *** and **** denote p values of <0.05, <0.01, <0.001 and <0.0001 respectively.

2.5 AFM imaging

2.5.1 Microscope and cantilevers

For AFM imaging a Dimension 3100 (Veeco Instruments Inc, NY, USA) and a MultiMode VIII microscope with a NanoScope V controller (Bruker Corporation, CA, USA) were used together with triangular silicon cantilevers of a spring constant between 0.01-0.7N/m. Samples were fixed on glass coverslips using 4% paraformaldehyde solution. Cells were imaged using a variety of modes; intermittent contact mode in both air and liquid, and contact mode in both air and liquid. Images were analysed using NanoScope Analysis Software Version 6 (Bruker Corporation, CA, USA) and Gwyddion 2.53 Software (David Nečas and Petr Klapetek, Department of Nanometrolgoy, Czech Metrology Institute).

2.5.2 Preparation of glass coverslips

Circular borosilicate glass slips of 13mm diameter and no. 1 thickness (0.13mm) (VWR International) were acid washed in 1M HCl for a minimum of 16 hours, then washed twice in dH_2O and once in ethanol and allowed to dry.

A 1mg/mL solution of poly-L-lysine (Sigma Aldrich, Irvine, UK) (made using dH_2O and filtered using a 0.2µm filter) was left to incubate on the washed coverslips overnight. The coverslips were then washed in dH_2O and allowed to dry for a minimum of 2 hours before being used. Alternatively, the coverslips were stored in tissue culture dishes (one per dish) ready for use.

Cells were placed dropwise onto the coverslip and left to settle for approximately 20 minutes before 2mL supplemented DMEM was added to the tissue culture dish. Cells were grown for a minimum of 48 hours before fixation and imaging.

2.5.3 Cell fixation

Though the original intention had be to image live cells, it transpired that cells were required to be fixed using a 4% solution of paraformaldehyde (PFA). In order to fix channels in the open state, a PBS solution with a high concentration of potassium was used to make the PFA solution with the following ion concentrations (mM): 104 NaCl, 38.8 KCl, 8.1 Na_2HPO_4 and 1.2 KH_2PO_4 (Sasaki et al., 1995). This was in comparison to the normal PBS which had ion concentrations of (mM): 137 NaCl, 2.7 KCl, 10 Na_2HPO_4 and 1.8 KH_2PO_4.

The 4% PFA solution was made through addition of PFA powder to heated PBS (either high or low potassium), NaOH then added dropwise to dissolve the PFA and the final pH adjusted to 7.4 using HCl.

Upon fixation, cells were washed twice with the appropriate PBS solution, then approximately 2mL PFA was added to the dish and allowed to incubate at room temperature for 45 minutes. The cells were washed twice and stored in dH_2O at 3°C for up to one week, although cells were usually fixed on the day of imaging.

For imaging in air, cells were fixed as stated previously and then washed in dH_2O twice in order to remove PBS crystals. The excess liquid was poured off and the remaining blotted off using filter paper. These dishes were then left for a minimum of an hour at room temperature to allow evaporation of any remaining dH_2O before being imaged.

3. Ionic current of WT-hERG1a and the R528C mutant

3.1 Introduction

R528 is an arginine residue in the distal S4 domain of the hERG1a channel (see figure 3-1). Due to its positive charge, it is repelled from the lipid bilayer upon membrane depolarisation. It forms charge pairings with negative residues in other transmembrane helices which facilitates the movement of S4 out of the membrane (Subbiah et al., 2005; Zhang et al., 2005).

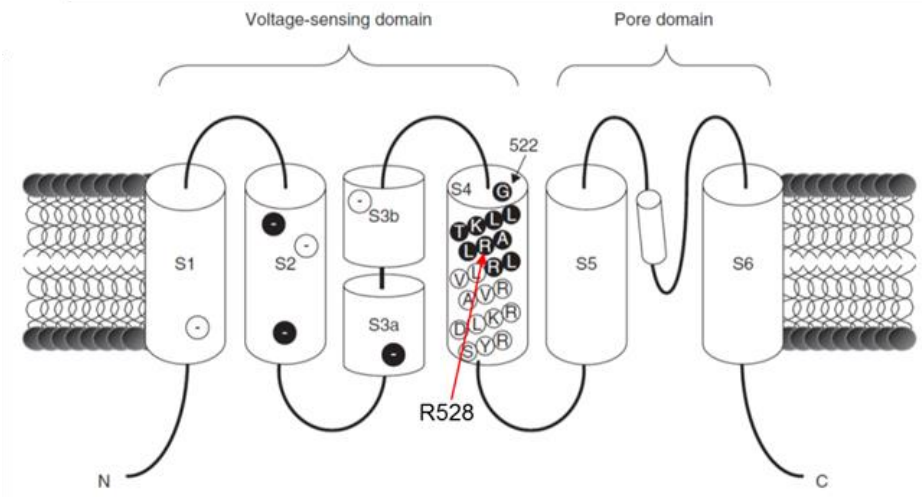

Figure 3-1. The location of R528 within the S4 transmembrane region of the WT-hERG1a channel. Only one subunit of the hERG1a tetramer is shown for clarity. Adapted from Elliot et al., 2009.

Due to R528 having a role in the movement of S4 in and out of the membrane, it is consequently involved more in the activation and deactivation of the channel compared with the inactivation, which is theorised to involve the S5-P linker and the selectivity filter (Vandenberg et al., 2004; Perrin et al., 2008). Mutations of R528 have not yet been identified to be a cause of either LQTS or SQTS (Splawski et al., 2000), and as a result the effect of a mutation of R528 on hERG1a current has yet to be fully determined.

The R528C mutation was chosen for this body of research from the conclusions drawn by Zhang et al., 2004, who found that the R528C-hERG1a $V_{0.5}$ of activation was positively shifted and the gating charge was significantly reduced relative to WT-hERG1a. Therefore, it was expected that both the ionic and gating currents of the mutant would be affected by this mutation.

Furthermore, the position of the R528C mutation would allow modification by MTSET (2-(Trimethylammonium)ethyl methanethiosulfonate), a positively charged MTS reagent which is membrane impermeable. This would bind to the mutated cysteine residue upon activation of the channel and upward S4 movement, effectively locking the channel in its activated state which would allow the activated form of channel to be imaged using AFM (Zhang et al., 2004). However, due to limitations encountered when using AFM this was not employed during the course of this research.

The aims of this chapter are to characterise the ionic current of the R528C-hERG1a mutant and compare this with the ionic current of WT-hERG1a. Furthermore, the stable hERG1a-HEK293 cell line will be briefly characterised to ensure that there is no functional difference between the I_{hERG} produced by stable and transient expression of the channel.

3.2 Results

3.2.1 The activation of hERG1a and the R528C mutant

To quantify the activation of I_{hERG}, a voltage protocol was applied that would elicit tail currents (see figure 3-2, *A*). A 10ms pre-pulse to -60mV from a holding potential of -70mV was first applied to enable leak subtraction of the current, before a 2 second pulse to potentials between -40mV to +50mV in 10mV increments. This depolarising pulse activated the channel before

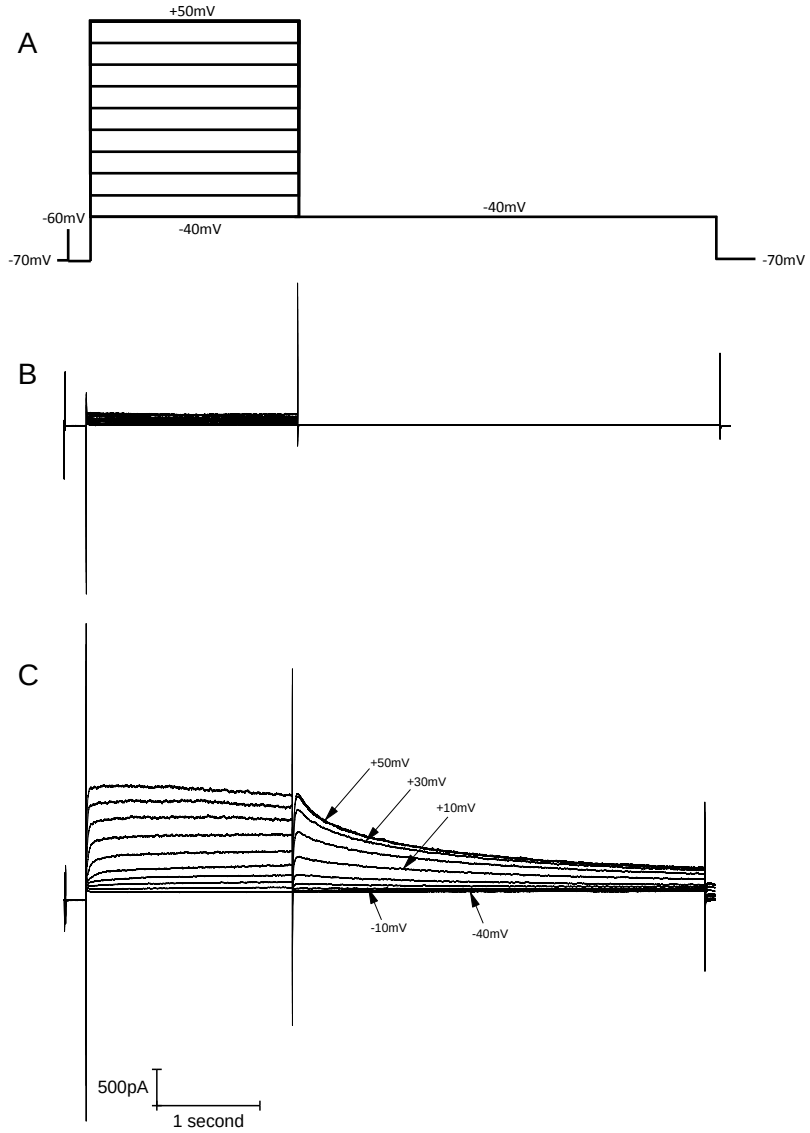

Figure 3-2. Protocol for producing an activation curve for WT-hERG1a current. *A,* Voltage protocol used to elicit current. After a 10ms depolarising prepulse to -60mV from a holding potential of -70mV, cells were depolarised to voltages between -40mV to +50mV at 10mV intervals for 2 seconds, and then repolarised to -40mV for 4 seconds before returning to the -70mV holding potential. *B,* Representative current trace from non-transfected cells using the previous voltage protocol. *C,* Representative current trace from cells transfected with the WT-hERG1a subunit using the previous voltage protocol, showing the pulse currents in the depolarising step and the tail currents upon the repolarisation step.

shifting the channel quickly (relative to its opening) into its inactivated state, as seen by the rise in outward current (pulse current) before the current begins to plateau which reflects channel inactivation. Cells were then repolarised with a +40mV pulse of 4 seconds which resulted in the stereotypical outward 'tail currents', as seen in previous hERG1a studies (Sanguinetti et al., 1995b; Trudeau et al., 1995; McPate et al., 2005; Zhang et al., 2011). These tail currents, which were not seen in non-transfected cells (see figure 3-2, *B*) result from channel inactivation being relieved and thus it shifts back into its open and conducting state, allowing the channel to conduct a large amount of current before deactivating, (see figure 3-2, *C*).

The amplitude of the tail current from non-transfected cells and those transfected with WT-hERG1a were used to plot an I/V relation where the magnitude of current was expressed as current density (pA/pF) (see figure 3-3). This normalisation took into account cell size as capacitance can be used as a measure of cell membrane surface area, however the voltage dependence of WT-hERG1a activation (as measured by $V_{0.5}$) remained positively shifted compared with those found previously (Zhou et al., 1998; McPate et al., 2005).

From figure 3-3 it can be seen that there was a small amount of voltage-independent current present in non-transfected cells. This current was insignificant relative to the current recorded from transfected cells and could be attributed either to a low-level presence of endogenous channels or to a small-amplitude leak current (Yu and Kerchner, 1998; Varghese et al., 2006; Ponce et al., 2018).

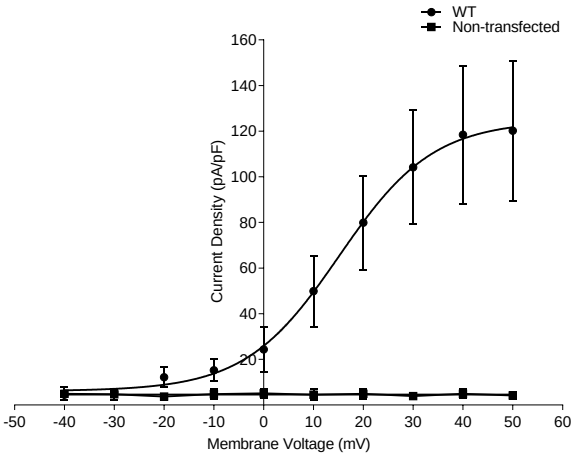

Figure 3-3. Normalised tail current I/V relationship of WT-hERG1a. The I/V curve was plotted using the leak-subtracted peak tail current amplitude evoked by the preceding depolarising step, which was then normalised to capacitance to reflect the surface area of the cell membrane, WT-hERG1a (●, n=8) and non-transfected cells (■, n=8). The curve for non-transfected cells shows a small amount of endogenous current whilst the curve for WT-hERG1a was fitted to a Boltzmann function ($V_{0.5}$ = 15.2 ± 5.7mV, k = 9.4 ± 0.56mV).

The end-pulse I/V relation is an accepted method of demonstrating the inward rectification of hERG (Zhang et al., 2011; Butler et al., 2019) as the magnitude of outward current at end of the pulse current is determined by both channel activation and inactivation (see figure 3-4, *A*). As the membrane voltage becomes increasingly depolarised, the channel will favour the inactivated state leading to a decrease in channel conductance and therefore a decrease in the outward current (Sanguinetti, 2004).

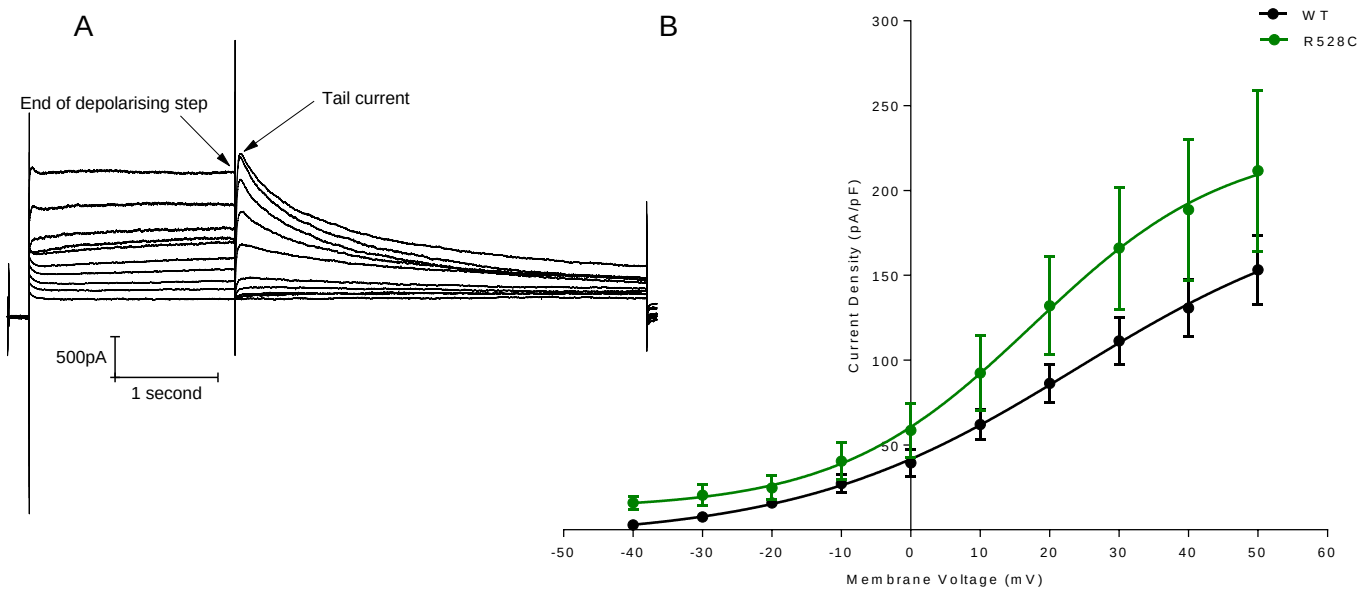

Figure 3-4. I/V relationship of WT-hERG1a (●, n=8) and R528C-hERG1a (●, n=10) leak-subtracted end-pulse current. *A,* Representative current trace from WT-hERG1a, arrows show where current amplitudes were measured for the voltage-dependent activation curve (tail currents) and for the I/V relationship shown *B,* (end of depolarising step). Two-way ANOVA with Bonferroni multiple comparisons found there was no significant difference between WT and mutant at any membrane voltage ($p>0.05$).

Figure 3-4, *B* shows the leak-subtracted end-pulse I/V relation for both WT-hERG1a and R528C-hERG1a current, demonstrating that both showed a similar increase in end-pulse current amplitude over the voltage range. R528C-hERG1a appeared to have a greater current density than WT-hERG1a (a maximum of 229 ± 56.0mV (n=10) compared with 195 ± 59.8mV (n=8), although this difference was found not to be significant, two-way ANOVA). This difference can be accounted for by R528C-hERG1a having an accelerated activation rate compared with WT-hERG1a (see figure 3-6), resulting in more current being conducted in the pulse current before the channel transitions into the inactivated state.

However, it can be seen from the end-pulse I/V relation plotted (figure 3-4, *B*) that the current had no negative slope even at the most positive test voltages used. This could be explained by the experiment being conducted at room temperature, as I_{hERG} activation is known to be shifted rightwards by a decrease in temperature (Mauerhöfer and Bauer, 2016). The reasons for not conducting experiments at physiological temperatures were two-fold; at lower temperatures the kinetics of the channel would be slowed enough to resolve the gating currents (see chapter 4), and the AFM microscope did not have the capability to heat samples. Recording ionic currents at room temperature maintained the internal validity of the project.

Using the same protocol, R528C-hERG1a tail current amplitude (see figure 3-5, *A*) was measured and normalised with respect to the peak current recorded in each cell. Comparison of WT-hERG1a and R528C-hERG1a tail currents enabled voltage dependence differences to

be elucidated, as tail currents indicate the level of channel activation when inactivation is removed (Zhou et al., 1998; Sanguinetti, 2004; McPate et al., 2005; Butler et al., 2019).

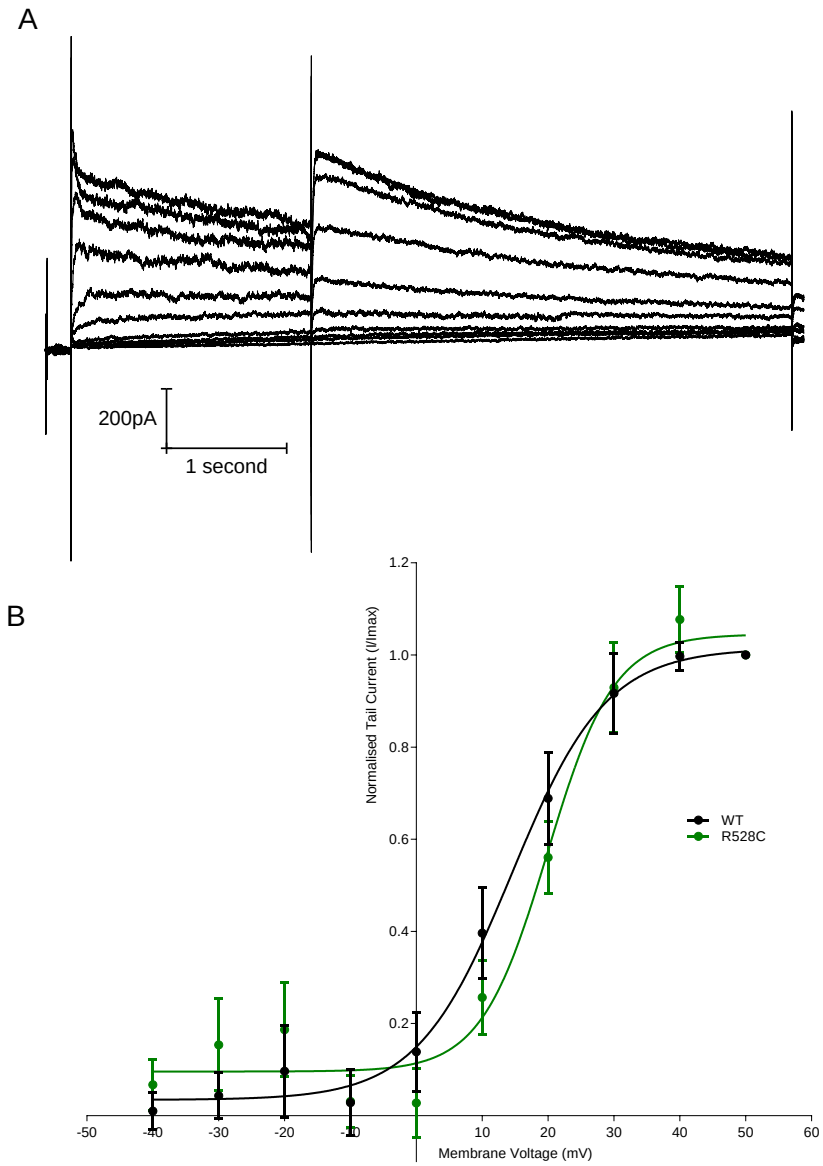

Figure 3-5. The activation curve of the R528C mutant. *A,* Representative current trace from the R528C mutant, tail current amplitude was measured and used the produce the activation curve below. *B,* the normalised leak-subtracted activation curves of WT-hERG1a (●, n=8) and the R528C mutant (●, n=10). Curves were fitted to a Boltzmann relationship. Two-way ANOVA with Bonferroni multiple comparisons found no difference between the two relationships (p=0.4258).

Figure 3-5, *B* shows the resulting normalised tail-current/voltage relations, for both WT-hERG1a and R528C-hERG1a current fitted to a Boltzmann function to enable comparison of the voltage dependence of activation. Both I/V relations followed a sigmoidal relationship with R528C-hERG1a having a slight depolarising shift relative to WT-hERG1a, implying that more depolarisation was required to activate the channel owing to the loss of a positively charged S4 residue. Mean $V_{0.5}$ (half maximal activation voltage) for WT-hERG1a and R528C-hERG1a were +15.2 ± 5.7mV (n=8) and +18.1 ± 2.2mV (n=10) respectively, and mean k (slope of the I/V relationship) were +9.4 ± 0.56mV and +10.4 ± 0.93mV, respectively.

The activation of I_{hERG} was further quantified by the fitting of a mono-exponential to the rising phase of the current following the depolarising command voltage. Figure 3-6 shows the measured time constants plotted against the command pulse potential and subsequently fitted with a mono-exponential decay. There is a clear voltage-dependence of the activation time constant, which decreases exponentially as the command potential becomes more positive. R528C-hERG1a appears to have a smaller time constant of activation compared with WT-hERG1a, meaning a faster rate of R528C-hERG1a current activation. However, this difference between WT-hERG1a and R528C-hERG1a activation kinetics was found not to be significant at any membrane potential (two-way ANOVA, $p>0.05$)

There was no significant difference between any of the derived parameters of WT-hERG1a and R528C-hERG1a indicating that the R528C mutation had no statistically significant effect on the voltage dependence or kinetics of activation of the channel relative to the WT-hERG1a. There was indication of a small depolarising shift of the voltage dependence of activation of R528C-hERG1a, given the position of the activation curve and the magnitude of $V_{0.5}$, and a small increase in the rate of activation, but with the sample size analysed these differences were not found to be significant.

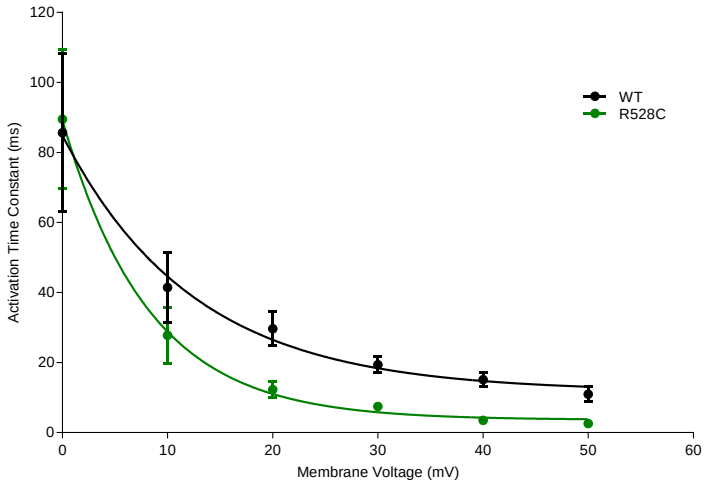

Figure 3-6. The time constant (τ) of WT-hERG1a (●, n=8) and R528C-hERG1a (●, n=10) I_{hERG} activation. The rising phase of the outward I_{hERG} after the depolarising command voltage was fitted with a monoexponential. At membrane potentials <0mV the degree of activation was considered too small to fit exponentials accurately. WT-hERG1a and R528C-hERG1a τ were calculated to be 12.5ms ± 5.7ms and 8.2ms ± 2.6ms, respectively. Two-way ANOVA found there to be no significant difference between the two time constants.

3.2.2. The effects of the R528C mutation on the fully activated I/V relations of hERG1a

To obtain the fully activated I/V relationship, the voltage protocol in figure 3-7, *A* was used (McPate et al., 2005; Zhang et al., 2011). A 10ms pre-pulse to -60mV from a holding potential of -70mV preceded a 2 second +20mV depolarising pulse. This was followed by a 4 second repolarising pulse to voltages between -100mV and +30mV at 10mV intervals, before returning to the holding potential for 100ms. As can be seen in the representative current trace (figure 3-7, *B*), this protocol elicited tail currents due to the channel being released from inactivation and then subsequently deactivating over the 4 second command pulse.

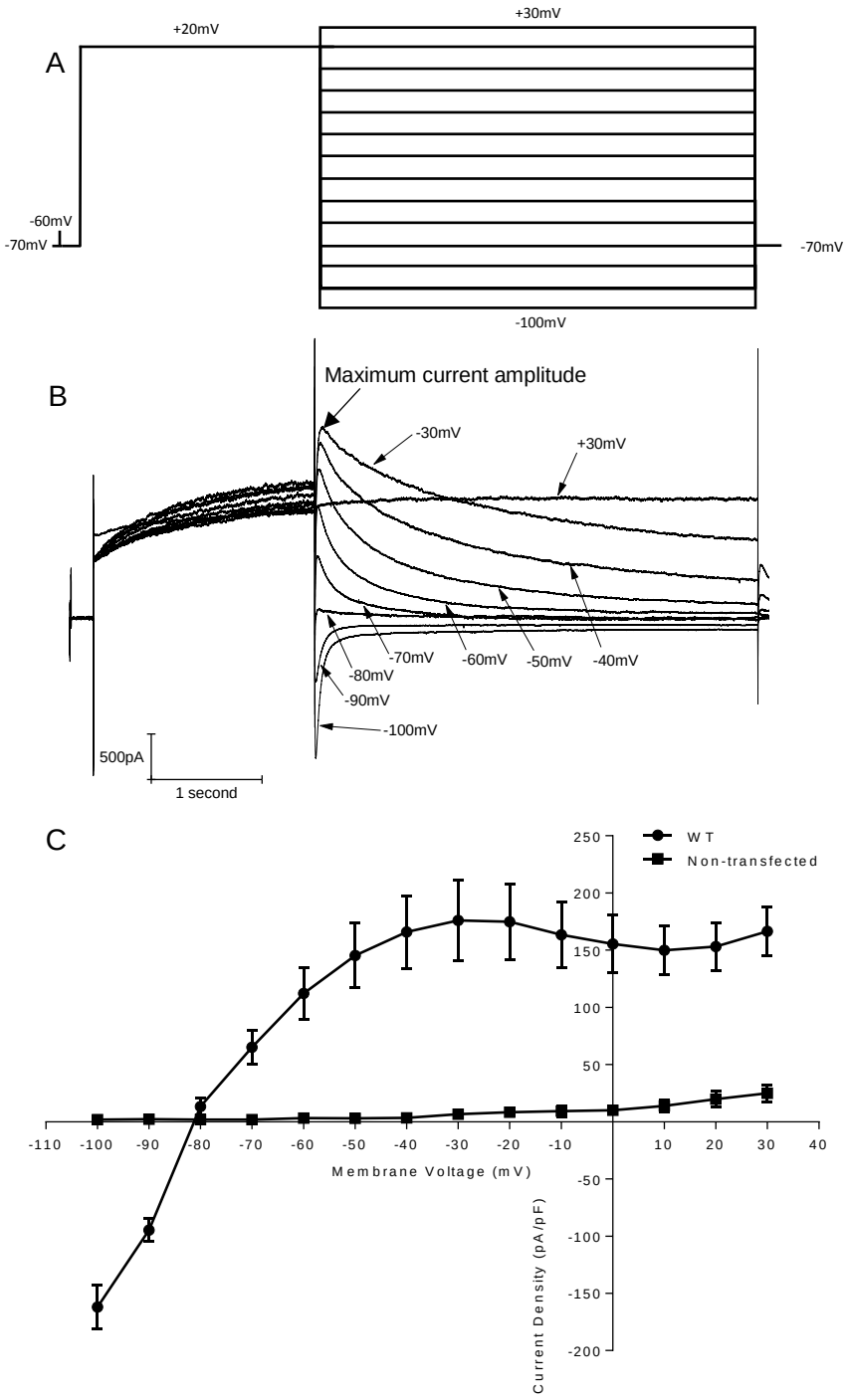

Figure 3-7. Protocol used to produce the fully activated I/V relations for WT-hERG1a. *A*, the voltage protocol used to elicit current. After a 10ms depolarising prepulse to -60mV from a holding potential of -70mV, cells were depolarised to +20mV for 2 seconds, and then repolarised to voltages from -100mV to +30mV at 10mV intervals for 4 seconds. *B,* Representative current trace from WT-hERG1a-transfected cells. Some traces have been omitted for clarity. To produce the fully activated I/V relation, current amplitude was measured at the maximum current amplitude, see arrow on trace. *C,* The fully activated I-V relation measured from the peak WT-hERG1a current (●, n=8), and the endogenous current from non-transfected cells (■, n=4), expressed as current density (pA/pF).

This was first utilised in cells transfected with WT-hERG1a and compared with non-transfected cells, see figure 3-7, *C.* In the representative current trace from WT-hERG1a, it can be seen that the tail current amplitude increased as the membrane potential became increasingly positive, reversing and peaking at approximately -80mV and -30mV respectively (see figure 3-7, *B*). At the most depolarised membrane potentials no tail currents were elicited given that channels were inactivated. A small-amplitude current was elicited from non-transfected cells which given its increasing amplitude as the membrane potential became more depolarised,

could be attributed to leak current or a low-level expression of endogenous channels (Yu and Kerchner, 1998; Varghese et al., 2006; Ponce et al., 2018).

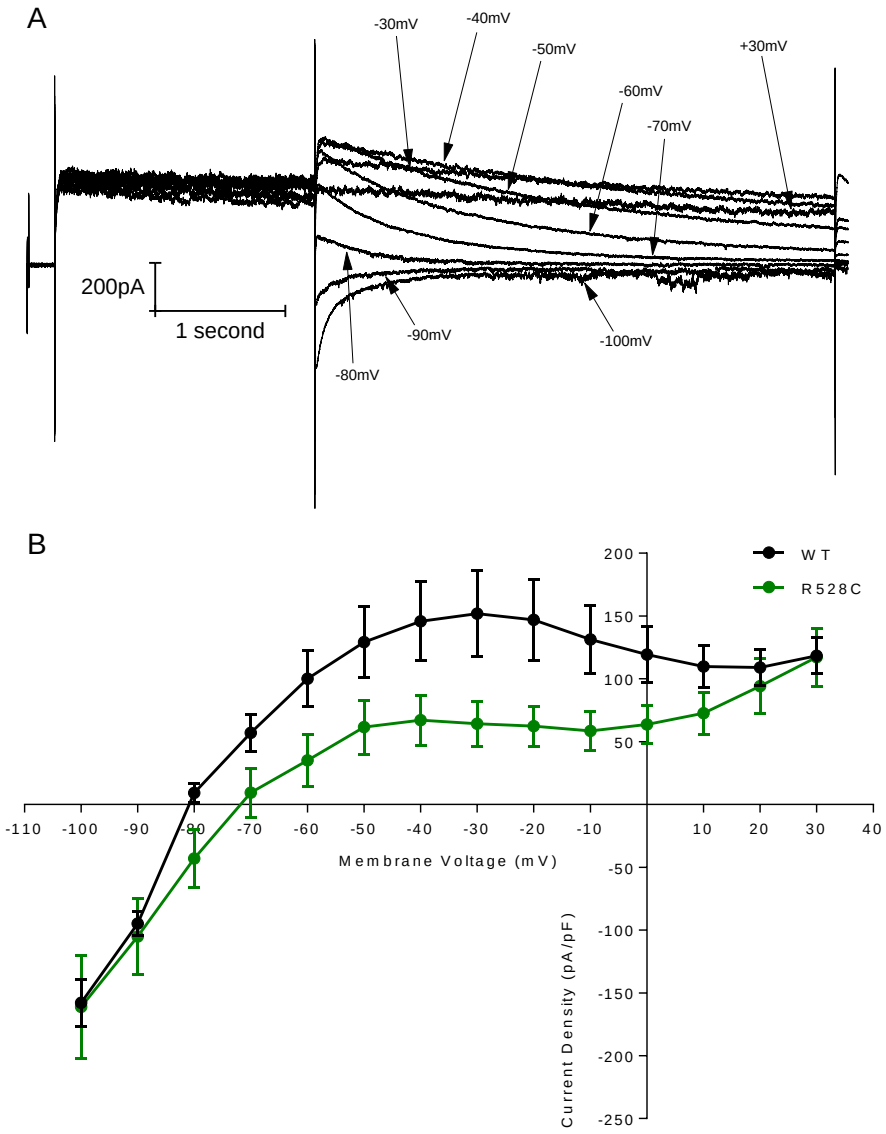

Figure 3-8. Fully activated curve of the R528C mutant current. *A,* Representative current trace from the R528C-hERG1a mutant when transiently expressed in tsA201 cells, with some traces omitted for clarity. *B,* The normalised fully activated I/V relation of WT-hERG1a (●, n=8) and R528C-hERG1a (●, n=9), two-way ANOVA found a significant effect of the R528C mutation relative to WT-hERG1a ($p<0.05$). The reversal potential for WT-hERG1a was found to be -79.9 ± 0.11mV. For R528C the reversal potential was found to be -72.3 ± 0.02mV. Unpaired t-test found a significant difference between WT and mutant reversal potential ($p<0.05$).

The voltage protocol in figure 3-7, *A* was applied to the R528C mutant, and the representative current trace can be seen in figure 3-8, *A*. The R528C-hERG1a current trace resembled that of WT-hERG1a, with tail currents being elicited by the repolarising pulse. These tail currents reversed and peaked at approximately -80mV and -40mV respectively, with R528C-hERG1a current appearing to be of smaller amplitude than WT-hERG1a. The tail current amplitude (leak subtracted and normalised with respect to membrane capacitance) from both WT-hERG1a and R528C-hERG1a was used to plot the fully activated I/V relation seen in figure 3-8, *B*.

Both WT-hERG1a and R528C-hERG1a followed a similar pattern of rising to a peak current amplitude and then decreasing as the membrane potential became more depolarised. However, WT-hERG1a peaked at ~-30mV whilst R528C-hERG1a peaked slightly more negatively at ~-40mV and the current density for R528C-hERG1a was lower than that of WT-hERG1a. The reversal potential for R528C-hERG1a (-72.3 ± 0.02mV, n=9) was found to be significantly more depolarised than that of the reversal potential for WT-hERG1a (-79.9 ± 0.11mV, n=8, $p<0.05$, unpaired t-test).

Using the Goldman-Hodgkin-Katz voltage equation and the reversal potential values attained from the fully activated I/V relation, the Na^+: K^+ permeability ratio for WT-hERG1a was calculated to be 0.029 which increased to 0.043 in the R528C mutant. Therefore the mutation increased the channel's selectivity towards conducting Na^+ ions and away from K^+ ions, as is reflected in the more depolarised E_K of the R528C mutant, implying that S4 domain can interact with the channel's selectivity filter.

To quantify the deactivation of WT-hERG1a and R528C-hERG1a current, the traces of the tail currents were fitted with a bi-exponential decay in order to attain the fast (τ_f) and slow (τ_s) components of deactivation, as in Sanguinetti et al., 1995; Zhou et al., 1998; McPate et al., 2005; Butler et al., 2019. The time constants were expressed in milliseconds (τ_f) and seconds (τ_s) and plotted against the repolarisation potential, see figure 3-9, *A and B*. Tail currents elicited by potentials of -10mV to +30mV were considered too small to be able to fit the bi-exponential decay with sufficient accuracy.

Both fast and slow components of R528C-hERG1a were significantly increased relative to WT-hERG1a (two-way ANOVA, $p<0.05$ and $p<0.01$ respectively), indicating that the R528C mutation slowed the deactivation rate of the channel. From the two plots there appeared to be a greater effect on the fast time component, partially due to the poor resolution of the slow time component as a result of recording at room temperature (further slowing the component) and partially due to a large error being associated with τ values greater than 1 second given that the depolarising pulse was only 4 seconds. However, expressing the total deactivation current as a fraction of the fast deactivating current ($A_f/A_f + A_s$) indicated there was no significant difference between the contribution of either component in the R528C-hERG1a mutant relative to WT-hERG1a (see figure 3-9, *C*). This implied that both fast and slow time constants increased equally, and one component was not affected more than the other by the mutation.

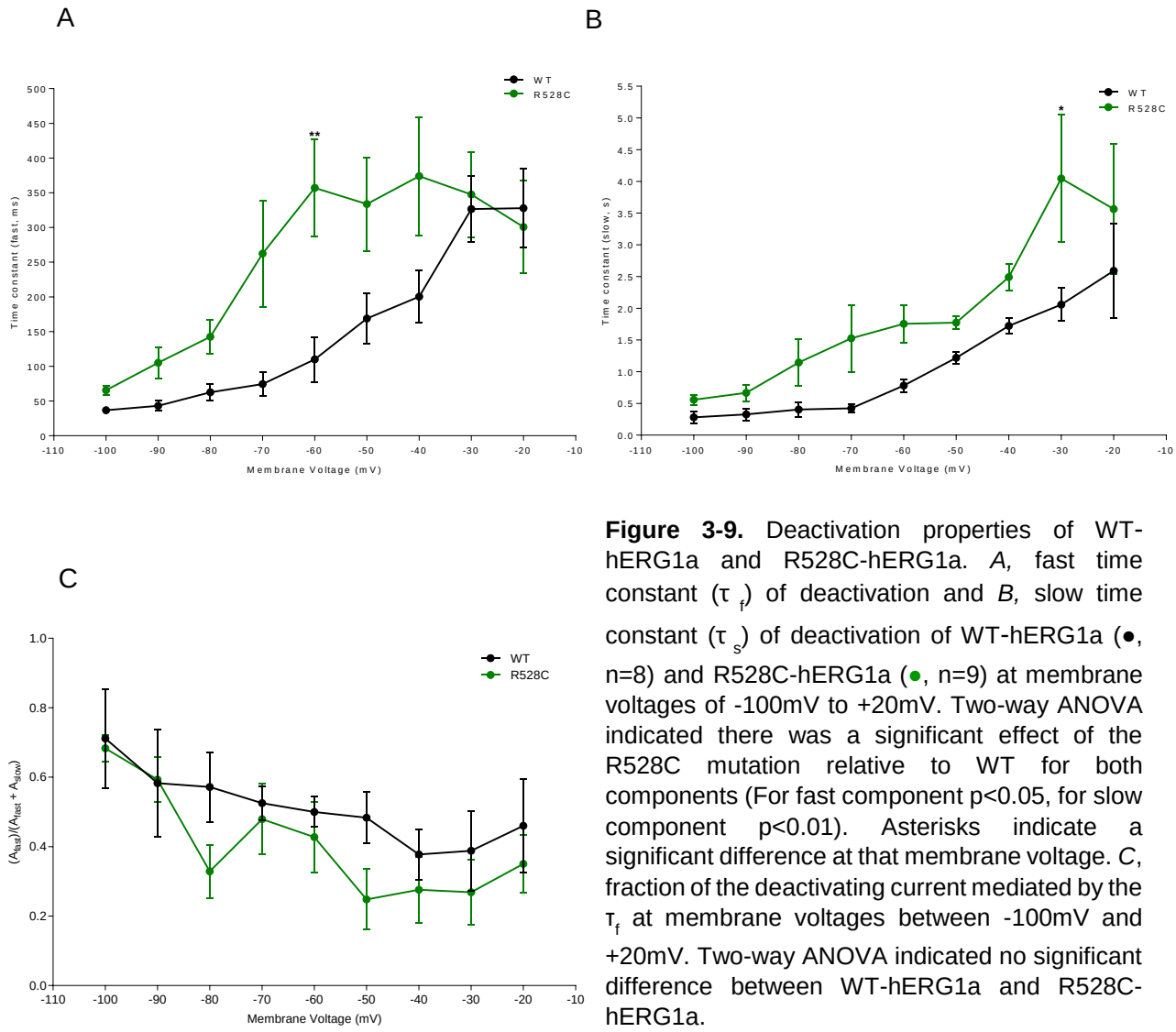

Figure 3-9. Deactivation properties of WT-hERG1a and R528C-hERG1a. *A,* fast time constant (τ_f) of deactivation and *B,* slow time constant (τ_s) of deactivation of WT-hERG1a (●, n=8) and R528C-hERG1a (●, n=9) at membrane voltages of -100mV to +20mV. Two-way ANOVA indicated there was a significant effect of the R528C mutation relative to WT for both components (For fast component $p<0.05$, for slow component $p<0.01$). Asterisks indicate a significant difference at that membrane voltage. *C*, fraction of the deactivating current mediated by the τ_f at membrane voltages between -100mV and +20mV. Two-way ANOVA indicated no significant difference between WT-hERG1a and R528C-hERG1a.

3.2.3. The inactivation of WT-hERG1a and the R528C mutant

The protocol used to study the voltage-dependence of inactivation has been successfully used in previous studies and is shown in figure 3-10, *A* (McPate et al., 2005; Zhang et al., 2011; Butler et al., 2019). From a holding potential of -70mV, a 500ms depolarising pulse to +40mV first activated then inactivated the channels. Cells were then repolarised to voltages between -140mV to +50mV in 10mV increments for 2ms which was designed to remove a proportion of inactivation from the channel, after which the membrane potential was returned to +40mV for 50ms. This step elicited a transient outward current, the expanded form of this protocol step can be seen in figure 3-10, *A*.

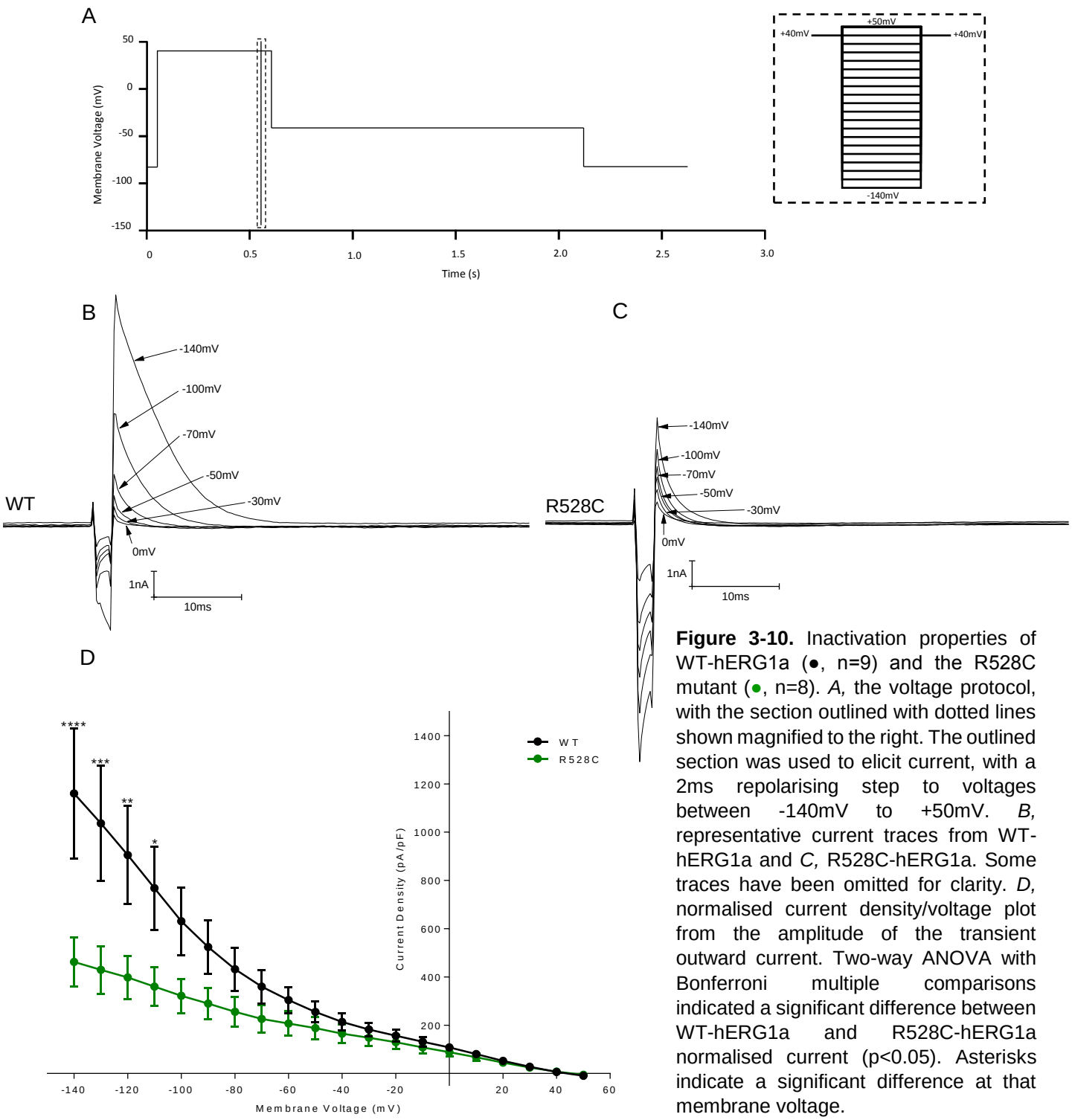

Figure 3-10. Inactivation properties of WT-hERG1a (●, n=9) and the R528C mutant (●, n=8). *A,* the voltage protocol, with the section outlined with dotted lines shown magnified to the right. The outlined section was used to elicit current, with a 2ms repolarising step to voltages between -140mV to +50mV. *B,* representative current traces from WT-hERG1a and *C,* R528C-hERG1a. Some traces have been omitted for clarity. *D,* normalised current density/voltage plot from the amplitude of the transient outward current. Two-way ANOVA with Bonferroni multiple comparisons indicated a significant difference between WT-hERG1a and R528C-hERG1a normalised current ($p<0.05$). Asterisks indicate a significant difference at that membrane voltage.

As the repolarising voltage became increasingly positive, the amplitude of the transient outward current decreased due to channel inactivation not being removed. From the representative current traces (figure 3-10, *B and C*), it can be seen that the amplitude of the outward current appeared to be of lower amplitude for R528C-hERG1a compared with that of WT-hERG1a. The amplitude of this current was measured and normalised with respect to

membrane capacitance and plotted against the repolarisation potential, see figure 3-10, *D*. Both WT-hERG1a and R528C-hERG1a current decreased as the repolarisation potential became more positive, however at more negative potentials the WT-hERG1a current was of significantly greater amplitude than that of R528C-hERG1a.

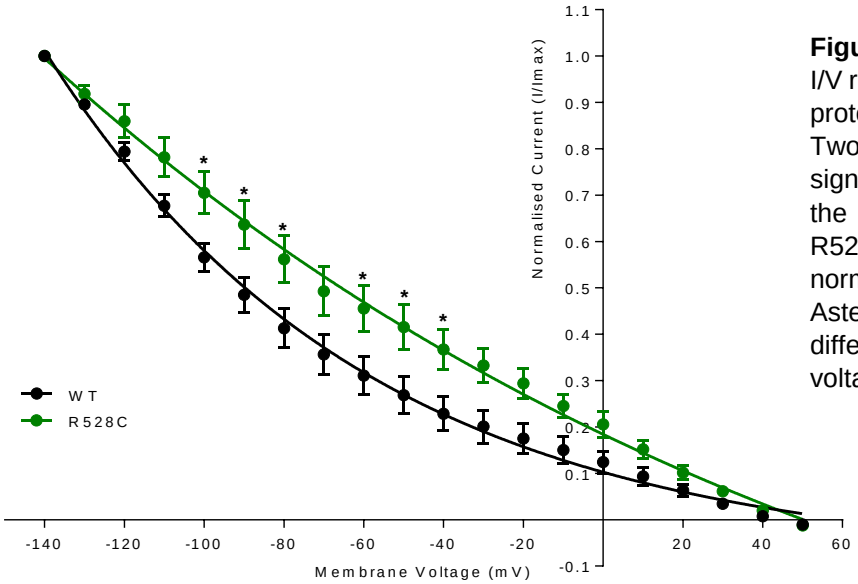

Figure 3-11. The normalised I/V relation from the inactivation protocol; the I_{hERG} availability. Two-way ANOVA indicated a significant difference between the WT-hERG1a (●, n=9) and R528C-hERG1a (●, n=8) normalised current ($p<0.05$). Asterisks indicate a significant difference at that membrane voltage.

The amplitude of this transient current was then normalised with respect to the maximum current amplitude obtained in that cell and plotted against the repolarisation potential, see figure 3-11.

The I/V relation, showing I_{hERG} inactivation/availability, indicated that a smaller amount of current was conducted by the channel as the repolarisation potential became increasingly positive due to inactivation not being alleviated. The R528C-hERG1a I/V relation was shifted rightwards relative to WT-hERG1a, and a two-way ANOVA indicated there was a significant difference between the two relations ($p<0.05$). Due to the ambiguous shape of the relations a Boltzmann relationship could not be fitted to the data, but the relative position of the curves suggests the voltage dependence of R528C-hERG1a inactivation has been positively shifted relative to WT-hERG1a.

The decay of the transient current was fitted with a mono-exponential function (McPate et al., 2005; Butler et al., 2019), and the resulting time components plotted against the repolarising potential that elicited the current transient, see figure 3-12. Decays elicited by repolarising currents more positive than -20mV were deemed too small to fit accurately.

Both time constants of inactivation exhibited voltage dependence although WT-hERG1a showed the greatest degree of change; WT-hERG1a decreased 73% across the voltage range (4.53 ± 0.60ms at -140mV to 1.20 ± 0.15ms at -20mV) whilst R528C-hERG1a decreased 61% (1.73 ± 0.32ms at -140mV to 0.68 ± 0.15ms at -20mV). For all membrane potentials the R528C-

hERG1a τ was of a smaller magnitude than WT-hERG1a, with two-way ANOVA indicating a significant effect of the R528C mutation. The smaller τ of R528C-hERG1a current inactivation suggested that R528C-hERG1a had a greater rate of development of inactivation compared with WT-hERG1a. Therefore the R528C mutation has increased the ease at which the channel can transition into the inactivated state, possibly due to an interaction between the S4 domain and the S5-P linker, which is a region of the channel believed to be involved in inactivation.

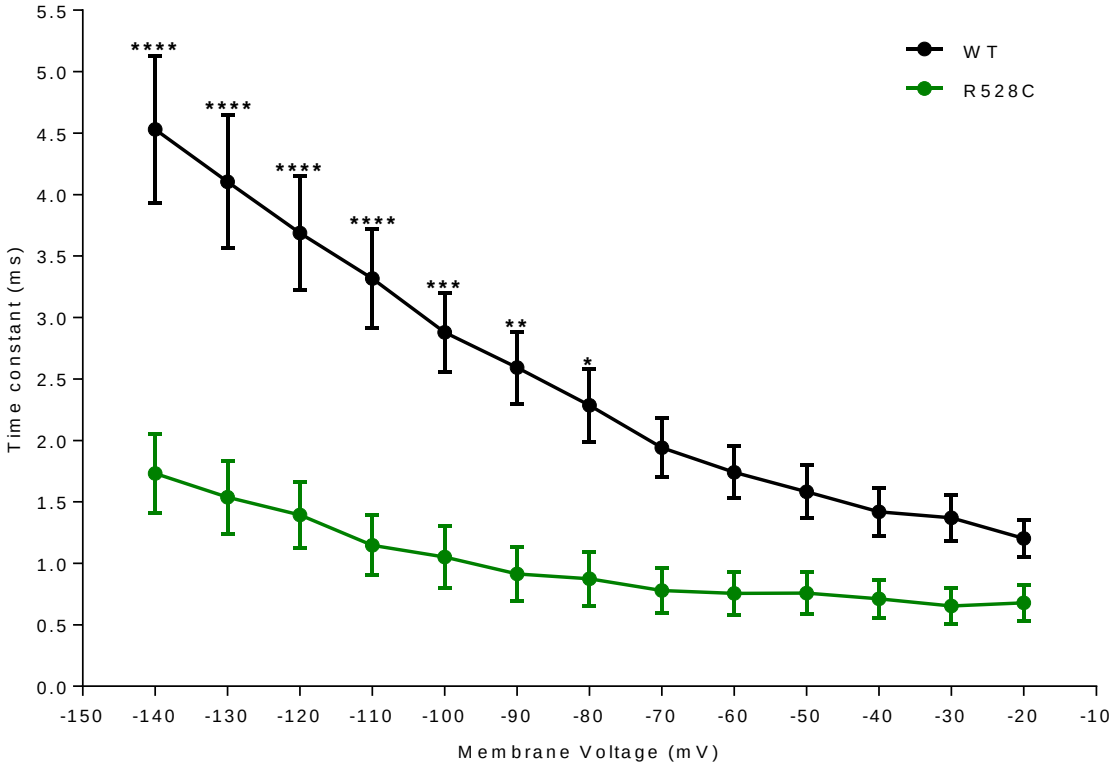

Figure 3-12. The time constants of WT-hERG1a (●, n=9) and R528C-hERG1a (●, n=8) inactivation. A mono-exponential was fitted to the decay of the I_{hERG} transient elicited by the step to +40mV from the 2ms repolarising pulse. Two-way ANOVA with Bonferroni multiple comparisons indicated a significant effect of the R528C mutation on the magnitude of the time constant ($p<0.001$). Asterisks indicate a significant difference at that membrane voltage.

3.2.4. The biophysical properties of the hERG1a-HEK293 stable cell line

Due to a UV-light source not being available on the AFM microscope, a HEK293 cell line which stably expressed the WT-hERG1a channel was used for imaging. This circumvented the need for an eGFP-marker and UV light source as all cells would be expressing the channel (Song et al., 2011; Liu et al., 2014).

To ensure that the channel being expressed by the stable cell line was comparable with that of the channel transiently expressed in the tsA201 cell line, the previous voltage protocols were

used to produce an activation curve from the normalised tail currents (see figure 3-13, *A*) and a fully activated I/V relationship from the peak current (see figure 3-13, *B).*

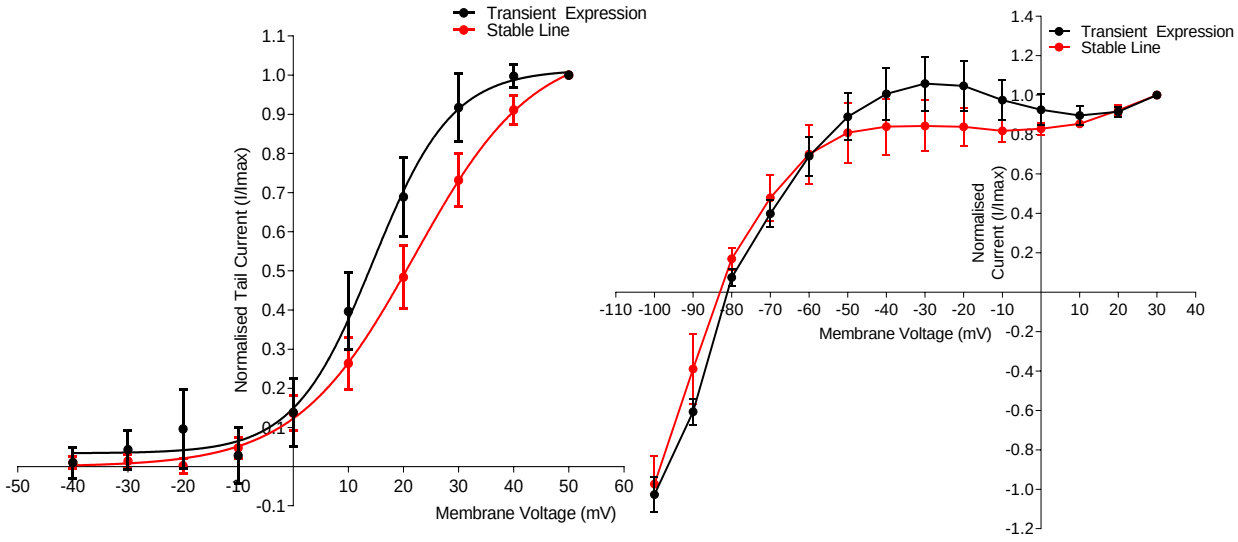

Figure 3-13. Ionic current of the transiently expressed WT-hERG1a (●, n=8) and the HEK293 stable line (●, n=6). *A,* The activation curve of the two different variants of expression, two-way ANOVA with Bonferroni multiple comparisons concluded there was no significant difference between the two at any membrane voltage (p=0.4674). *B,* Fully activated I/V plot of the two variants of expression, two-way ANOVA with Bonferroni multiple comparison tests concluded there was no significant difference at any membrane voltage (p=0.6964). Unpaired t-test found no significant difference between either the $V_{0.5}$ or *k* of the WT and stable line current (p>0.05).

The activation curve from the current of both cell lines (figure 3-13, *A*) followed a sigmoidal relationship which could be fitted with a Boltzmann function, allowing $V_{0.5}$ and k to be determined. Two-way ANOVA found no significant difference between I_{hERG} for the two expression variants, while an unpaired t-test found no difference between the $V_{0.5}$ and k values (the $V_{0.5}$ and k values for WT-hERG1a, R528C-hERG1a and the stable cell line are summarised in table 3-1).

	WT	**Stable**	**R528C**	**One-way ANOVA**
$V_{0.5}$ (mV)	15.2 ± 5.7	22.3 ± 3.9	18.1 ± 2.2	P > 0.05
k (mV)	9.4 ± 0.56	8.9 ± 0.95	10.4 ± 0.93	P > 0.05

Table 3-1. Mean $V_{0.5}$ (half maximal activation voltage) and k (slope) values from Boltzmann functions fitted to each cell. One-way ANOVA with Bonferroni multiple comparisons of the respective values concluded there was no difference between them, and hence no difference in the activation of either WT, the stable cell line or the R528C mutant.

The fully activated I/V relationships (figure 3-13, *B*) again followed a similar pattern; I_{hERG} increased as the command voltage became more depolarised (E_K being approximately -81mV), reaching a maximum amplitude between -40 and -30mV. I_{hERG} then decreased as the membrane potential became more positive due to channel inactivation. Two-way ANOVA

indicated there was no significant difference between the fully activated I/V relations of the two cell lines at any membrane potential.

In summary, despite being one being transiently expressed in a tsA201 cell line and the other being stably expressed in a HEK293 cell line, there was no difference between the overall I_{hERG}. This allowed comparison between AFM images obtained using the stable cell line and any conclusions drawn from the transiently expressed channel current.

3.3. Discussion

3.1.1. The effect of the R528C mutation on the activation of I_{hERG}

The half-maximal activation voltage of activation for both WT-hERG1a and R528C-hERG1a found here are considerably more depolarised than those found previously. The half-maximal activation voltage of WT-hERG1a is generally accepted to be -25mV (Zhou et al., 1998; Vandenberg et al., 2012), but has also been found to be more depolarised (Zhang et al., 2011; Butler et al., 2019), closer to the value found here of +15.2mV. The R528C-hERG1a half-maximal voltage of activation has been less well characterised but has been found to be +1.0mV by Zhang et al., 2004 and +33.5mV by Elliott et al., 2009. in contrast to +18.1mV calculated from the data presented here.

This could be due to a number of factors, such as the cell type used for channel expression. Differences in I_{hERG} could be due to the intrinsic variability of synthesis, folding and trafficking which could lead to differences in the functional properties of the channel (Vandenberg et al., 2012). Differences in temperature, the composition of the recording solutions and the recording techniques themselves could all account for variation in results.

Despite the variability, the data presented here suggests that the R528C mutation has no statistically significant effect on the voltage dependence of activation of I_{hERG}, despite a slight depolarising shift in the activation curve and resulting $V_{0.5}$. This is supported by the findings of Elliott et al., 2009 who concluded that though the R528C mutation did positively shift the voltage dependence of activation, this difference was found not to be statistically significant.

Contrastingly, an R528D mutation (arginine to aspartic acid) was found to not shift the voltage dependence of activation, but instead produced a ‘pedestal’ component of channel activation; a delay in the decrease of tail current amplitude at hyperpolarised potentials. The authors suggested this reflected the bulky side chain of aspartic acid inhibited the closure of the activation gate at negative voltages, resulting in more current being conducted at these potentials (Zhang et al., 2005).

The R528D mutation was found to significantly decrease the rate of activation, in contrast to the data presented here which suggests that R528C increased the rate of channel activation. Mutation of R528 to glutamine (R528Q) increased the rate of activation and positively shifted $V_{0.5}$ of activation, similar to R528C (Subbiah et al., 2004). The cysteine and glutamine residues may not hinder the movement of S4, being non-polar molecules and less bulky than that of aspartic acid and arginine. A faster rate of S4 movement would be reflected in a faster rate of activation, but the lack of one charged residue in S4 would mean a greater voltage gradient would be required to activate the channel; reflected in the depolarising shift of the $V_{0.5}$ of activation seen in R528C.

The kinetics of I_{hERG} activation have also been studied extensively in WT and varying mutants using an 'envelope of tails' protocol. A depolarising pulse of increasing duration is used to elicit tail currents, the normalised amplitude of which is then plotted against pulse duration and fitted with an exponential (Trudeau et al., 1995; Ridley et al., 2003; McPate et al., 2005; Zhang et al., 2011; Butler et al., 2019). This method has been shown to produce a τ of activation different from that obtained using the method outlined here, therefore future characterisation of R528C would benefit from using the envelope of tails method (Zhou et al., 1998).

3.3.2. The effect of the R528C mutation on I_{hERG} and its deactivation

The data presented suggests that the E_{Rev} of R528C-hERG1a current was more depolarised relative to WT-hERG1a current. This is supported by a calculated increase in permeability to Na^+ ions relative to K^+ ions but is in contrast to previous findings (recorded in oocytes) that R528C and WT E_{Rev} were no different (Zhang et al., 2004). This change in the relative permeability suggests that mutating R528 can affect the permeability of the channel, possibly through interactions with the selectivity filter of the channel. Due to R528 being a considerable distance from the selectivity filter such an effect is more likely a consequence of perturbation of S4 movement which in turn will modulate an allosteric interaction between the S4 helix and the selectivity filter, rather than a direct effect on the selectivity filter (Zhang et al., 2011). However this highlights how interlinked the domains of the hERG channel are, as a mutation in S4 can modulate the selectivity filter of the channel pore.

The fully activated I/V relation suggests that R528C-hERG1a current had a significantly decreased current density relative to WT-hERG1a. Fougere *et al.* concluded that an R582C mutation (in the S5-P linker) resulted in decreased expression of the channel due to abnormal trafficking. Incubation of R582C-transfected HEK 293 cells at 30°C was found to rescue the cell surface expression to near WT levels, while R582C expression in oocytes was found to be largely unaffected at any temperature (Fougere et al., 2011). This again raises the point that different expression systems will result in variations in protein expression, alongside the fact

that single point mutations can have a significant effect on channel biogenesis (Vandenberg et al., 2012).

However, an error in biogenesis is unlikely to be the reason for a decreased current density given that the R528C-hERG1a gating current amplitude was found to be equal to or greater than WT-hERG1a, implying that the same or indeed greater number of R528C-hERG1a channels were present (see chapter 4). Therefore, the decrease in current density of R528C-hERG1a was due to the channel rapidly shifting into the inactivated state after activation as a result of the accelerated inactivation rate. If more channels were in the non-conducting inactivated state at a given membrane potential, there would be less current recorded than in WT-hERG1a channels which remained in the activated conducting state for longer.

The deactivation rate of R528C was found to be decreased, though not due to either the fast or the slow component specifically, so may have been due to an equal slowing of both fast and slow deactivation components given the uncertainty of the measurement of the slow component. This is supported by the findings of Subbiah *et al.* who found that the deactivation rate, was slightly decreased compared with WT-hERG1a.

The R528D mutation was found to cause a significant decrease in the rate of deactivation (Zhang et al., 2005). As the aspartic acid and cysteine mutations both had a similar effect of slowing the deactivation kinetics, this would suggest that R528 has a role in hERG deactivation. The mutations may affect the rate of S4 movement through the open and closed states, with the loss of R528 hindering the formation of charge pairings between S4 and S1-S3 which usually facilitate the stabilisation of the deactivated state of S4 (Subbiah et al., 2004; Jiang et al., 2005; Vandenberg et al., 2012). Taking into account the increased activation kinetics yet slowed deactivation kinetics, this suggests that the R528C mutation may destabilise the deactivated state with the channel preferentially transitioning to the activated state and only slowing transitioning back to the closed state.

3.3.3. The effect of the R528C mutation on the inactivation of I_{hERG}

R528C-hERG1a was found to have a positively shifted voltage-dependence of inactivation and an increased rate of development of inactivation relative to WT-hERG1a (deduced from the τ of inactivation for R528C-hERG1a being significantly smaller).This suggests that R528C-hERG1a needed greater voltage gradient in order to recover from inactivation, indication that the S4 domain has a role in channel inactivation (Piper et al., 2003).

hERG inactivation has been theorised to be analogous to C-type inactivation, where protein-protein interactions leads to collapse of the selectivity filter of the channel, resulting in blockage of the pore (Smith et al.,1996) . C-type inactivation is found in many voltage-gated potassium

channels, however the speed at which inactivation takes place in hERG is of several orders of magnitude faster for reasons that remain to be elucidated. (Perrin et al., 2008; Zhou et al., 2011).

The S5-P linker (residues 571-613) is generally accepted as the region responsible for hERG fast inactivation rather than the S4 voltage sensor (Fougere et al., 2011; Zhou et al., 2011). Mutations such as S620A causes a dramatic +100mV shift in the $V_{0.5}$ of inactivation, whilst N588K and S631A result in complete deficiency of inactivation, with the latter leaving activation unaffected (Piper et al., 2003b, 2005a; Perrin et al., 2008). R528, being in the S4 voltage sensor region, will only exert an effect on inactivation through allosteric interactions between itself and the S5-P linker. This may account for the relatively small differences in the inactivation of R528C-hERG1a compared to WT-hERG1a found here. However, this again highlights the interlinked nature of the domains of hERG, and how a mutation in one domain may have consequences on the function of other domains.

3.4 Conclusion

Overall, the R528C mutation had a small effect on the ionic current of hERG1a. Given its position in the S4 voltage sensor it was unlikely that there would be abolishment of or a large effect on inactivation. Whilst R528 has been identified as an important contributor to the voltage-sensing capability of S4, its neutralisation had only a small effect on the voltage dependence of activation and deactivation. This suggests that R528's position in the midst of the positive residues in S4 allows the overlapping positive charges from neighbouring residues to facilitate the movement of S4 out of the lipid bilayer when the positive arginine residue has been neutralised (Subbiah et al., 2005; Zhang et al., 2005). However the mutation may destabilise the deactivated state of S4, resulting in the slowed deactivation kinetics, and facilitate transition into the inactivated state, reflected in the accelerated inactivation kinetics.

4. WT, R528C and N588K-hERG1a gating currents

4.1 Introduction

4.1.1 Charged particles and gating currents

The idea of a charged particle moving across a membrane in response to depolarisation was first proposed by A.L. Hodgkin and A.F. Huxley in 1952. They proposed the existence of gating particles which moved from a non-permissive to permissive state to facilitate the conduction of ions (Hodgkin and Huxley, 1952). Many others have used the proposals of Hodgkin and Huxley as a basis for their research, and as a result our understanding of the gating of voltage-gated ion channels has grown.

The general consensus is that a depolarising step of the membrane potential causes positively charged amino acid residues within the membrane field to move outwards. This simultaneously opens the ion channel and produces a transient outward current. First recorded from sodium channels expressed in isolated giant squid axons, gating currents have now been recorded from numerous voltage-dependent proteins and are believed to represent the movement of the voltage sensor through the membrane field in order to open the ion channel (Armstrong, 1981; Bezanilla, 2018).

The cloning of sodium channels from rat brain and *Drosophila* identified the S4 domain as a possible voltage sensor as the sequence was found to have a positively charged arginine or lysine residue every three amino acids (Noda et al., 1984, 1986; Salkoff et al., 1987). Mutation of these S4 positive residues into either non-polar or negatively charged amino acids reduced the slope of the activation curve of the channel; therefore the mutations had reduced the equivalent gating charge. This was indication that the positively charged residues in S4 enabled the domain to act as the voltage sensor of activation for the channel (Stuhmer et al., 1989). Further cloning studies confirmed that the positively charged residues in S4 were conserved across voltage gated calcium and potassium channels, suggesting that voltage-gated channels share this common mechanism of activation, see figure 4-1.

The gating currents that arise from the movement of the now identified voltage sensor of activation (S4) have since been used by a variety of approaches to elucidate conformational changes of proteins. Analysis of gating current kinetics and voltage dependence and gating charge magnitude, in combination with techniques such as voltage-clamp fluorimetry (VCF) have, in some cases, allowed gating mechanisms of proteins to be proposed (Catterall, 2000; Bezanilla, 2018; DeCoursey, 2018).

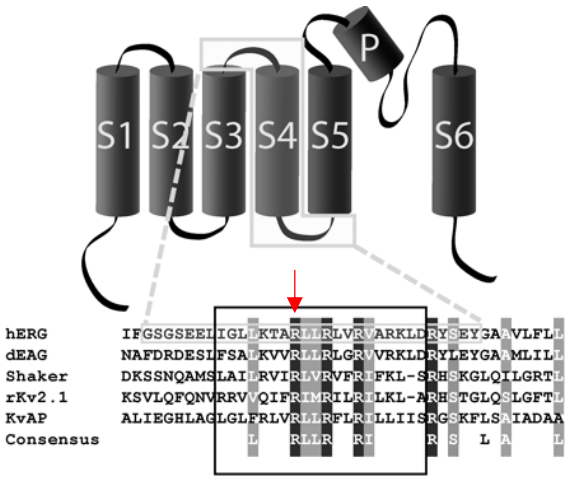

Figure 4-1. The S4 voltage sensor sequence is highly conserved across K_V channels. Outlined in the black box is the S4 sequence of hERG aligned with the *Drosophila* EAG channel, Shaker, rat $K_V2.1$ and K_VAP. Conserved residues and identical residues are shown shaded grey and black, respectively. R528 is highlighted with a red arrow. Adapted from Piper et al., 2004.

4.1.2 hERG1a and gating currents

The recording of gating currents presents a unique set of challenges; ionic currents must be inhibited through blockade of the ionic channel (either pharmacologically or use of impermeant ions), capacitive and leak currents must be correctly compensated for and a high temporal resolution is required (Armstrong, 1981; Bezanilla, 2018).

In addition, hERG1a activation kinetics occur over a longer time course than other voltage-gated potassium channels such as *Shaker*, putatively due to slow movement of the S4 voltage sensor (Cheng and Claydon, 2012). As a consequence of this slower time scale the gating currents are harder to resolve as they are at risk of being lost in the background noise of the recording.

Regardless of this, hERG gating currents have been previously recorded both in oocytes (using the cut-open oocyte voltage clamp technique) and in mammalian cells (Piper et al., 2003b; Ferrer et al., 2006; Fedida et al., 2012; Wang et al., 2013; Goodchild and Fedida, 2014; Goodchild et al., 2015; Dou et al., 2017). These gating currents have been used to suggest gating mechanisms behind the slow activation of hERG, as well as proposals for the mechanism of hERG inactivation.

4.1.3 The N588K-hERG1a inactivation mutant

The R528C-hERG1a mutant (characterised in chapter 3) is proposed to have an altered gating charge from that of WT-hERG1a channels as a result of the neutralisation of one of the positively charged S4 residues (see figure 4-1). To investigate the effect of inactivation on the gating currents an inactivation-deficient hERG mutant was required. The N588K mutant was chosen, which has already been characterised in terms of ionic current but not gating current.

N588K-hERG1a was first identified in patients with genetically linked SQTS (short QT syndrome), and is a point mutation in the S5-P linker (turret region) of the channel (see figure 4-2) (Hong et al., 2005). The voltage dependence of inactivation of N588K-hERG1a current has been shifted approximately +60mV compared with WT-hERG1a current. Therefore its inactivation is no longer at physiologically relevant potentials and hence it can be considered inactivation deficient. The depolarising shift in inactivation results in a lack of inward rectification of I_{hERG} over the 0 to -100mV range, resulting in N588K-I_{hERG} increasing proportionally as potentials become more depolarised (Cordeiro et al., 2005; McPate et al., 2005; Grunnet et al., 2008).

As previously stated (see chapter 1), the lack of inward rectification results in N588K-hERG1a conducting a repolarising current during the plateau phase of the cardiac action potential which cuts the action potential short, resulting in arrythmia and less commonly fibrillation (Hong et al., 2005; Grunnet et al., 2008; Loewe et al., 2014).

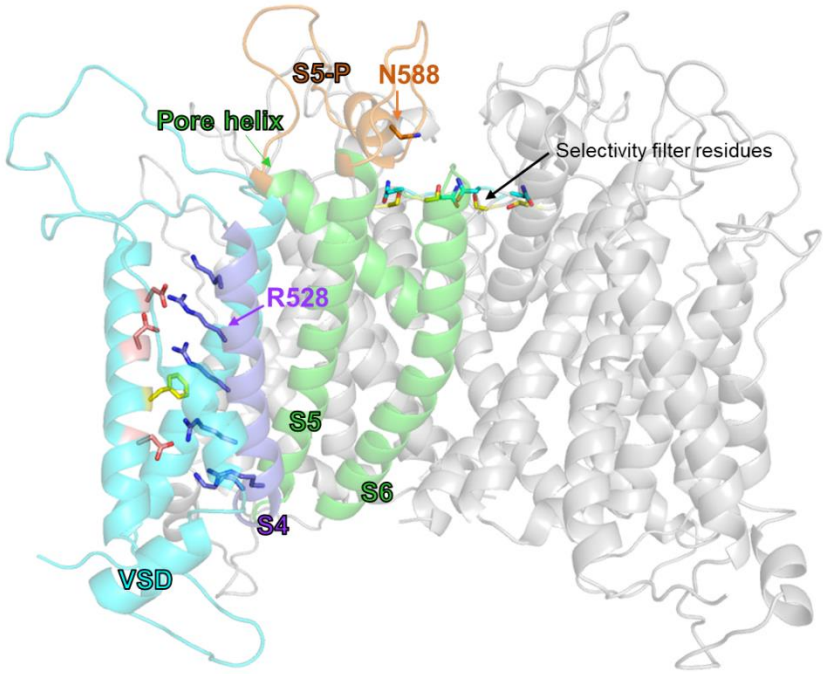

Figure 4-2. The position of the two mutations in the hERG channel used in this project. The arginine at position 528 can be seen in the S4 domain (coloured purple) and was mutated to a cysteine. The asparagine at position 588 can be seen in the S5-P linker (turret region, coloured orange) and was mutated to a lysine. The VSD is shown in blue and the S5 and S6 helices in orange. The remaining 3 channel subunits have been shaded in grey for clarity. Structural images were provided by Dr. Christopher Dempsey, University of Bristol.

The aims of this chapter are to present recordings of gating currents from WT-hERG1a and compare these with the gating currents recorded from the R528C-hERG1a mutant and the N588K-hERG1a inactivation deficient-mutant.

4.2 Methods for recording gating currents

Gating currents have been previously recorded in oocytes (Fedida et al., 2012; Goodchild et al., 2015) and in tsA201 cells (Wang et al., 2013). Oocytes have been tended to be used more as their high protein expression levels lend to easier recording of the small amplitude gating currents (Sigel, 1990). Even when using this expression system, the parameters and

conditions were adjusted from the recording of ionic currents to be able to resolve the gating currents. Figure 4-3 shows the main adjustments, aside from the ionic compositions of the internal and external recording solutions, that were made to the recording conditions in order to isolate gating currents in the mammalian tsA201 cells used in this project.

Figure 4-3 *A* shows the voltage protocol used to elicit gating currents. Cells were depolarised from a holding potential of -100mV to potentials between -60mV to +60mV at 10mV intervals for 50ms, which elicited the on gating current due to the activation of channels. After 50ms cells were returned to the holding potential; this transition elicited the off gating current due to channel deactivation.

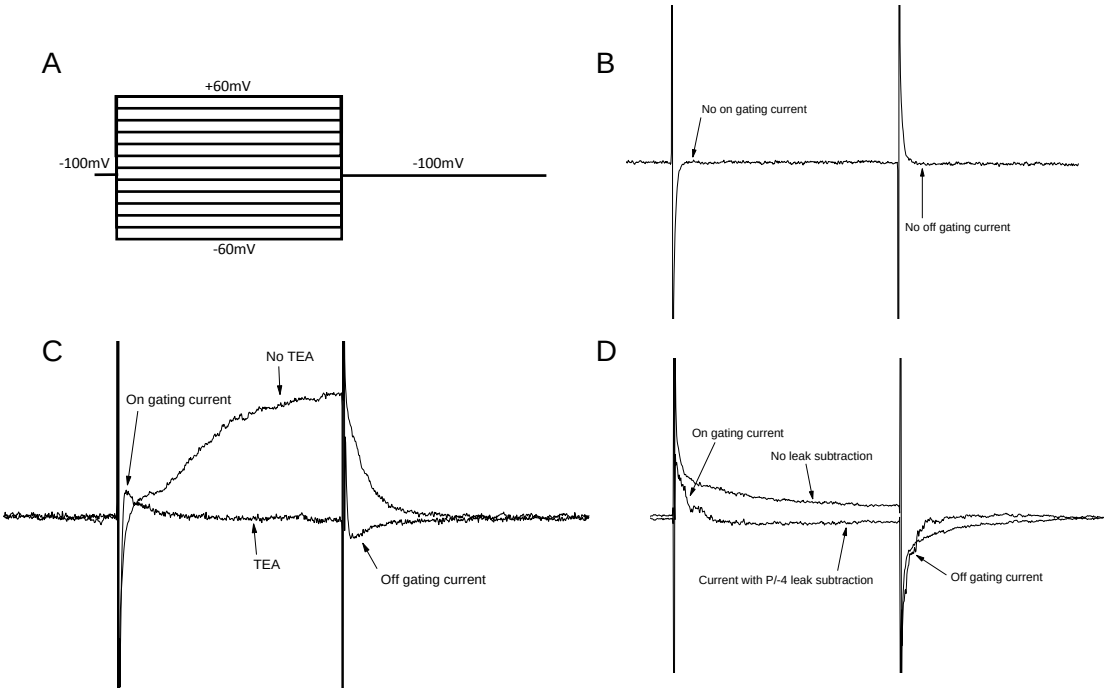

Figure 4-3. Recording of gating currents from WT-hERG1a transiently expressed in tsA201 cells. *A,* Protocol used to elicit gating current. Cells were held for 50ms at a holding potential of -100mV then depolarised to voltages between -60mV and +60mV at 10mV intervals for 50ms, then repolarised to -100mV for 200ms. *B,* Representative current trace at +60mV from non-transfected cells showing that no gating current could be elicited. *C,* TEA (150mM) was added to the external solution in order to eliminate any residual ionic current. This is demonstrated with current traces before and after the addition of TEA at +60mV, showing the presence of on and off gating currents. *D,* A P/-4 leak subtraction protocol was applied in order to further resolve gating current, shown with representative current traces at +60mV.

As a negative control, currents were recorded from non-transfected tsA201 cells using an identical protocol see figure 4-3, *B*. As predicted no currents, gating or ionic, were recorded.

In order to resolve gating current from ionic current, 150mM TEA was added to the external recording solution while 150mM NMDG was added to the internal solution (Wang et al., 2013). NMDG is a non-permeant cation and TEA is a non-selective potassium channel blocker and their presence was intended to prevent the hERG1a channel conducting ions (either Na^+ or

K^+) (Bisset and Chung, 2008). Therefore, any recorded current would be due to the movement of charged residues across the membrane field. The effect of the addition of TEA to the external solution can be seen in figure 4-3, *C*. With no TEA only ionic current can be seen, after the addition of TEA the ionic current component has been removed and the relatively small amplitude gating current can now be seen. A -P/4 protocol was applied to further isolate the gating current, the effect of which can be seen in figure 4-3, *D*.

Previous papers have also added a further channel blocker such as terfenadine or MK-499 (Piper et al., 2003b; Wang et al., 2013; Goodchild et al., 2015). However with the addition of 0.01mM terfenadine to the external solution recordings became unstable and no gating current could be recorded. This may be due to mammalian tsA201 cells being less able to withstand the effects of terfenadine compared with oocytes.

4.3 Results

4.3.1 Gating currents of the WT-hERG1a channel

Gating currents were successfully recorded from WT-hERG1a and could be resolved from approximately -10mV, at which point a transient outward current was recorded. The amplitude of this transient increased as the depolarising pulse became more positive. The current decayed across the 50ms pulse, at which point repolarisation to the -100mV holding potential elicited a transient inward current. WT-hERG1a gating currents exhibited an asymmetric profile with off gating currents being of greater amplitude than the on gating currents, see figure 4-4. The decay of both on and off gating currents at +60mV were fitted with a biexponential function, see figure 4-4, *inset*.

The normalised amplitude of the WT-hERG1a gating currents were plotted against the membrane voltage and the resulting relationship was fitted with a Boltzmann function, see figure 4-5, *A and B*.

As the command pulse became more depolarised the amplitude of the gating current increased, both for on and off gating currents. The gating currents only became discernible at potentials above approximately -20mV, which is generally the membrane potential at which some degree of voltage dependence on the I-V relations could be observed. The current amplitudes increased as potentials became more depolarised, though this was more obvious in the on gating current. The parameters derived from the Boltzmann fit of the currents were as follows; on gating current $V_{0.5}$ = 41.4mV ± 9.1mV, k = 22.7mV ± 2.2mV. Off gating current $V_{0.5}$ = 6.3mV ± 5.1mV, k = 16.2mV ± 1.8mV. Unpaired t-test found there to be a significant

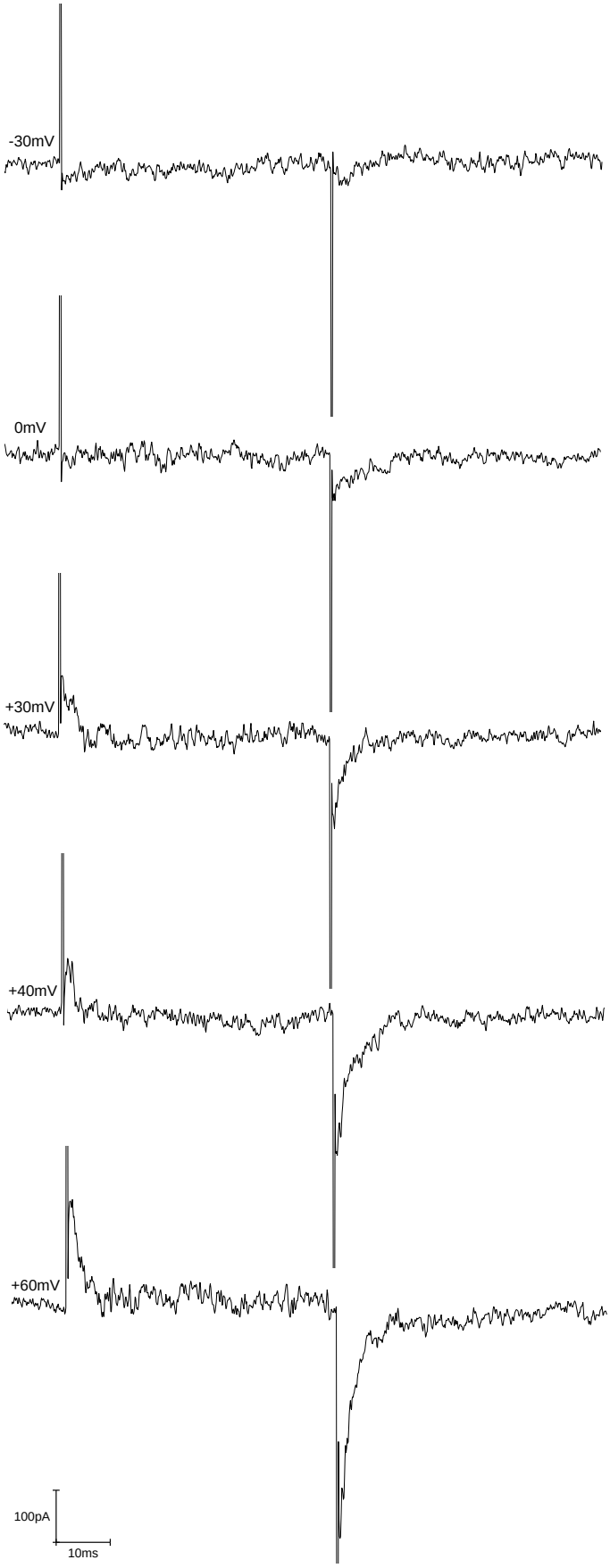

Figure 4-4. Representative gating current traces from the WT-hERG1a ion channel. Shown are traces from depolarising pulses to -30, 0, +30, +40 and +60mV, where the asymmetry of the WT gating current can be seen. *Inset* shows the biexponential fitting (grey) of the gating current at +60mV. For on gating current τ_1 = 2.1ms ± 0.6ms, τ_2 = 4.4ms ± 0.4ms. For off gating current τ_1 = 0.6ms ± 0.2ms, τ_2 4.4ms ± 3.9ms.

difference between the on and off Boltzmann parameters ($p<0.05$). This highlights the difficulty resolving the on and off gating currents in mammalian cell lines, as the Boltzmann parameters

of the on and off gating currents should be no different from each other, indicating a significant amount of error was associated with current measurements.

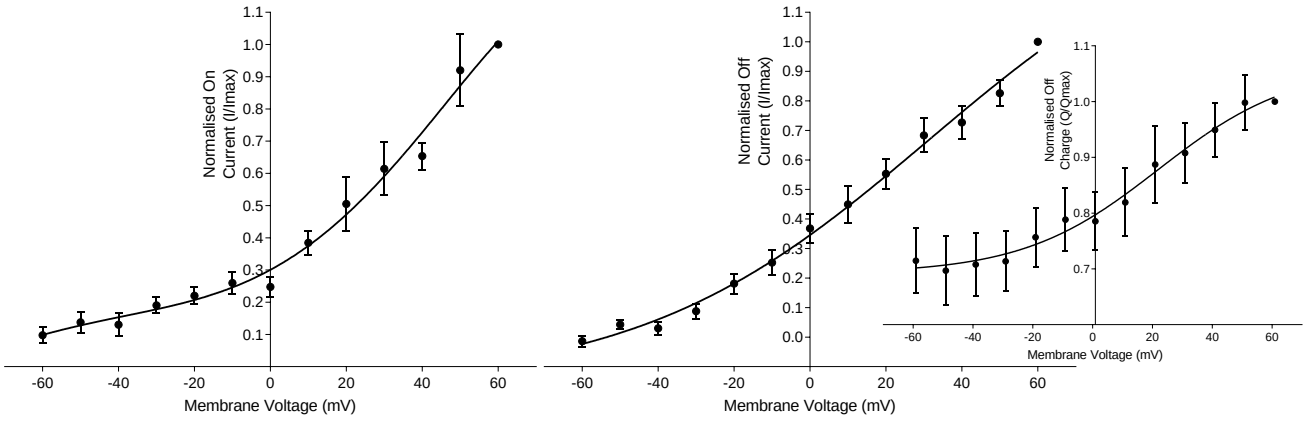

Figure 4-5. The normalised on *(A)* and off *(B)* gating current amplitude, and off gating charge *(inset)* from WT-hERG1a. Relationships were fitted with a Boltzmann function, on gating current $V_{0.5}$ = 41.4mV ± 9.1mV, k = 22.7mV ± 2.2mV. Off gating current $V_{0.5}$ = 6.3mV ± 5.1mV, k = 16.2mV ± 1.8mV. Off gating charge $V_{0.5}$ = 15.5mV ± 9.2mV, k = 16.7mV ± 5.1mV. Unpaired t-test found there to be a significant difference between on and off parameters derived from the current, but no significant difference between those derived from current and those derived from charge.

Gating charge was measured through the integration of the areas under the gating current traces. The on gating charge appeared not to exhibit strong voltage dependence, however the off gating charge displayed a more obvious positive slope. Only the off gating charge could be fitted with a Boltzmann function, see figure 4-5, *inset*, with the derived parameters being $V_{0.5}$ = 15.5mV ± 9.2mV, k = 16.7mV ± 5.1mV. An unpaired t-test found there to be no difference between the Boltzmann parameters derived using current and those using charge, therefore for the purposes of this project they can be considered equivalent.

Previous publications have plotted normalised gating current amplitude against normalised ionic current to demonstrate that the movement of S4 (shown by the gating current) occurs at more hyperpolarised potentials than (and so occurs prior to), the conduction of ions through the channel pore (Piper et al., 2003b; Wang et al., 2013; Goodchild and Fedida, 2014; Goodchild et al., 2015). However when plotted the gating current presented here did not exhibit this hyperpolarised shift relative to the ionic I/V relation. This perhaps indicates that in a mammalian cell line gating currents are more difficult to resolve especially at negative potentials, compared with recordings using the cut-open oocyte voltage-clamp technique.

4.3.2 R528C-hERG1a gating currents

Gating currents were recorded from the R528C-hERG1a mutant. As in WT-hERG1a, an outward transient current was seen upon depolarisation while an inward transient was seen upon repolarisation (see figure 4-6). The amplitude of this current transient exhibited voltage dependence, with the amplitude increasing as the command potential became more depolarised. Decays of both on and off gating currents at +60mV were fitted with a biexponential function, see figure 4-6, *inset*.

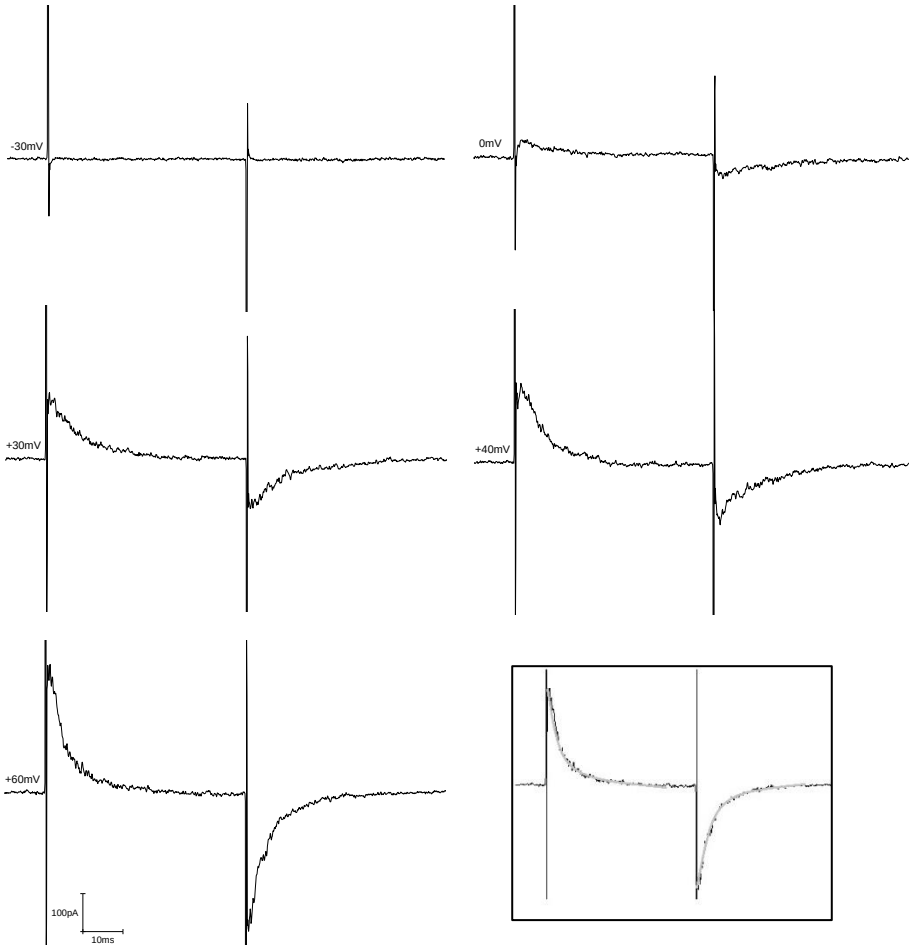

Figure 4-6. Representative gating current traces from the R528C-hERG1a ion channel. Shown are traces from depolarising pulses to -30, 0, +30, +40 and +60mV. *Inset* shows the biexponential fitting (grey) of the gating current at +60mV. For on gating current τ_1 = 3.3ms ± 1.5ms, τ_2 = 9.1ms ± 4.5ms. For off gating current τ_1 = 2.3ms ± 0.9ms, τ_2 5.9ms ± 2.2ms.

The normalised amplitude of the on and off gating currents were plotted against the membrane potential and the relationships fitted with a Boltzmann function, see figure 4-7.

Both on *(A)* and off *(B)* gating currents exhibited voltage dependence, with the amplitude of current increasing as membrane voltage became more depolarised. The I/V relations of both on and off gating currents were fitted with a Boltzmann function; $V_{0.5}$ and k from the on gating currents were 35.7mV ± 9.0mV and 17.0mV ± 3.8mV, respectively. The same parameters derived from the off gating current were 32.6mV ± 10.7mV and 17.3mV ± 3.8mV. Unpaired t-test performed on both parameters found there to be no difference between the $V_{0.5}$ and k of on and off R528C gating currents.

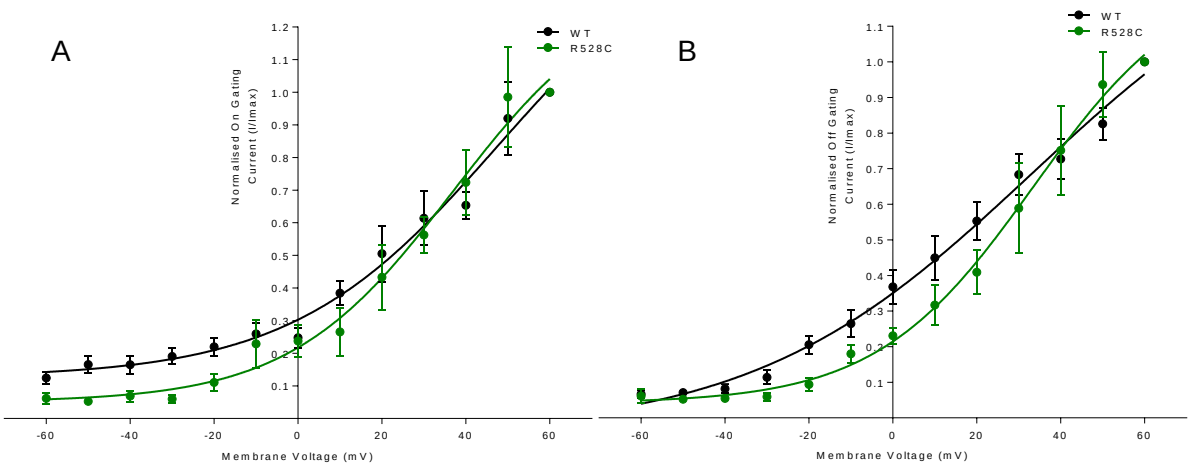

Figure 4-7. The normalised on and off gating currents from R528C-hERG1a channels relative to WT-hERG1a. Both on gating currents (*A*) and off gating currents (*B*) were fitted with a Boltzmann function. For on gating current $V_{0.5}$ = 35.7mV ± 9.0mV, k = 17.0mV ± 3.8mV. For off gating current $V_{0.5}$ = 32.6mV ± 10.7mV, k = 17.3mV ± 3.8mV. Unpaired t-test found there to be no significant difference between the derived parameters of on and off gating currents.

When compared with WT-hERG1a, unpaired-t test found a significant difference between the $V_{0.5}$ of the off gating current, with the $V_{0.5}$ of R528C-hERG1a being positively shifted compared with the $V_{0.5}$ of WT ($p<0.05$). Both on and off R528C-hERG1a gating currents exhibited a depolarising shift relative to WT-hERG1a gating currents (see figure 4-7, *A and B*), aligning with the finding that the ionic current of R528C activates at more depolarised potentials compared with WT-hERG1a channels. The slopes of WT-hERG1a on and off gating current (as measured by the k value) was found to be statistically no different from that of R528C, in contrast to the finding that R528C-hERG1a ionic current has an accelerated activation rate compared with WT-hERG1a.

4.3.3 The gating currents of the N588K-hERG1a mutant

Gating currents were recorded from N588K-hERG1a, of which the representative current traces can be seen in figure 4-8. Unlike WT-hERG1a and R528C-hERG1a gating currents, the decays of the on and off gating currents recorded from N588K-hERG1a were fitted with a monoexponential decay, see figure 4-8, *inset.*

Using the amplitude of the on and off gating currents, I/V relations were plotted and fitted with a Boltzmann function, see figure 4-9. Both on and off N588K-hERG1a gating I/V relations closely resembled that of WT-hERG1a, showing no shift in the *x* axis and no obvious difference in the slope. Unlike the I/V relations of WT-hERG1a and R528C-hERG1a, the on I/V relation of N588K-hERG1a was best fit with a double-Boltzmann function (figure 4-9, *A*). Similarly, WT-hERG1a gating charge-voltage relationships have previously been fitted with a double-Boltzmann function which was attributed to there being two charge components underlying

hERG gating which move at different potentials (Wang et al., 2013). The double-Boltzmann parameters found here show a depolarising shift relative to those found previously ($V_{0.5\text{-}1}$ = -35.6mV, k_1 = 5.6mV, $V_{0.5\text{-}2}$ = +28.9mV, k_2 = 14.5mV) by Wang et al., indicating that the small gating currents at hyperpolarised potentials may not have been sufficiently resolved, and instead were lost in the background noise of the recording.

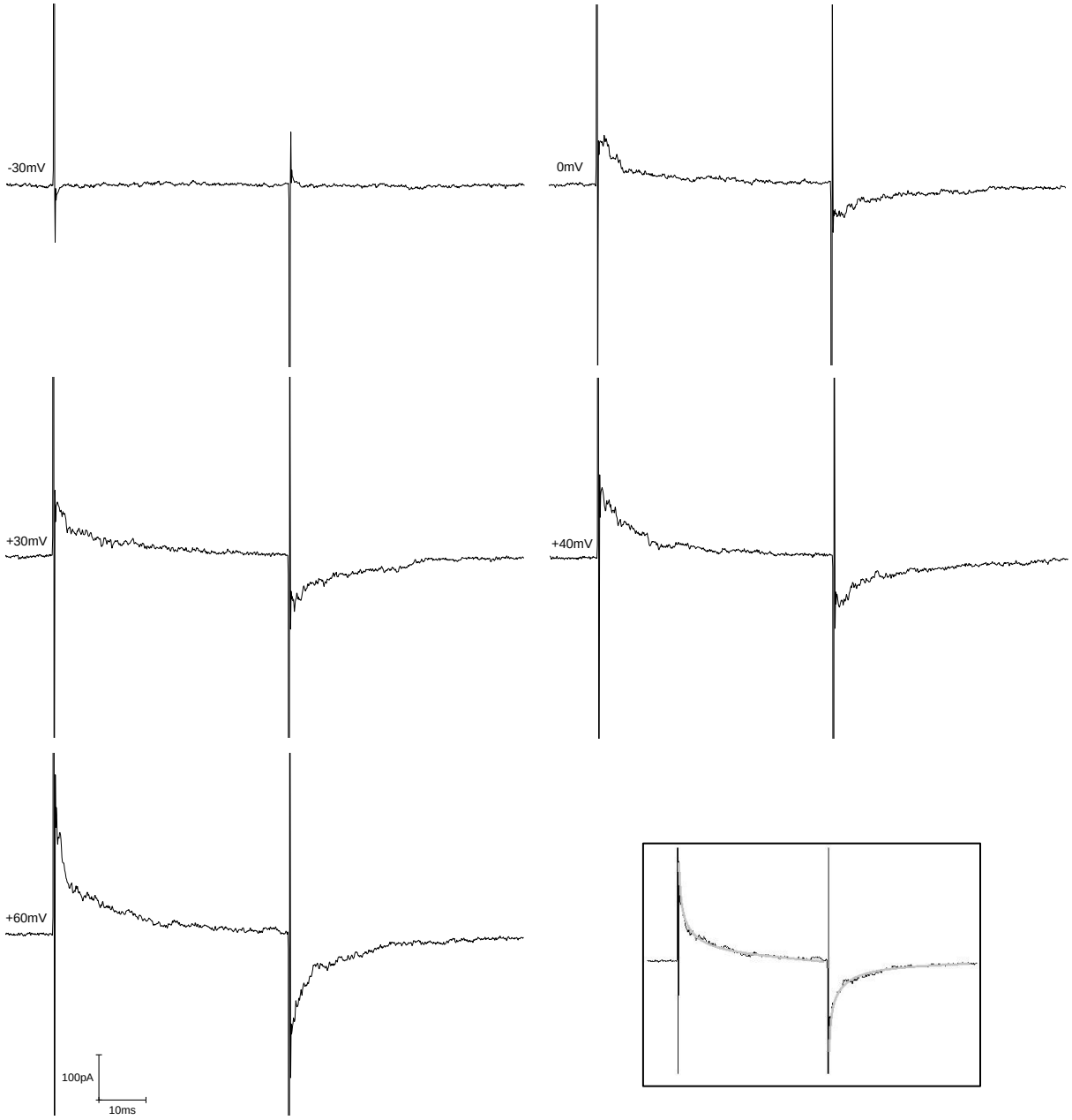

Figure 4-8. Representative gating currents of the N588K-hERG1a mutant. Both on and off current decays at +60mV were fitted with a monoexponential decay (see *inset*, grey trace). For on gating currents, τ_1 = 3.23ms ± 1.31ms, for off gating currents τ_1 = 2.29ms ± 0.47ms

Due to the large error associated with measuring small currents combined with a small sample size one a double-Boltzmann function could not be fitted to the off I/V gating relation. Therefore

a single Boltzmann function was fitted (figure 4-9, *B*). Unpaired t-test found there to be no significant difference between the Boltzmann function parameters derived from WT-hERG1a off gating currents and N588K-hERG1a off gating currents.

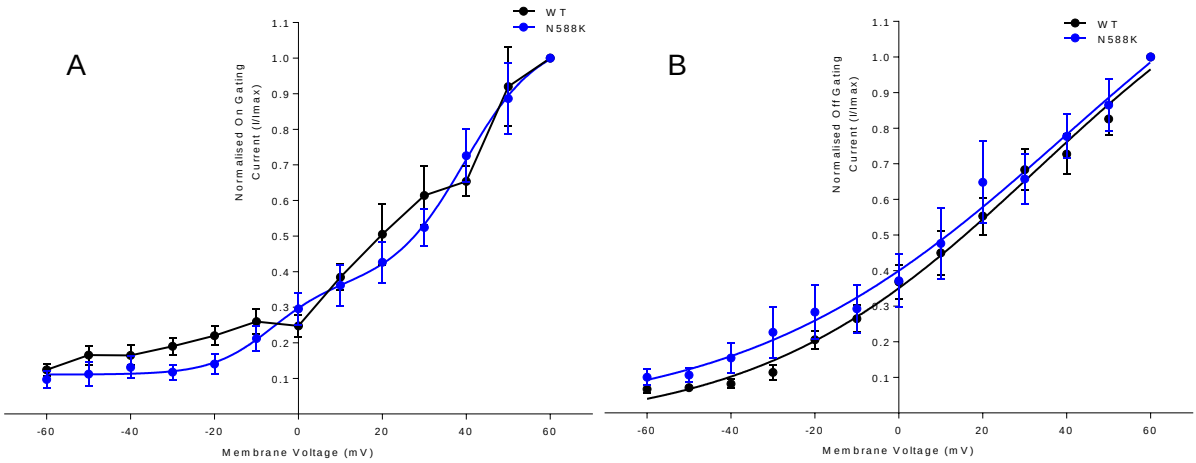

Figure 4-9. The I/V relations for on and off gating currents of N588K-hERG1a. *A,* the on gating current was fitted with a double Boltzmann function; $V_{0.5\text{-}1}$ = -9.5mV ± 5.3mV, $V_{0.5\text{-}2}$ = +39.3mV ± 4.5mV, k_1 = 0.08mV ± 0.03mV, k_2 = 0.07mV ± 0.03mV. *B,* the off gating current was fit with a single Boltzmann function, $V_{0.5}$ = 9.8mV ± 11.2mV, k = 12.9mV ± 2.9mV.

4.3.4 Comparison of WT, R528C and N588K -hERG1a gating currents

4.3.4.1 The time constants of decay of gating current

The decay of gating currents at +60mV were fitted with a biexponential function (WT- and R528C-hERG1a) or a monoexponential function (N588K-hERG1a). The time constants of decay can be seen in table 4-1. A significant difference between the time constants was only found between τ_1 of the off gating current, alongside the fact that N588K-hERG1a was found to have only one time constant of decay. This would suggest that the decay of the off gating current of WT-hERG1a has an initial fast component which is lacking in the two mutants.

	ON		**OFF**	
	τ_1	τ_2	τ_1	τ_2
WT	2.1ms ± 0.6ms	4.4ms ± 0.4ms	0.6ms ± 0.2ms	4.4ms ± 3.9ms
R528C	3.3ms ± 1.5ms	9.1ms ± 4.5ms	2.3ms ± 0.9ms	5.9ms ± 2.2ms
N588K	3.2ms ± 1.3ms	-	2.3ms ± 0.5ms	-
P value	P>0.05 (No significant difference between τ_1 of on gating currents, one-way ANOVA)	P>0.05 (No significant difference between τ_2 of WT and R528C on gating currents, unpaired t-test)	P<0.001 (A significant difference between τ_1 of off gating currents, one-way ANOVA)	P>0.05 (No significant difference between τ_2 of WT and R528C off gating currents, one-way ANOVA)

Table 4-1. The time constants calculated from fitting a bi- or mono-exponential function to the gating current at +60mV. One-way ANOVA found a significant difference only between the τ_1 of the off gating current, whilst all other comparisons were found to not to be statistically significant.

Though not statistically different, the τ_1 of WT-hERG1a on gating current (2.1ms ± 0.6ms) is also smaller than that of the two mutants, indicating that this fast component is also present in the decay of the on gating current.

4.3.4.2 Gating current amplitude

The mean amplitude of the on and off gating current from each hERG1a variant was plotted against membrane voltage. All three variants showed a strong voltage dependence with gating current amplitude increasing with membrane depolarisation, with the increase in amplitude becoming observable from -20mV to -10mV, see figure 4-10.

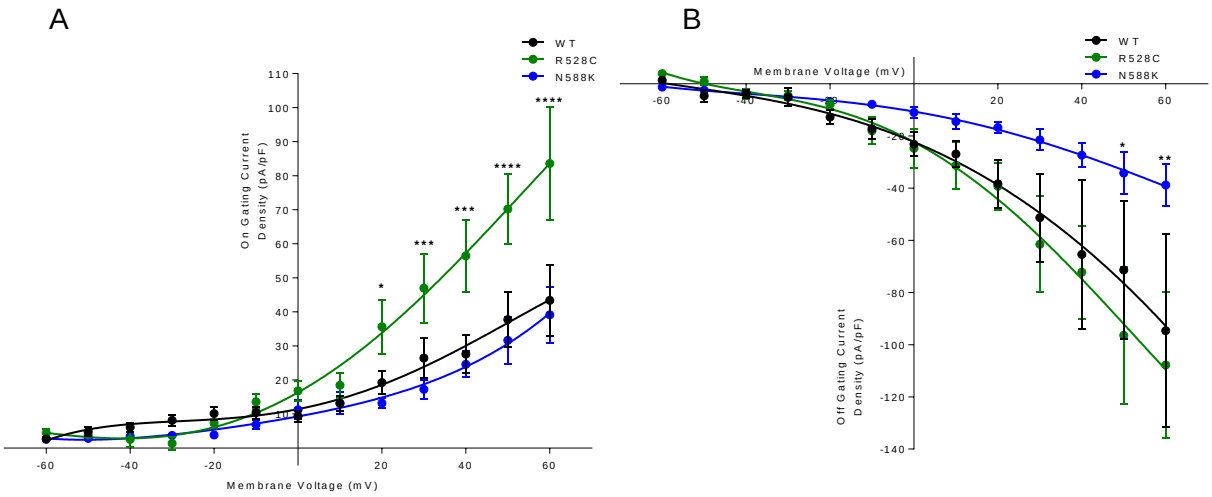

Figure 4-10. The gating current amplitude of WT-, R528C- and N588K-hERG1a normalised with respect to membrane capacitance. A, the on gating current amplitude. Two-way ANOVA with Bonferroni multiple comparison tests found there to be a significant difference between the current amplitude of R528C vs WT and N588K, but no significant difference between WT and N588K. *B,* the off gating current amplitude. Two-way ANOVA with Bonferroni multiple comparison tests found there to be a significant difference between R528C and N588K at +50mV and +60mV and between WT and N588K at +60mV. (Asterisks indicate a significant difference of current amplitude at that membrane potential, lines fitted to the I-V relations are for display purposes only).

R528C-hERG1a displayed the greatest increase in gating current amplitude, with there being a significant effect of the mutation on the gating current amplitude relative to WT-hERG1a channels (two-way ANOVA with Bonferroni multiple comparison tests, $p<0.001$). From +30mV to +60mV a significant difference was found between R528C-hERG1a gating current amplitude and the other two variants, but not between WT-hERG1a and N588K-hERG1a current amplitudes.

When analysing the off gating current amplitude a significant difference was found between R528C-hERG1a and N588K-hERG1a at +50mV and +60mV, and between WT-hERG1a and N588K-hERG1a at +60mV, but no significant difference was found between WT-hERG1a and R528C-hERG1a at any membrane potential.

R528C-hERG1a gating currents, when normalised with respect to membrane capacitance, were greater in amplitude than WT-hERG1a gating currents. This infers that the number of expressed functional R528C-hERG1a channels was no less than the number of WT-hERG1a channels. Therefore the theory that the smaller amplitude macroscopic current density of R528C-hERG1a relative to WT-hERG1a was due to a synthesis error can be discounted. This observation is more likely due to the accelerated inactivation rate of R528C-I_{hERG}. The R528C-hERG1a channel transitions more readily into the non-conducting inactivated state, and therefore it would appear to conduct less current for a given membrane potential compared with WT-hERG1a.

4.3.5 Asymmetry of gating currents

4.3.5.1 Categorisation of asymmetry

From visual observation of gating currents it became apparent that the hERG variants showed both asymmetric and symmetric gating currents, with WT-hERG1a gating currents having a tendency towards asymmetric and the mutants tending towards symmetrical gating currents, see figure 4-11. This asymmetry of hERG gating currents is a known phenomenon that has previously been observed both in oocytes and mammalian cells (Piper et al., 2003a; Wang et al., 2013; Goodchild et al., 2015).

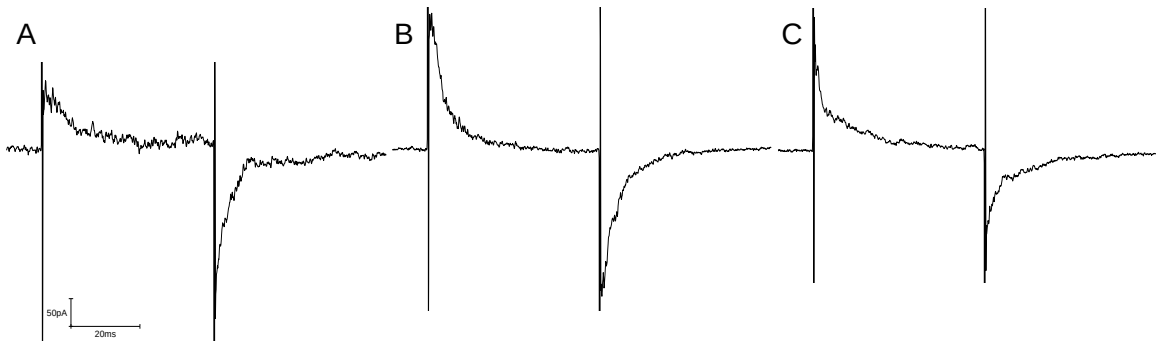

Figure 4-11. Asymmetric and symmetric gating currents. All three hERG variants exhibited asymmetric gating currents. *(A)* WT-hERG1a asymmetric gating currents where the on gating transient current was of a smaller amplitude than the off, and symmetric gating currents of *(B)* R528C-hERG1a and *(C)* N588K-hERG1a where the on and off gating current transients were approximately the same amplitude.

To quantify this characteristic, the on gating current of each cell was divided by the off gating current to produce a ratio. A smaller ratio would indicate a greater degree of asymmetry with the on gating current being smaller than that of the off, and a ratio of 1 would indicate complete symmetry. Ratios of ≤0.6, ≤0.7 and ≤0.8 were tested as threshold for defining asymmetry, with a gating current being classed as asymmetric if the on/off current ratio was less than or equal to the threshold at +60mV. The resulting proportions of asymmetric gating currents can be seen in table 4-2.

	Proportion of asymmetric gating currents		
Threshold	WT	R528C	N588K
0.6	50%	22%	21%
0.7	71%	22%	21%
0.8	71%	56%	43%

Table 4-2. The proportion of gating currents classed as asymmetric with a varied threshold ratio

Relative to a 0.7 threshold, with a threshold of 0.6 the proportion of R528C and N588K asymmetric gating currents did not change, but the proportion of WT decreased. The opposite was true with a threshold of 0.8, as the proportion of WT asymmetric current remained unchanged but the proportion of R528C and N588K asymmetric gating currents increased.

Therefore a ratio of ≤0.7 at +60mV was used as the threshold to define gating current asymmetry, as it was the threshold which maximised the difference between the proportion of asymmetric gating currents of WT, R528C and N588K.

4.3.5.2 Asymmetry of WT-hERG1a gating currents

The asymmetry of the WT-hERG1a sample was analysed and revealed that the development of WT-hERG1a gating asymmetry was voltage dependent from the potential at which gating currents could be resolved (0mV), see figure 4-12.

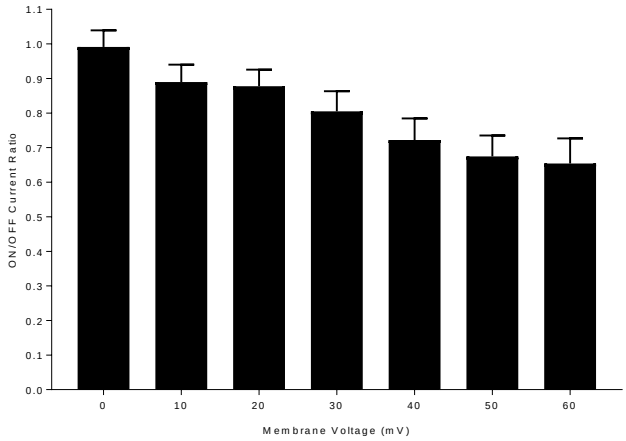

Figure 4-12. Development of the asymmetry of WT-hERG1a gating current. The development of the asymmetric ratio starts with the onset of gating current at approximately 0mV. One-way ANOVA found there to be a significant effect of membrane depolarisation on the ratios across the membrane potential range ($p<0.01$).

Figure 4-12 shows a clear decrease in the ratio as potentials become more depolarised, indicating that amplitude of the off gating current increased more than the on for a given membrane depolarisation, resulting in a greater degree of asymmetry. This effect of membrane depolarisation on the ratio was found to be significant (one-way ANOVA, $p<0.01$).

As stated above, examples of both asymmetric and symmetric WT-hERG1a gating currents were found, see figure 4-13. Using the ≤0.7 ratio threshold, 71% of the WT sample was categorised as asymmetric with the on gating current being of smaller amplitude than the off gating current.

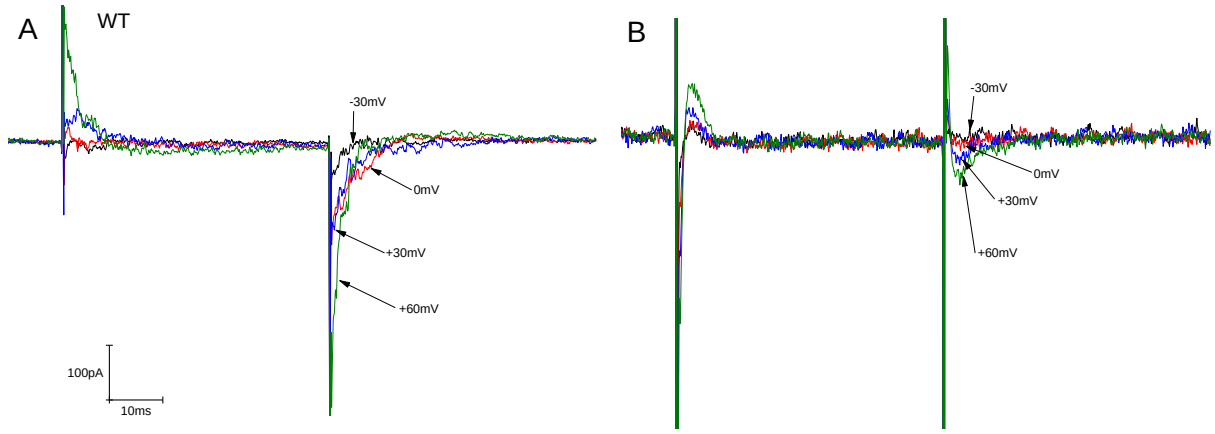

Figure 4-13. WT-hERG1a gating currents exhibited two populations; asymmetric and symmetric. *A,* representative trace of a WT-hERG1a asymmetric gating current which accounted for 71% of the sample population (10/14 cells) and *B,* representative trace from a symmetric gating current (29% of the sample population (4/14 cells.)

The mean ratio of the asymmetric and symmetric gating current sample was compared at the potentials where gating currents could be resolved (see figure 4-14). In both populations the ratio was found to decrease as potentials became more depolarised, but the mean ratio of the asymmetric population across the potential range was significantly less than that of the symmetric population (two-way ANOVA, $p<0.05$).

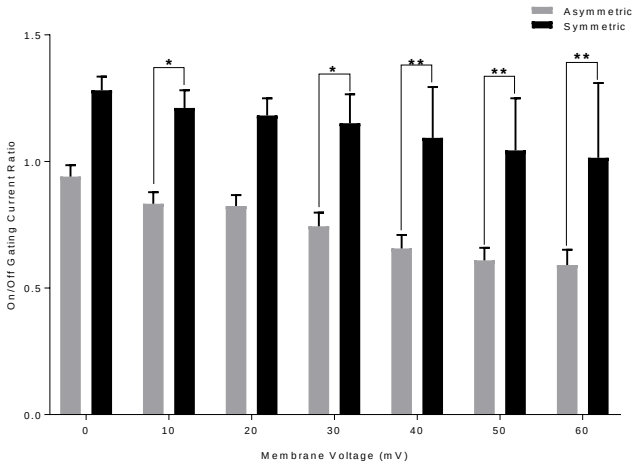

Figure 4-14. WT-hERG1a gating currents showed two populations; asymmetric and symmetric. At 0mV to +60mV (potentials where gating currents could be recorded) two-way ANOVA with Bonferroni multiple comparisons found a significant difference between asymmetric and symmetric ratios, indication of there being two gating current populations present, and a significant effect of membrane voltage on the gating current ratio. Asterisks indicate a significant difference at that membrane potential.

4.3.5.3 R528C-hERG1a gating current symmetry

When the R528C-hERG1a gating sample was analysed as a whole, the development of gating current asymmetry did not exhibit a clear voltage-dependence as found in WT-hERG1a, see figure 4-15. The mean ratio of the sample varied across the membrane potential range, but there was no indication that this variation was affected by membrane depolarisation.

Using the ≤0.7 ratio threshold, 22% (2/9) R528C-hERG1a gating currents were classified as asymmetric, see figure 4-16, in comparison to 71% of WT-hERG1a gating currents. This implies that while both hERG variants show both asymmetric and symmetric gating currents,

WT-hERG1a tends to exhibit asymmetric currents while R528C-hERG1a tends towards symmetric gating currents.

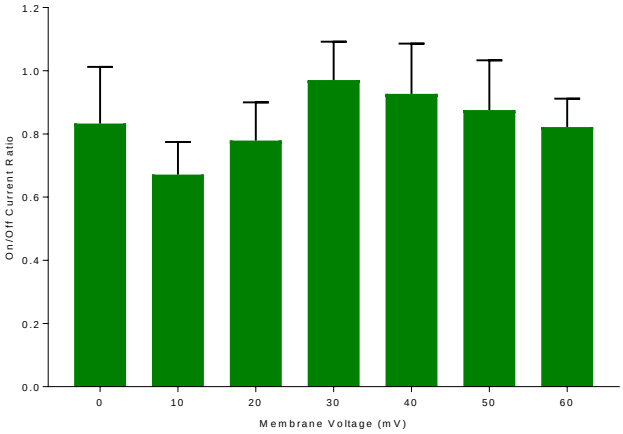

Figure 4-15. R528C-hERG1a channel gating current showed no voltage-dependent development of asymmetry. The on/off gating current ratio was plotted from 0mV, where gating currents could be resolved. One-way ANOVA found no significant difference between the ratios across the range of membrane potentials used (p>0.05).

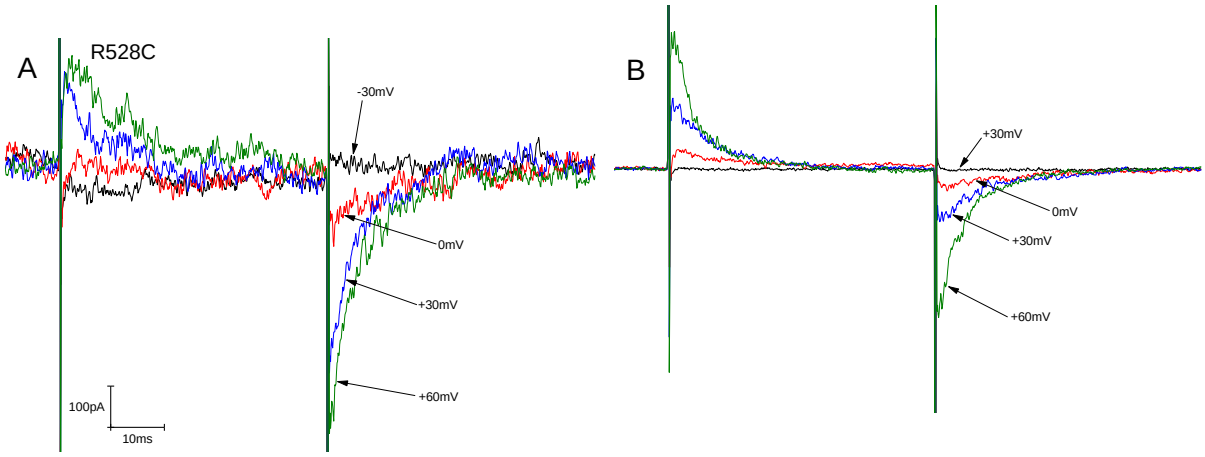

Figure 4-16. R528C-hERG1a asymmetric and symmetric gating currents. *A,* representative trace of an R528C asymmetric gating current which made up 22% of the sample population (2/9 cells) and *B,* representative trace from an R528C symmetric gating current (78% of the sample population (7/9 cells)).

The sample of R528C-hERG1a asymmetric gating currents was compared with the symmetric sample using the mean on/off gating current ratio, see figure 4-17. As in figure 4-15, no voltage-dependent development of asymmetry was found, and there was no significant difference between the mean ratio at any membrane potential (two-way ANOVA, p>0.05). This is a strong indication that R528C-hERG1a gating currents show no real asymmetry in contrast to WT-hERG1a gating currents.

R528C-I_{hERG} was shown to have an accelerated rate of activation compared with WT-hERG1a (see chapter 3), which owing to the position of the R528C mutation, must be related to the loss of a positively charged S4 residue and the resulting change in S4 movement. Likewise, the increased on gating current amplitude relative to the off may be partly due to an altered S4 movement as the channel shifts into the open conformation.

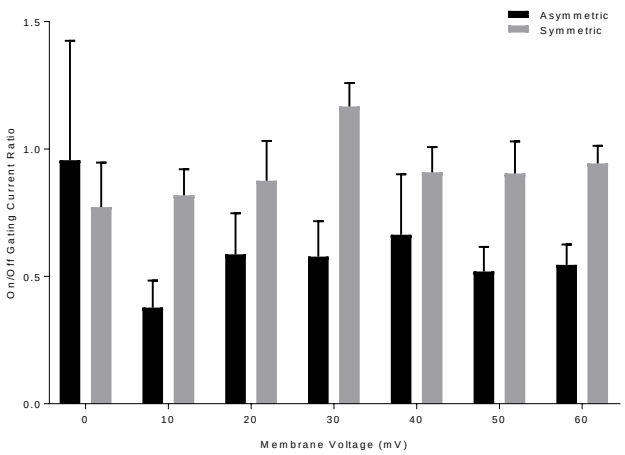

Figure 4-17. R528C-hERG1a gating currents did not show asymmetric and symmetric populations. Gating currents classed as asymmetric and symmetric were expressed as the on/off gating ratio at 0 to +60mV (potentials where gating currents could be recorded). There was no difference between the ratios and no significant effect of membrane potential on the on/off gating ratio (two-way ANOVA with Bonferroni multiple comparisons).

4.3.5.4 N588K-hERG1a gating current symmetry

Though examples of asymmetric and asymmetric N588K-hERG1a gating currents were found, there was no evidence of asymmetry when the ratio of the sample was analysed as a whole, see figure 4-18. Though the ratio decreased at 50mV and 60mV relative to more hyperpolarised potentials, the mean value remained approximately 1 indicating current symmetry.

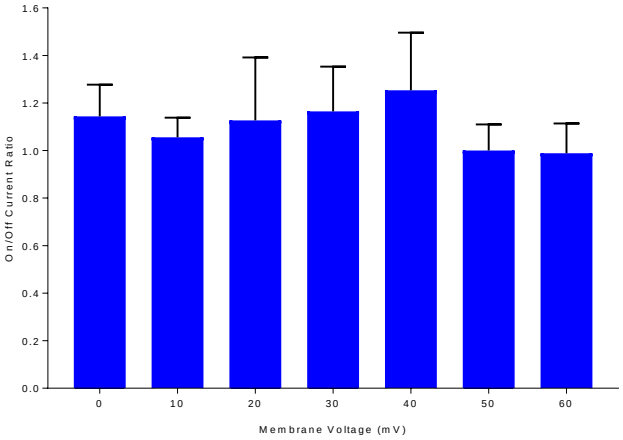

Figure 4-18. When analysed as a whole, the N588K-hERG1a gating current sample showed no development of asymmetry. One-way ANOVA with Bonferroni multiple comparisons found no difference between the ratios of N588K across the range of membrane potentials used (p=0.9370).

As with WT-hERG1a and R528C-hERG1a, N588K-hERG1a gating currents were categorised according to the ≤0.7 ratio threshold. 21% (3/14) of the sample was classed as asymmetric, similar to the 22% of R528C-hERG1a gating currents but far less than that of WT-hERG1a (71%). Examples of N588K-hERG1a asymmetric and symmetric gating currents can be seen in figure 4-19.

Comparison of the asymmetric and symmetric gating currents of N588K-hERG1a confirmed that neither group exhibited voltage-dependent development of asymmetry, see figure 4-20. The ratio showed no trend across the membrane potentials and the ratio of the ‘asymmetric’ group was greater than that of the ‘symmetric’ group at 0mV, +20mV and +40mV. One-way ANOVA found there to be no difference between the ratios of the asymmetric and symmetric

populations and no significant effect of membrane potential on the gating current ratio. Therefore, in spite of 3 asymmetric examples, N588K-hERG1a can be considered to only exhibit symmetric gating currents.

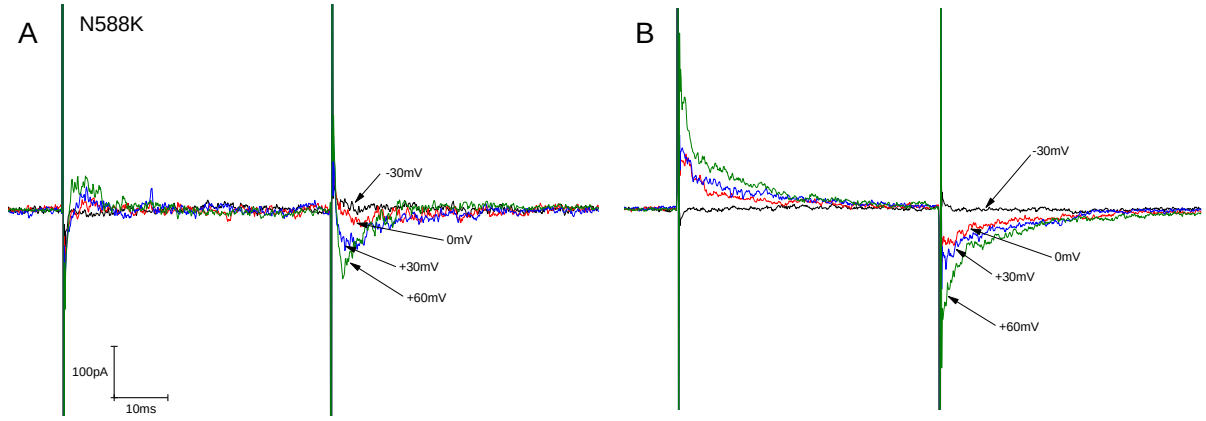

Figure 4-19. N588K-hERG1a asymmetric and symmetric gating currents. *A,* representative trace of an asymmetric gating current which made up 21% of the sample population (3/14 cells) and *B,* representative trace from a symmetric gating current (79% of the sample population (11/14 cells)).

The symmetry of N588K-hERG1a gating currents may be related to the channel's lack of inactivation, however due to the time scale of the gating currents this is unlikely. Another theory would be that the N588K-hERG1a mutation in the S5-P linker has affected the conformation of the channel or the S4 voltage sensor, therefore affecting the movement of the S4 upon the opening of the channel.

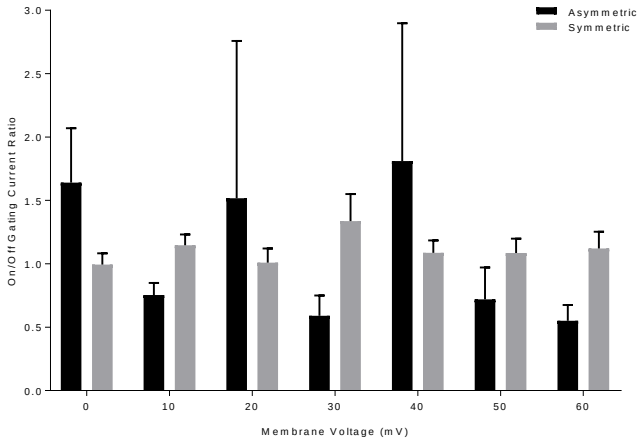

Figure 4-20. N588K-hERG1a gating currents showed no asymmetry. Gating currents classed as asymmetric and symmetric were expressed as the on/off gating ratio at 0 to +60mV (potentials where gating currents could be recorded). There was no difference between the ratios and no significant effect of membrane potential on the on/off gating ratio (two-way ANOVA with Bonferroni multiple comparisons).

4.3.5.5 The slow activation of WT-hERG1a and gating current asymmetry

To investigate whether the asymmetry of WT gating current was linked to slow activation or fast inactivation of the channel a voltage protocol with an increasing duration of the command pulse was used. With an increasing pulse duration more channels would have time to transition into the open and then inactivated state. This would result in a larger off gating current, as charged residues from a greater number of channels which had moved in order to traverse these two states would then move back at the same time upon repolarisation. With shorter pulse durations the opposite would be true, resulting in symmetric gating currents.

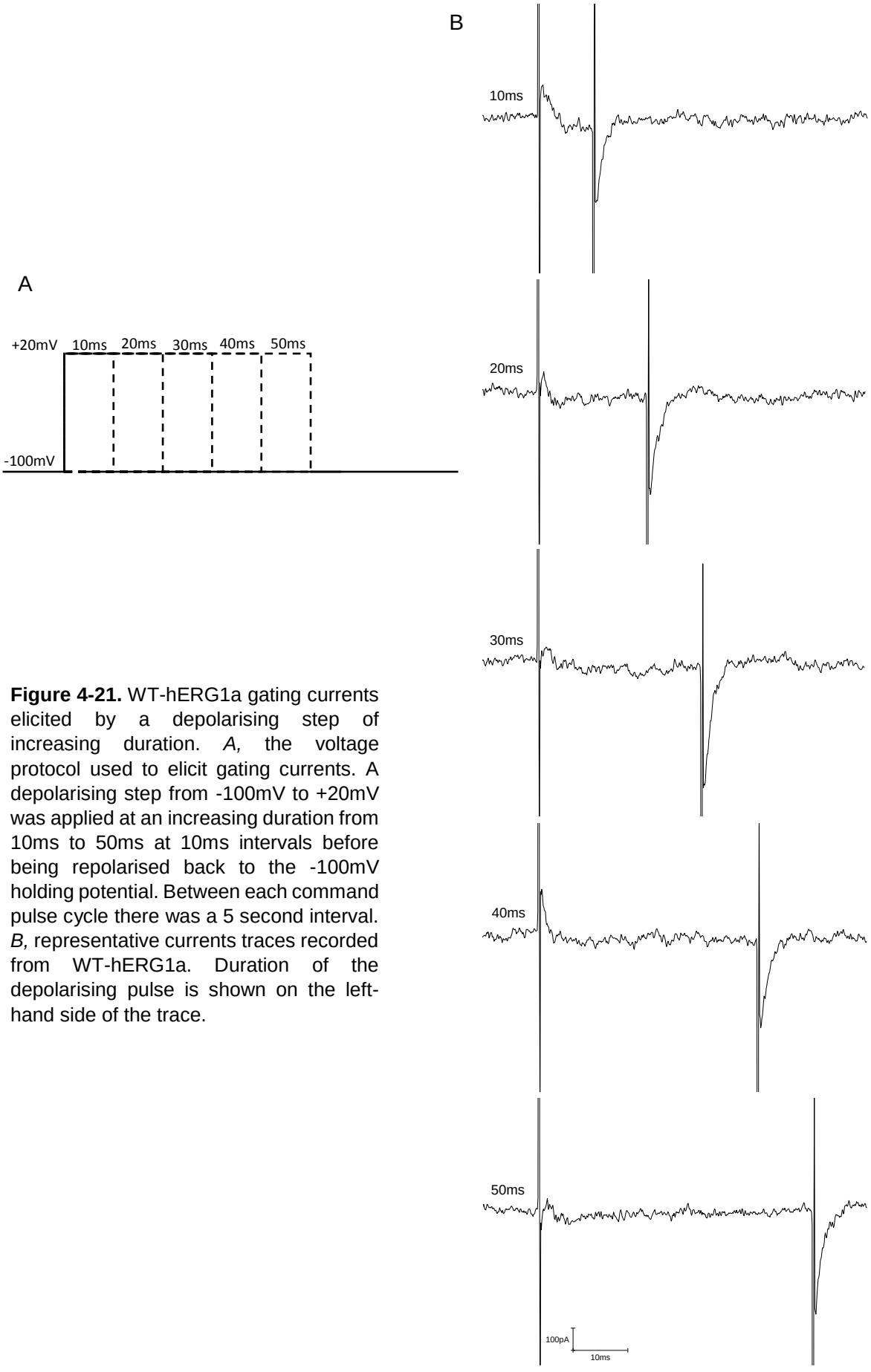

Figure 4-21. WT-hERG1a gating currents elicited by a depolarising step of increasing duration. *A,* the voltage protocol used to elicit gating currents. A depolarising step from -100mV to +20mV was applied at an increasing duration from 10ms to 50ms at 10ms intervals before being repolarised back to the -100mV holding potential. Between each command pulse cycle there was a 5 second interval. *B,* representative currents traces recorded from WT-hERG1a. Duration of the depolarising pulse is shown on the left-hand side of the trace.

Figure 4-21, *A* shows the voltage protocol used to elicit gating currents. Cells were depolarised to +20mV from a holding potential of -100mV in order to fully activate the channels. This +20mV depolarising pulse was applied at a duration of 10ms before cells were repolarised to the holding potential. After an interval of 5 seconds the protocol was repeated with the +20mV pulse being applied for 20ms. The overall cycle was repeated to enable the depolarising pulse to be of 10, 20, 30, 40 and 50ms duration.

Figure 4-21, *B* shows representative gating currents recorded from the WT-hERG1a channel. As with the previous WT-hERG1a gating currents, the off appears to be of greater current amplitude than the on, but from the traces there appears to be no obvious increase in the amplitude of the off gating current as the pulse duration increases.

Using the gating currents elicited from this protocol, the on/off ratio from both current amplitude and charge magnitude was plotted against the duration of the depolarising pulse (see figure 4-22).

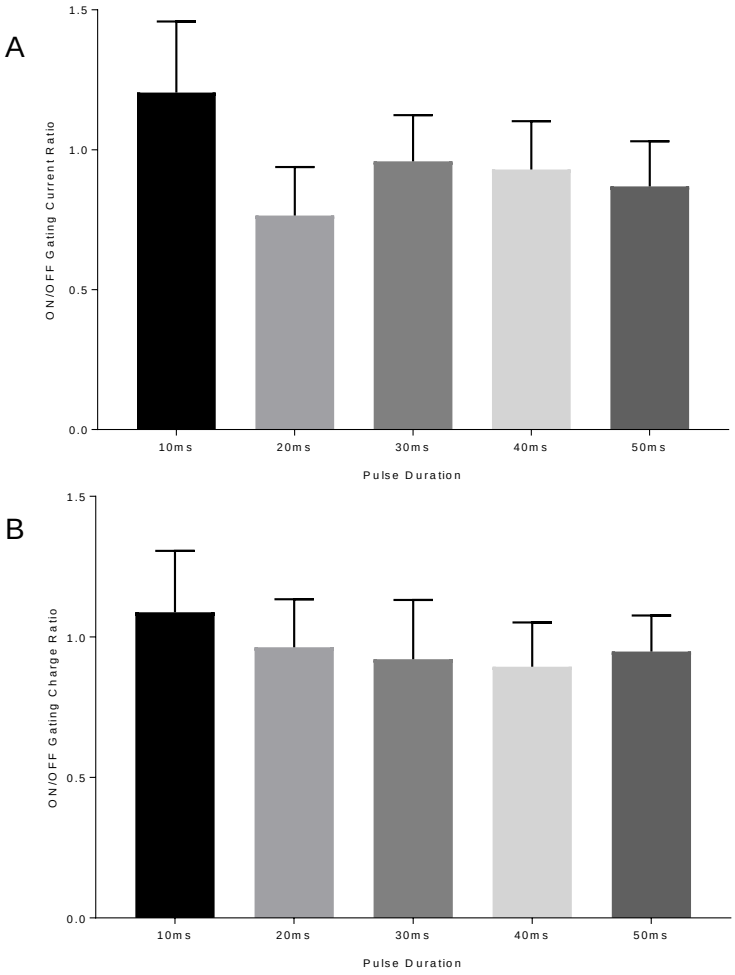

Figure 4-22. The asymmetry of gating currents elicited by a depolarising pulse of increasing duration. *A,* the amplitude of the on and off gating currents were expressed as a ratio for each duration of the depolarising pulse. One-way ANOVA with Bonferroni multiple comparison tests found no significant difference between the ratio at any pulse duration (p=0.5669, n=9). *B,* when expressed as a ratio of on to off gating charge, there was no significant effect of increasing the depolarising pulse duration (one-way ANOVA with Bonferroni multiple comparison tests (p=0.9514, n=9)).

The 10ms pulse exhibited the greatest ratio (1.2 ± 0.3 for current, 1.1 ± 0.2 for charge) relative to the other pulse durations, see table 4-3. Increasing the depolarising pulse duration above 10ms decreased the ratio of the current, indicating that that a longer pulse had caused more

channels to open resulting in gating current asymmetry. The charge ratio also decreased with an increased pulse duration, although not to the same extent. However, one-way ANOVA found there to be statistically no difference between either the current or charge ratios.

	10ms	20ms	30ms	40ms	50ms
Current Ratio	1.21 ± 0.30	0.77 ± 0.17	0.96 ± 0.17	0.93 ± 0.17	0.87 ± 0.16
Charge Ratio	1.09 ± 0.22	0.96 ± 0.17	0.92 ± 0.21	0.89 ± 0.16	0.95 ± 0.13

Table 4-3. The on/off ratio from the WT-hERG1a gating currents elicited by an increasing depolarising pulse duration, using both gating current amplitude and gating charge. One-way ANOVA with Bonferroni multiple comparisons found there to be no significant difference between the ratios at any pulse duration.

This suggests that more channels are able to transition into the activated state during a longer depolarising pulse, which is reflected in a larger off gating amplitude and a decreased gating current ratio. Though the decrease of gating current and charge ratio is not significant, this likely reflects the small sample size analysed rather than a longer pulse duration having no effect on the number of channels opening.

4.4 Discussion

4.4.1 The R528C mutation has no effect on the magnitude of gating currents

In WT-hERG1a channels, the positively charged R528 residue is theorised to contribute to the transfer of gating charge as the S4 voltage sensor moves across the membrane field (Zhang et al., 2005). The movement of the R528 residue has been investigated using accessibility studies and VCF (Smith and Yellen, 2002; Zhang et al., 2004; Cheng and Claydon, 2012). In accessibility studies residues were mutated to allow binding of compounds such as MTSET or pCMBS (p-Chloromercuribenzenesulfonate), which were applied either intra- or extracellularly during voltage protocols designed to activate and inactivate the channel. If MTSET or pCMBS accessibility exhibited state dependence, this would provide evidence that the modified residue had changed its position and moved out of the lipid bilayer (Cheng and Claydon, 2012). In fluorimetry, fluorescence is detected when two fluorophores move within close proximity of each other, and so can be used to track the movement of the S4 domain upon depolarisation.

Though indirect measures, both methods concluded that the S4 domain moves across the membrane field upon activation. MTSET accessibility demonstrated that R528 did not translocate across the membrane, but this was attributed to MTSET being too large to access the residue and when the smaller pCMBS molecule was used it confirmed that R528 moved up through the membrane upon depolarisation (Zhang et al., 2004; Wang et al., 2013; Elliott et al., 2009; Cheng and Claydon, 2012).

The limiting slope method has been employed to estimate the number of gating charges which move upon channel activation. It was found that the R528C mutation reduced the estimated number of gating charges to 3.77 ± 0.35 compared with 6.35 ± 0.69 in WT channels (Zhang et al., 2004). Based on these conclusions and those from VCF and accessibility studies, it would be expected that the R528C mutation would reduce the gating current amplitude, as less charged particles would move through the membrane field.

However, in this study the R528C mutation did not reduce the magnitude of gating charge, the amplitude of gating current or the slope of the activation curve of ionic current. The gating charges measured from all three hERG variants were not statistically different from each other, despite there being one less charged residue present in the S4 domain in R528C. This would suggest that R528 does not move out of the membrane field upon depolarisation despite its relatively superficial position in the S4 domain, indicating that upwards S4 movement may not be as extensive as previous studies have concluded (Zhang et al., 2005; Elliott et al., 2009).

When the gating current amplitude was analysed the R528C-hERG1a mutant had a greater on gating current amplitude that both that of N588K and WT-hERG1a. This could be attributed to a faster rate of activation of R528C-hERG1a than when compared with WT-hERG1a (see chapter 3) and N588K-hERG1a, which would mean more channels are activating at the same time upon depolarisation resulting in a large amplitude gating current. Mutations of R528 are known to change expression levels of the channel; the R528A mutation reduced the level of expression to the point where gating current recordings proved impossible (Piper et al., 2005b). Therefore there is potential that the R528C mutation increased hERG1a expression levels which would also result in a greater amplitude of gating currents compared with WT-hERG1a and N588K-hERG1a.

The disparity between the effect of the neutralisation of R528 found here compared with other studies could be related to the expression systems used in each study. Studies which have concluded that R528 translocates across the lipid bilayer (as measured by MTSET and pCMBS accessibility) and contributes to gating charge (seen by a decrease in the gating charge when R528 charge was neutralised) used *Xenopus* oocytes to express the hERG channel, (Subbiah et al., 2004; Zhang et al., 2004, 2005; Elliott et al., 2009) in contrast to this study which used mammalian tsA201 cells. It could be suggested that within oocyte membranes the hERG channel conformation varies from its native state due to variations in the lipid bilayer composition (Hill et al., 2005; Van Meer et al., 2008) or due to enzyme variation in the protein synthesis pathway (Vandenberg et al., 2012). Any differences in conformation of the channel protein could lead to the S4 region moving further out of the membrane, resulting in R528 appearing to contribute more to the gating charge than it does in its native state.

4.4.2 The asymmetry of gating currents

Previous studies have recorded gating currents from the hERG1a channel, albeit using oocytes to express the channel (Piper et al., 2003a; Zhang et al., 2004; Ferrer et al., 2006; Goodchild and Fedida, 2014; Goodchild et al., 2015; Dou et al., 2017) whilst a few other publications have succeeded in using tsA201 cells (Fedida et al., 2012; Wang et al., 2013). Gating currents are harder to resolve in mammalian cells due the expression efficiency being lower than when compared with oocytes resulting in a lower amplitude of current transient, combined with the cut-open oocyte technique having a higher temporal resolution, facilitating the recording of fast gating currents (Sigel, 1990; Tammaro et al., 2008; Stefani and Bezanilla, 1998).

The apparent asymmetry of WT-hERG1a gating currents could be linked to the reduced expression efficiency and lower temporal resolution of tsA201 cells. It was suggested that the slow component of the on gating current was lost in the recordings presented here due to longer voltage clamp settling times and greater background noise compared with the cut-open oocyte voltage-clamp technique (Stefani and Bezanilla, 1998). Theoretically, the loss of this slower component would give the gating currents their asymmetric appearance as only the fast on gating current could be resolved (Wang et al., 2013; Goodchild and Fedida, 2014). However, the poorer resolution would also apply when recording the off gating current leading to symmetric gating currents, therefore poor resolution does not explain the observed asymmetry.

From the time constants fitted to WT-hERG1a gating currents it was clear that there were two components, the slower time constant being 4.4ms ± 0.4ms for the on gating current and 4.4ms ± 3.9ms for the off gating current. These are similar to that of 3.0ms (on) and 6.2ms (off) recorded from tsA201 cells by Wang et al. and 7.6ms (off) measured by Goodchild et al. when recording from oocytes. From these values it is clear that the asymmetry of WT-hERG1a gating currents is not a product of low-resolution recordings, as the slow component of the gating currents was successfully recorded. The theory behind the asymmetry will be fully discussed in chapter 6 (general discussion).

4.4.3 The monoexponential decay of the N588K-hERG1a gating current

The gating currents recorded from N588K-hERG1a channels were found to display a monoexponential decay, in contrast to WT-hERG1a and R528C-hERG1a which were found to have a bi-exponential decay. This bi-exponential decay has previously been found and attributed to the movement of two charge components which move at different speeds over different voltage ranges to facilitate the opening of the channel (Wang et al., 2013). The first component moves faster at a more negative range of potentials and is hypothesised to be due

to the movement of S4 to an intermediate state. The second charge component is slower and larger, and moves at potentials closer to those associated with the opening and closing of the ion channel pore (Piper et al., 2003a; Goodchild and Fedida, 2014; Goodchild et al., 2015).

N588K-hERG1a has primarily been investigated for its inactivation-deficient properties, as this leads to SQTS, and the mutation is not known to affect the movement of the S4 voltage sensor (Cordeiro et al., 2005; McPate et al., 2005). However, N588K-hERG1a has also been found to have faster deactivation kinetics than WT-hERG1a (Grunnet et al., 2008). Though this increase in the deactivation rate has not been attributed to any particular charge component, it could be linked to monoexponential decay of the gating current. If the rate of movement of either charge component was increased, resulting in a faster deactivation rate, in a lower resolution system such as tsA201 cells the difference between the two components may no longer be resolved. Consequently, only a monoexponential decay would be seen in the N588K-hERG1a gating currents compared with the biexponential decay in WT-hERG1a and R528C-hERG1a gating currents.

4.5 Conclusion

Gating currents arise from the movement of charged particles across the membrane field in response to depolarisation and repolarisation, and represent the change in ion channel conformation between the closed and open states. The gating currents of WT-hERG1a and the R528C-hERG1a and N588K-hERG1a mutants were recorded in spite of the difficulty of resolving small amplitude currents in mammalian cells. Regardless of the mutants having different ionic current properties compared with the WT-hERG1a channel, no significant differences were found between their gating currents except the asymmetry of gating currents in WT-hERG1a compared with the symmetry of currents recorded from R528C-hERG1a and N588K-hERG1a. This phenonmenon is believed to be related in part to the differing kinetic properties of the mutants, and will be discussed in chapter 6 (the general discussion).

5. AFM imaging of the WT-hERG1a ion channel

5.1 Introduction

5.1.1 Atomic Force Microscopy

Atomic Force Microscopy (AFM) is a form of scanning probe microscopy which measures the topographical shape of samples at an atomic level. Since its conception in 1986 many AFM imaging modes have been developed, several of which have been utilised to characterise biological samples ranging from whole animal cells to membrane-bound proteins, DNA, RNA and ion channels (Binnig et al., 1986; Dufrêne et al., 2017; Krieg et al., 2019).

At its core, AFM relies on the interaction between the AFM probe and the sample surface; the resulting forces between the two are detected by the deflection of the cantilever upon which the probe is mounted. The AFM probe is sharp, the tip being generally less than 10nm in diameter, while the cantilever is approximately 100-500µm long, usually fabricated from silicon and coated with a reflective material such as gold (Vahabi et al., 2013; Dufrêne et al., 2017). The cantilever is very flexible, allowing it to bend according to the force applied to the probe tip. Cantilevers of different spring constants (*k*, as measured by Hooke's Law) have different degrees of flexibility, with softer cantilevers with a smaller spring constant being essential for the imaging of soft biological samples (Zhong and Yan, 2016).

The deflection of the cantilever is measured using a laser directed at the reflective surface on the top of the cantilever. The laser beam is reflected onto a photodetector which detects the position of the cantilever. This information is then processed, building up a topographical map of the sample surface (from the data collected about the height of a sample) alongside information about the properties of the sample such as adhesion, friction and elasticity (Vahabi et al., 2013; Zhong and Yan, 2016).

There are three primary modes of AFM imaging; contact mode, non-contact mode and tapping/intermittent contact mode. As indicated by the name, in contact mode the AFM probe remains in contact with the sample for the duration of the scan. To engage the cantilever the microscope first moves it down through the sample clearance distance set by focusing the camera first on the cantilever and then on the top of the sample. Once this distance has been covered the software steps the probe towards the sample until a measure of roughness detected by the probe (known as RMS, or Root Mean Squared) has dropped to a prespecified percent of the original RMS, at which point scanning will commence. Though contact mode can produce high resolution images relatively large frictional forces are involved. When considering a soft cell membrane these high frictional forces increase the likelihood of the sample being damaged (Vahabi et al., 2013; Dufrêne et al., 2017).

In non-contact mode the sample and the AFM probe never touch. Instead the deflection is caused by the electrostatic forces between the probe and the sample, believed to be the attractional long-distance Van der Waals forces. This mode requires more skill to produce high quality images as there is the additional risk that the probe and sample will form a capillary bridge through the water layer on the sample surface. This will result in 'jump-to-contact' of the tip and requires a high frequency feedback system to ensure that the probe remains a suitable distance from the sample surface (Vahabi et al., 2013; Zhong and Yan, 2016).

In tapping mode, the probe is oscillated at its resonant frequency as it tracks across the sample, resulting in the probe being intermittently in contact with the surface. This mode is capable of producing high resolution images (though not as high as contact mode) and the probe can scan at a fast rate whilst causing minimal damage to the sample (Dufrêne et al., 2017).

5.1.2 The use of AFM in molecular and cell biology

AFM in tapping mode has been widely used to image biological samples due to it being able to image in both dry and liquid environments and at temperatures suitable for biological systems. Alongside static images, some biological processes have been recorded such as the extension of cell filopodia and DNA degradation by enzymes using a combination of HS-AFM (high-speed AFM) and time-lapse contact mode (Henderson et al., 1992; Bezanilla et al., 1994b; Casuso et al., 2012).

More recently, frequency-modulation AFM (FM-AFM) has been developed, where the change in the oscillation of the cantilever due to interactions between the probe and the sample is used to build an image of the sample surface (Uchihashi et al., 2004). This mode exerts less force upon the sample surface, resulting in less distortion of biological samples. FM-AFM has obtained images of monoclonal IgG antibodies when mounted on a mica substrate and succeeded in imaging closed-circular plasmid DNA to the level where individual phosphate groups of the DNA backbone could be detected (Ido et al., 2013, 2014).

Ion channels have also been imaged using AFM. Such examples include TRPP2 (TRP channel polycystin-2), iGluRs (ionic glutamate receptors, both AMPA and NMDA), prokaryotic homologues of a cys-loop receptor and CNG channels, which have all been imaged primarily through the use of HS-AFM and FM-AFM (Shinozaki et al., 2014; Rangl et al., 2016; Ruan et al., 2017, 2018; Lal et al., 2018; Marchesi et al., 2018). The imaging of the prokaryotic homologue of a CNG channel (SthK) was combined with the washing on of cAMP and cGMP to open and close the channel, respectively. This allowed the movement of the subunits within the tetramer to be tracked during channel activation; as a result a gating mechanism of the channel could be proposed (see figure 5-1) (Marchesi et al., 2018).

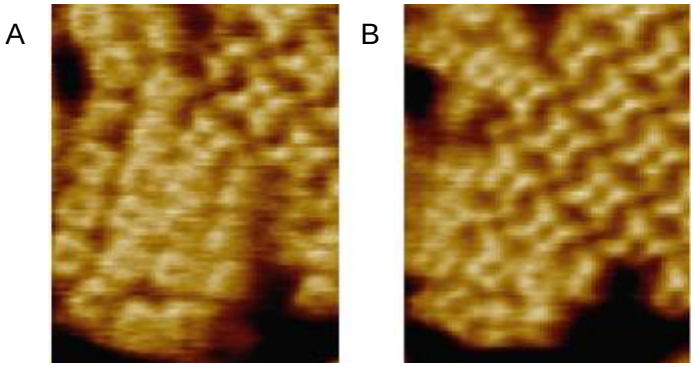

Figure 5-1. The open and closed states of the SthK CNG channel imaged using real-time HS-AFM. *A,* Addition of 7mM cGMP caused the subunits to adopt the closed conformation. *B,* addition of 0.1mM cAMP caused the tetramers to twist, with the channels adopting the open conformation. Adapted from Marchesi et al., 2018

The caveat to these images is that they were obtained by first purifying and then mounting the ion channels onto a stable, flat surface. This could be achieved by a variety of approaches such as inserting a small number of ion channels into a reconstituted membrane and then mounting this construct onto a mica surface. An alternative approach would be inserting a large number of channels into a reconstituted membrane to the point where the lipid bilayer becomes almost rigid. The images in figure 5-1 were obtained by first purifying and crystallising the ion channel proteins before mounting the sample onto a mica surface.

A stable surface is necessary for AFM imaging as the sample is required to be as immobile as possible to get an accurate height measurement of the sample. This is especially true when attempting to image something on the scale of an ion channel (Vahabi et al., 2013; Dufrêne et al., 2017). The images obtained in the previous studies, though there can be no doubt as to their significance, do not represent ion channels expressed in a cell membrane and so may not represent channels in their native conformation.

5.1.3 AFM and the hERG1a ion channel

Despite the physiological significance of the hERG ion channel very few studies have attempted to image it using AFM (Vandenberg et al., 2012). In 2008, AFM was utilised to identify which domain of hERG provided the binding site for the scorpion toxin Ergtoxin 1 (ErgTx1). An anti-hERG antibody (directed at residues 430-445 of the channel) was covalently linked to the probe, allowing the probe to form a bond with the channel. The extent to which the cantilever bent upon being moved away (which varied according to the strength of the bond) was used to identify the location and density of the channels. Application of ErgTx1 reduced the number of recognition events, providing evidence that the toxin bound to the S1-S4 domain of the channel and therefore could not be considered a conventional pore blocker (Chtcheglova et al., 2008).

Furthermore, AFM has provided evidence that the sigma-1 receptor binds to the hERG ion channel, with one sigma receptor binding to one hERG subunit, and possibly modifies the

assembly and trafficking of the channel (Su et al., 2016). The hERG channel was imaged after being isolated and purified from different points in the synthesis pathway (therefore individual hERG subunits were resolved) and then adsorbed onto a mica surface (see figure 5-2). Although the imaging of the hERG channel at a high enough resolution to be able to distinguish between its monomer, dimer or tetramer subunit forms signifies a considerable achievement, the images still fail to represent the channel in its native state in a cell membrane. (Balasuriya et al., 2014).

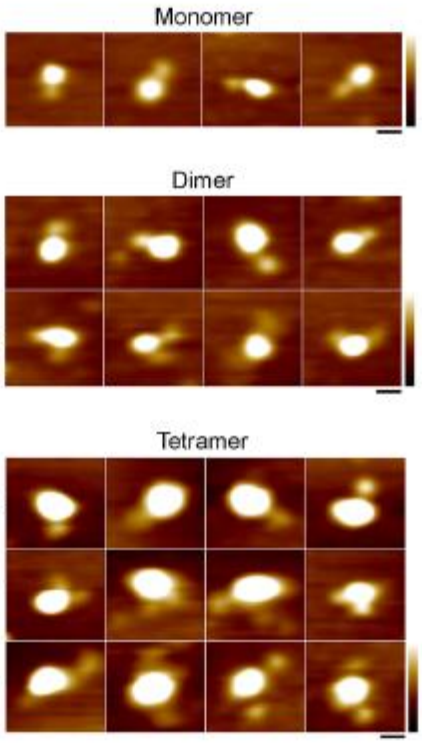

Figure 5-2. AFM images of the hERG1a ion channel bound to the sigma-1 receptor. hERG channels were imaged with either one or two sigma receptors bound, however only one sigma receptor bound to one hERG subunit. Images were obtained using tapping mode in air. Before imaging the proteins were purified and then adsorbed onto a mica surface. Adapted from Balasuriya et al., 2014.

My project aimed to image the hERG1a channel whilst being expressed in a cell membrane which would allow the channel to adopt its native conformation. Assuming this was successful the channel would then be imaged in both closed and open conformations, either being activated through use of a depolarising pulse being applied across the liquid of the sample or using a high concentration of potassium in the liquid. Comparison of the two images would reveal the change in subunit conformation between open and closed states.

More outlandish aims were to use HS-AFM to measure the movement of the S4 region upon channel activation. To allow the possibility of this occurring using conventional AFM, the R528C-hERG1a mutant was produced that would allow the S4 domain to be fixed in its activated upward state through application of extracellular MTSET. MTSET would bind to the cysteine residue on S4, and being membrane impermeable, would prevent S4 from moving back down upon channel deactivation.

5.2 Results

5.2.1 Problems encountered during AFM imaging

Initially the main problem was the lack of a UV light source on the AFM microscope, rendering the approach of transient transfection identification through eGFP expression unusable. A stable cell line of the hERG channel was therefore sourced which enabled any cell to be selected for imaging as all would be expressing the hERG channel. The hERG1a channel was stably expressed in a HEK293 cell line in contrast to the tsA201 cell line used for electrophysiology, but characterisation of the stable cell line ionic current found there to be no difference between the two mechanisms of expression. However, it remained a challenge to distinguish cells upon imaging owing to the contrast and resolution of the camera used to locate the sample.

The time to set up the AFM microscope (directing the laser at the cantilever surface, finding the probe, calibrating the distance between the AFM probe and the sample surface etc.) varied enormously, but was often found to be greater than the lifespan of cells once bathed in PBS. Imaging cells in DMEM was not an option owing to the large molecules found within the supplemented media. Even if the microscope was prepared within the cell life span, the flexible surface of the membrane made achieving a high resolution image problematic and meant even soft cantilevers damaged the cell membrane.

Storage of the cells in PBS caused crystals to precipitate onto the membrane surface even when the sample remained in solution for imaging. Not only did these crystals appear when imaging the cell, they damaged the sharp AFM probe causing imaging artefacts to be detected on the membrane surface, rendering the probes (of which there were a finite number available for use) useless for imaging.

As a result cells were fixed using a 4% solution of paraformaldehyde. This would cross-link proteins within the cell and cell membrane, making the membrane stiffer and theoretically more difficult to damage. After fixation, cells were washed in distilled water in an attempt to remove PBS crystals and any remaining debris from the membrane surface, and thoroughly dried. A dried sample imaged using tapping mode in air, though not ideal, required less variables to be measured and controlled compared with tapping mode in liquid, facilitating the ease of imaging.

5.2.2 Imaging of whole cells

To ensure there was no obvious debris or damage to the cell membrane, an initial 40μm^2 image was taken of a suitable cell, see figure 5-3. The outlines of multiple cells are clearly

visible along with filopodia-like extensions (blue arrows). A 3D render of the same data provided insight into the height ranges across the sample which were an additional impediment to obtaining high resolution images, given that the pre-set oscillation frequency of the cantilever only allowed the probe tip to extend so far. If a cell-surface structure raised the height beyond that which the probe could extend there was a risk of the image becoming distorted and the AFM probe tip becoming damaged.

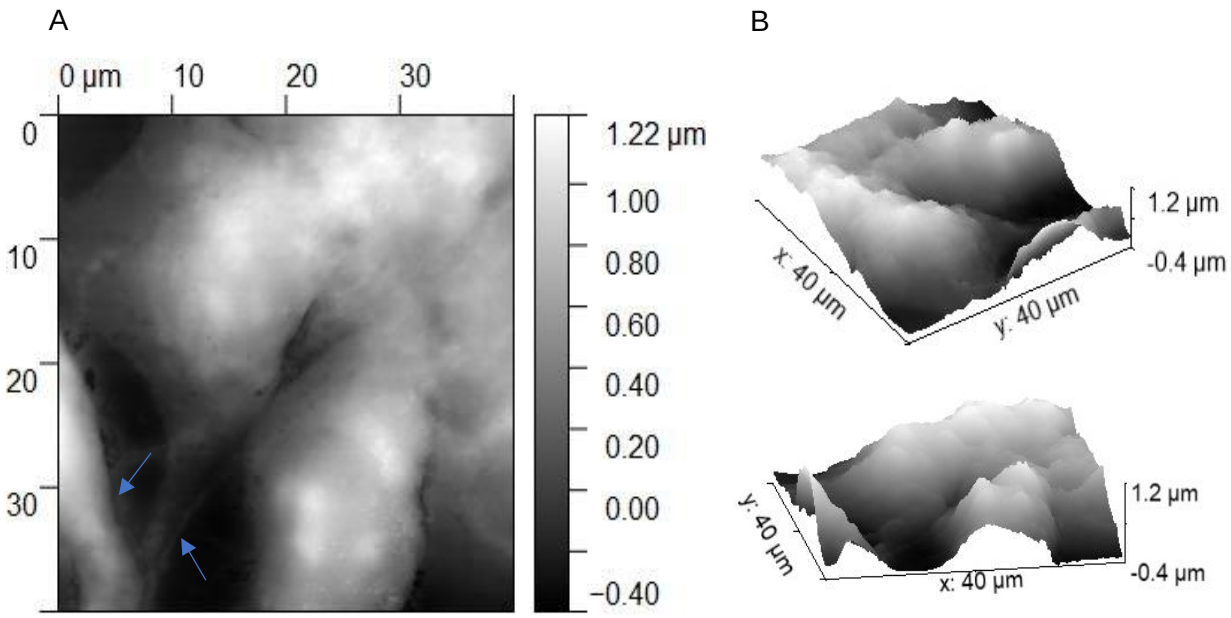

Figure 5-3. *A,* height image obtained of fixed HEK293 cells in a 40µm by 40µm square (see scale bar) in liquid tapping mode using 256 lines per image at a scan speed of 0.5µm/second. Blue arrows indicate possible filopodia extensions. *B,* 3D images of the same sample, showing the variations in height across the sample.

Once a suitable cell had been imaged at low magnification, the standard protocol was to select an area with minimal height differences to image with increasing magnification. Figure 5-4 shows one such example, where deformations and breaks in the cell membrane can be seen.

Figure 5-5 shows the same sample imaged with an increase in magnification. The features seen in the previous image can be more clearly seen and may show an area in the membrane where cells were in the process of dividing at the time of fixation.

As the magnification was increased small pores became visible in the membrane, however these were too large to be considered ion channel pores (see figure 5-6). From the 3D render it is clear that the AFM probe was beginning to catch on the surface of the membrane as the lines of the scan can be discerned. This is a common problem when imaging biological samples and can lead to the sample surface being distorted and appearing to be rougher.

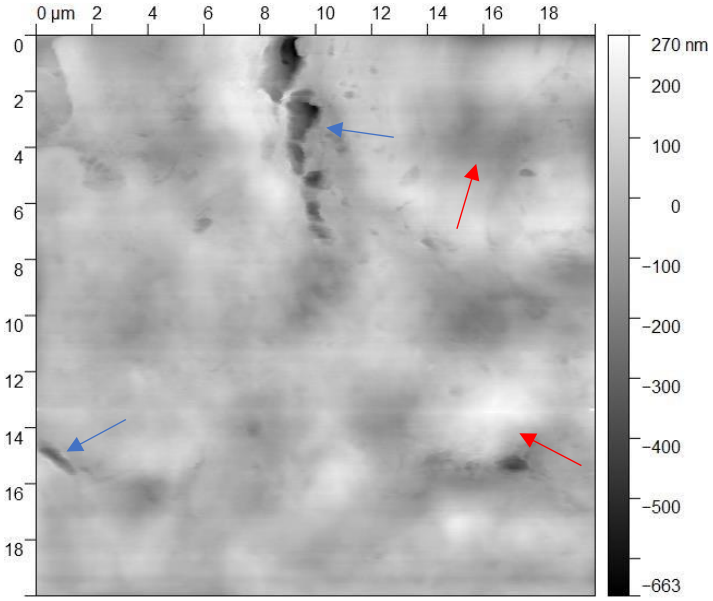

Figure 5-4. The surface of the cell membrane of a fixed HEK293 cell imaged using contact mode in air. Red arrows indicate where differences in the membrane height can be seen, where higher areas are shown in lighter shades and lower areas shaded darker (see scale bar). Blue arrows show clefts in the membrane possibly due to cell division. 512 lines were used to obtain the 20µm by 20µm square at a scan speed of 0.5µm/second. Image is displayed as height data.

Figure 5-5. The sample in figure 5-4 was imaged at a higher magnification in a 10µm by 10µm square. Shown is the 3D image (*A)* rendered from the original height data *(B).* Blue arrows indicate fissures in the cell membrane which could be attributed to cell division. To obtain the image the AFM probe moved at a speed of 0.4µm/second with 256 lines per sample using contact mode in air.

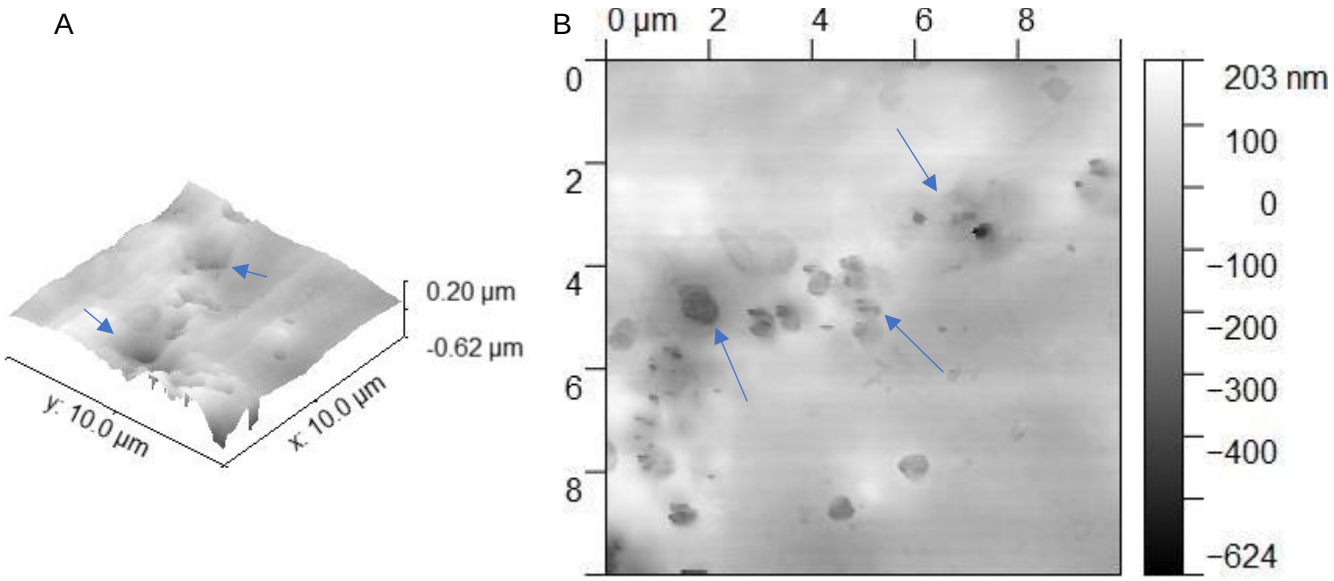

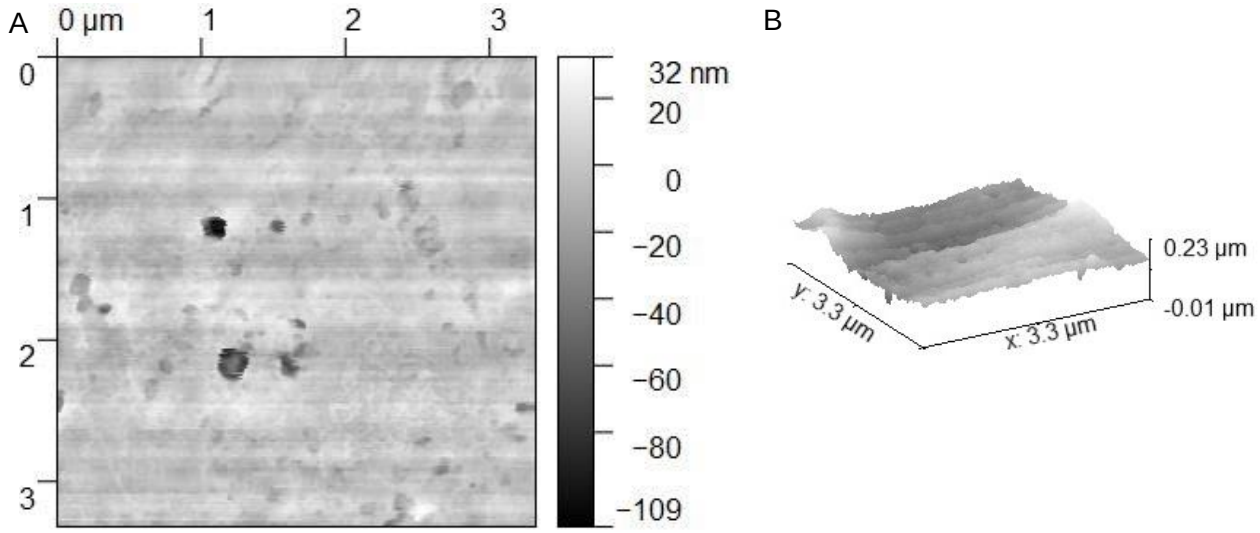

Figure 5-6. The sample in figure 5-4 and 5-5 was imaged at a higher magnification using a 3.32µm by 3.32µm square. *A* shows the height data obtained using 256 lines per sample at a scan speed of 0.4µm/second, while *B* shows the rendered 3D image of the same sample.

5.2.3 Images of non-expressing control cells and the hERG1a-HEK293 stable cell line

It was concluded that cells would have to be fixed using a 4% PFA solution to allow successful imaging. PFA cross-links cellular proteins which reduces the flexibility of the membrane, giving the AFM probe a stable surface upon which to image.

A sample of non-expressing and hERG-expressing cells were fixed and washed, then imaged in liquid tapping mode in dH_2O. The resulting images (see figure 5-7) demonstrate the morphological differences between the two samples, with the non-expressing negative control *(A)* having a smoother surface, although differences in the height data demonstrate that there are membrane structures present.

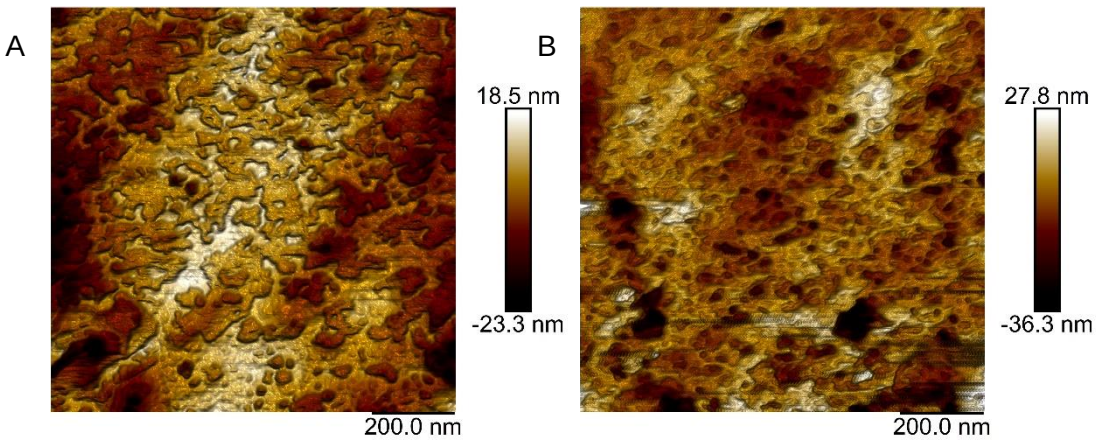

Figure 5-7. Morphological differences between non-expressing cells and the hERG-HEK293 stable cell line. *A*, image of a non-expressing cell and *B,* image of a hERG-HEK293 cell. Both samples have undergone fixation using a 4% solution of PFA made with a high $[K^+]$ solution of PBS. Images were obtained in liquid tapping mode and are displayed as height data.

In contrast, the expressing cell has a rougher surface with a high density of 'pockmark-like' structures which are low down within the membrane (shown by a darker colour, see scale bar). In comparison, the control cell membrane surface structures are further apart and descend less far into the membrane surface. These images suggest that the expression of numerous ion channels in a cell membrane creates morphological changes that can be seen even at a relatively low magnification.

5.2.4 Images of the hERG1a-HEK293 stable cell line

Upon imaging of the hERG-HEK293 stable cell line, structures could be observed on the surface of the cell membrane which appeared to be pores descending into the lipid bilayer. Figure 5-8 shows two samples (*A and C, B and D)*, demonstrating that the apparent pores are numerous across the cell surface. At a higher magnification (see figure 5-8, *C and D*) the pores became more discernible and were measured to be of 12-14nm in diameter. This is considerably larger than previous pore size estimates of 1.2nm for bacterial potassium channels. (Jiang et al., 2002).

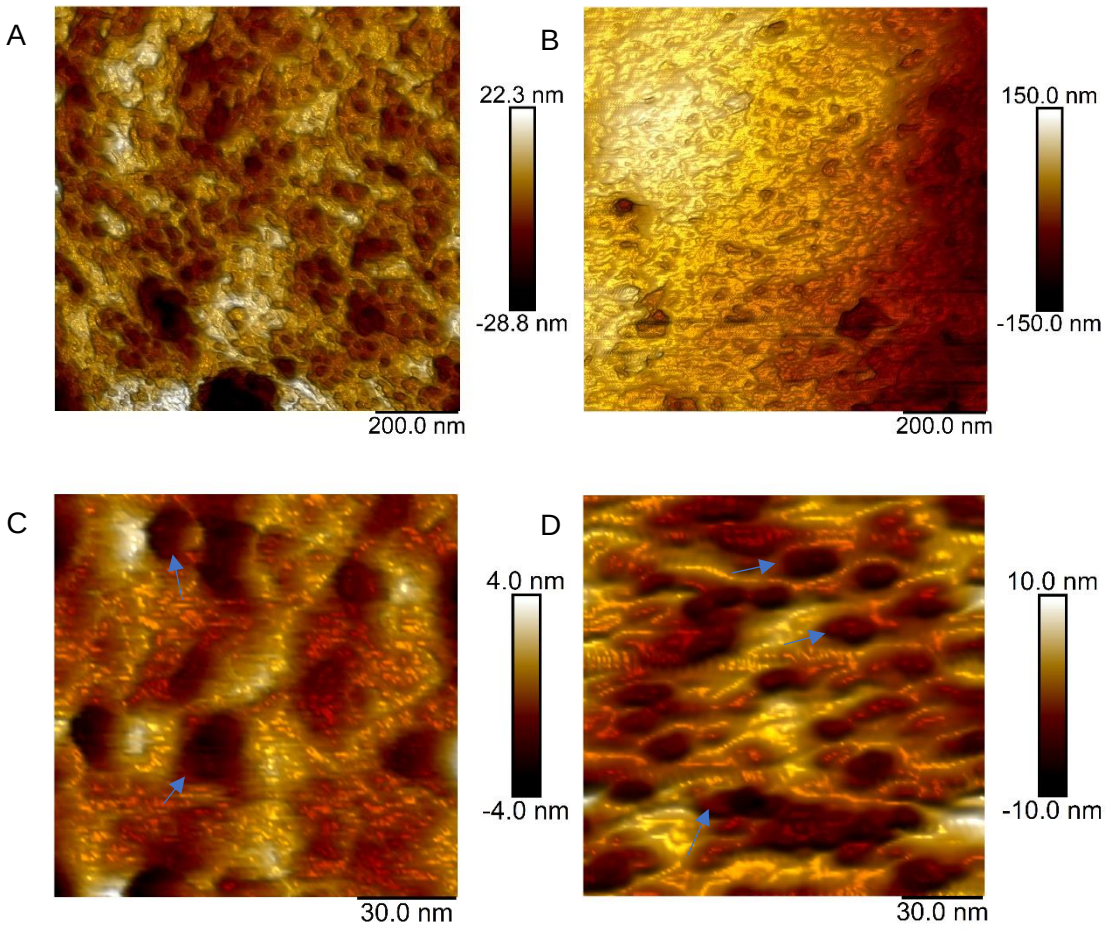

Figure 5-8. The membrane surface of the hERG-HEK293 stable cell line. Cells were fixed and dried prior to imaging in tapping mode in air, and images are shown as height data. Pores were visible on the membrane surface and at higher magnification *(C and D, see blue arrows)* the pores were measured to be 12-14nm in diameter and extended into the membrane 10nm and beyond.

The pores identified in the images had a sunken appearance and extended deep into the membrane, however the deepest measured was 10nm due to the limitations of the movement of the AFM probe. As the cells had been fixed in PFA and dried prior to imaging it was assumed that the channel had been pulled into the membrane as the cytoskeletal proteins were crosslinked (as a result of fixation) and as the cell contracted due to the drying process.

This would also explain the large measured pore diameter. If the channel had been pulled down into the membrane, the measured diameter represented the diameter of the whole ion channel, rather than the pore mouth. The diameter of the hERG channel was measured to be approximately 80Å from the cryo-EM structure (8nm) which is closer to the approximate diameter of the pores on the cell (Wang and MacKinnon, 2017). The remaining disparity in the measurements could be accounted for by the subunits being pulled so far down that the membrane was being pulled down alongside the channel and therefore was distorted, giving the appearance of a larger pore diameter.

5.2.5 Imaging in liquid tapping mode

As before, cells were fixed using a 4% PFA solution and were washed and maintained in water to enable imaging in liquid tapping mode. At a high magnification (a $2nm^2$ scanning size), structures on the surface of the cell membrane could be seen which appeared to be of tetrameric arrangement (see figure 5-9, *A and B*). The images show four sunken areas in the membrane which were presumed to be the four ion channel subunits pulled down into the membrane as a result of the fixation process.

Figure 5-9, *C* shows the trace and retrace (red and blue lines, respectively) of the top surface one of the tetramers which indicates the height variations across the sample surface. The indentations believed to be the tetramer subunits are indicated by black arrows, and the pore structure in the centre is indicated by a blue arrow. From the trace and AFM images the tetramer subunits were measured to be approximately 3nm apart, close to the ~2nm diameter of the pore mouth measured from the cryo-EM structure and from the ~2nm estimation from the diameter of hERG pore blockers (Vandenberg et al., 2017; Wang and MacKinnon, 2017).

The structure in the centre of the tetramer was measured to be approximately 1-3nm in height but varied enormously between tetramer samples. This structure was theorised to be an artefact of interactions between the tip of the AFM probe and salt crystals left within the pore from the PFA solution (Müller and Engel, 1997). This suggests the need for a more thorough washing protocol of the cells after fixation in order to remove any remaining detritus from the cell membrane surface.

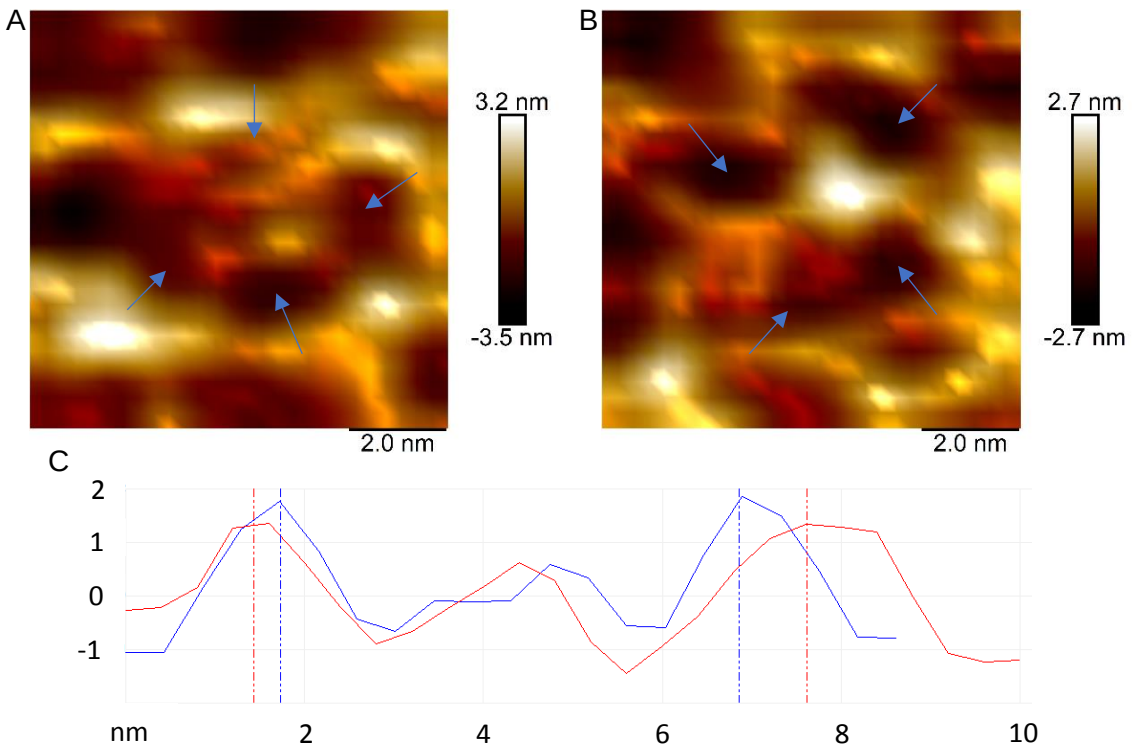

Figure 5-9. The tetrameric structures seen on the membrane of hERG-HEK293 cells. *A and B,* show examples of tetramers imaged on the cell membrane surface obtained in liquid tapping mode. Blue arrows indicate the suspected subunits of each tetramer. *C,* trace of the topography of one tetramer showing the indentations of the subunits of the tetramer (black arrows) and the raised structure within the pore (blue arrow).

5.3 Discussion

5.3.1 Structure of the tetramer

The images shown here provide evidence of a tetrameric structure present on the cell membrane of HEK293 cells which are stably expressing the hERG1a ion channel. Each structure shows four sunken regions which are hypothesised to be the four hERG subunits, around a central structure believed to be the pore. Given that hERG1a is known to be a tetramer, this is evidence that the AFM images show a channel in its native state in a cell membrane.

Previous AFM images of ion channels have shown clearly defined subunits of the channel protruding from the sample surface, possibly a result of the channels being mounted on a flat stable substrate which pushes the subunits upward out of the membrane (Marchesi et al., 2018; Heath and Scheuring, 2019). Despite this, it was expected that the hERG1a channel subunits may protrude slightly out of the membrane given that they have an extracellular domain (namely the S5-P linker). This was found not to be the case with the suspected channel subunits being sunken down within the membrane. This can be partly attributed to the PFA

solution used in the fixation process. PFA creates covalent links between proteins in a process known as cross-linking (Hobro and Smith, 2017; Kim et al., 2017). It is proposed that this caused the contraction of cytoskeletal proteins within the cell, which would in turn pull on the cytoplasmic domains of the channel resulting in the sunken appearance. However, this remains speculation until an ion channel can be imaged in a living cell membrane.

The measured diameter of the pore region (~3nm) is larger than suggested by previous studies of potassium channels. The pores of prokaryotic potassium channels such as KcsA and MthK have been suggested to be approximately 12Å (1.2nm) in diameter (Jiang et al., 2002). However the measurements obtained from these AFM images are not the pore diameter, rather they are the distance between the uppermost region of the subunits due to the ion channel being pulled down below the surface of the lipid bilayer. This reinforces the point that the imaging of ion channels in live cells is required to visualise channels in their native state.

5.3.2 Future AFM imaging of live cells

As found in this project, the main challenge when imaging live cells is the flexibility of the membrane which results in its deformation when the probe comes into contact. Although live mammalian cells have been imaged using AFM the limit on the resolution was deemed to be approximately 50-100nm, far from the resolution needed to resolve a single ion channel (Li et al., 2015). Aside from improved fixation processes, improvements in FM-AFM may represent the greatest chance of obtaining high resolution images of living cells given that it exerts little force on the membrane and therefore causes minimal deformation of the sample (Yang et al., 2007).

To further reduce the forces exerted on the cell, modification of the standard AFM probe tip may be required. A probe modified to be ~3µm in length was successfully employed to image live mammalian cells, with structures such as endocytic pits and filopodia extensions being resolved (Shibata et al., 2015). Such modifications alongside FM-AFM or HS-AFM may be effective in resolving ion channels being expressed in living cells in the future.

5.4 Conclusion

The images obtained here represent a significant achievement; evidence of a tetrameric structure in the membrane of a cell known to be expressing high levels of the hERG1a channel. Though the images do not provide as much data as images obtained when channels are adsorbed onto a mica surface, they do represent the ion channel in its native state despite the cell fixation process. In the future it is likely that AFM imaging in cell membranes will be used as an adjunct to imaging ion channels on a stabilised surface. The more stable surface (such

as mica) will allow measurements of pore diameters and other structural features while images obtained in cell membranes would be used to support the validity of these conclusions.

6. General Discussion

6.1 The ionic current of R528C-hERG1a in comparison with WT

The time course of both activation and inactivation of R528C-hERG1a current was faster when compared with WT-hERG1a, while the time course of deactivation was slower. Despite the kinetics of the channel being affected the voltage dependence of the channel was only marginally altered. Both $V_{0.5}$ of activation and inactivation were positively shifted, though less than was expected considering the loss of a charged arginine residue from the S4 voltage sensor (Tao et al., 2010). Therefore the contribution of R528 to movement of the S4 domain may be less extensive than previous studies have concluded, with neighbouring charged residues seeming to make up for the loss of the R528 positive charge.

The altered kinetics indicated mutation of R528 accelerated the transition of the channel into the active state, and then subsequently into the inactivated state. Therefore, it could be suggested that R528 stabilises the deactivated state of the channel through the formation of salt bridges with negative residues on other domains such as the nearby S1, S2 and S3 (Piper et al., 2005b, 2008; Zhang et al., 2005; Vandenberg et al., 2012). Loss of these salt bridges through the R528C mutation destabilised the deactivated state of S4, resulting in accelerated entry of the channel into the active and then inactivated states, with the slowed deactivation rate being further evidence that the deactivated channel conformation was an energetically unfavourable state in the R528C mutant.

The apparent decrease in R528C-hERG1a current density can be explained by the accelerated entry of R528C-hERG1a into the open and then inactivated state. The amplitude of the off gating current suggested that there are a similar, if not greater, number of functional R528C-hERG1a channels present, therefore a decrease in current density was not due to a channel biogenesis error. R528C-hERG1a channels spend less time in a conducting state for any given membrane voltage given the accelerated inactivation rate, resulting in the apparent reduction in current density when compared with WT-hERG1a.

The R528C mutation was found to shift the relative permeability of the channel (increasing its selectivity for Na^+ ions), suggesting that R528 modulates the selectivity filter through allosteric interactions. The S4 domain residues L529, L532 and V535 are known to interact directly with the S1 domain; given proximity of R528 to these identified residues it is likely that R528 also contributes to this S4-S1 interaction (see figure 6-1) (Wang and MacKinnon, 2017; Butler et al., 2019).

The S4-S1 interaction has been theorised to be transmitted to the selectivity filter by means of a pathway of aromatic residues (see figure 6-1). These aromatic residues (Y427 and F431 in S1, W568 and Y569 in S5, Y611 and F617 in the pore helix and W585 in the S5-P linker) form a network between S4-1, S1-5 and the S5-pore helix which transmits the gating movement of S4 to the selectivity filter (Butler et al., 2019). The interactions between helices along this pathway will be altered by the R528C mutation as the introduction of a cysteine residue will change the conformation of S4. This would have the downstream effect of changing the conformation of the S5-P linker and the selectivity filter, explaining the differences in the inactivation and selectivity of R528C-hERG when compared with WT-hERG1a.

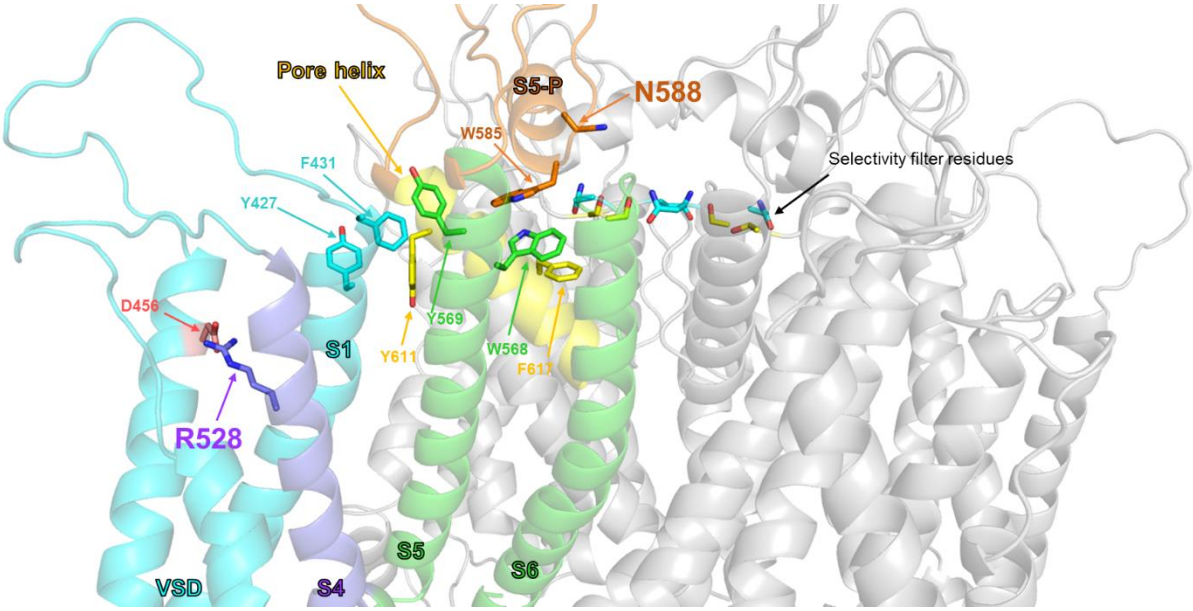

Figure 6-1. Interactions between the S4 and S1 helices can potentially affect both the S5-P linker involved in hERG1a channel inactivation and the selectivity filter which dictates the relative permeability of the channel. One subunit of hERG1a is shown in colour, with the remainder of the channel in grey for clarity. The VSD is shown in blue, the S4 voltage sensor in purple, S5 and S6 in green, the pore helix in yellow and the S5-P linker in orange. Y427, F431, Y611, W568, Y569, W585 and F617 are believed to be the aromatic residues which contribute to the pathway linking the movements of S4 to the S5-P linker and the selectivity filter. Structural images provided by Dr. Christopher Dempsey, University of Bristol.

Additionally, this would explain the similar effects of R528C and other mutations within the aromatic residue pathway, including the N588K-hERG1a mutant, on the inactivation and relative permeability of hERG. L532P, a mutation within the S4 helix, shifted the voltage dependence of inactivation by approximately +32mV, increased the permeability of the channel for Na^+ ions over K^+ ions (shown by an approximately 1.6-fold increase in the P_{Na}/P_K ratio relative to WT) and has been shown to disrupt the conformation of S4 (Colenso et al., 2013). I560T (in the S5 domain) shifted the voltage dependence of inactivation approximately +24.5mV and increased the P_{Na}/P_K ratio from 0.010 in WT-hERG1a to 0.016 (Butler et al., 2019). The N588K-hERG1a S5-P linker mutant, as previously stated, is inactivation-deficient

at physiological relevant potentials and has a P_{Na}/P_K ratio ~2.7 fold greater than that of WT-hERG1a (McPate et al., 2005).

These mutations have been found to have effects on both channel inactivation and channel selectivity, regardless of being in spatially distinct areas of the hERG channel. These mutants all modify the interaction between the S4, S1, S5, S5-P linker and pore helices at some point in the aromatic residue pathway, resulting in similar effects on hERG channel inactivation and relative permeability (Colenso et al., 2013; Butler et al., 2019). This highlights the highly mobile and allosteric nature of the channel, with all domains moving and interacting together to influence the biophysical properties of the channel.

6.2 The symmetry and asymmetry of the gating currents

The majority of WT-hERG1a gating currents (79%) were found to be asymmetric, with the on gating current being of smaller amplitude than the off. The R528C-hERG1a and N588K-hERG1a mutations both reduced the tendency of gating currents to display asymmetry, with 22% of R528C and 21% of N588K gating currents being classed as asymmetric.

6.2.1 The asymmetric gating current of WT-hERG1a

The asymmetry of the WT-hERG1a gating current can be explained using the kinetic properties of channel transitions between closed, open and inactivated states. Most WT-hERG1a channels (approximately 63%, as 62.9% of channels will open before or at the fitted time constant (τ) value) transitioned to the open state upon depolarisation, giving the outward transient seen in recordings due to the movement of the charged S4 voltage sensor (Tao et al., 2010). The remaining channels (approximately 37%) opened during the sustained depolarisation of the 50ms pulse, but the gating current from these channels was not resolved due to it being distributed over the duration of the pulse. Additionally during the pulse, some channels transitioned into the inactivated state and some transitioned back and forward through the whole linear gating scheme (Bett et al., 2011b).

All channels that were opened, whether immediately after the depolarisation or during the length of the pulse, made the transition from the open or inactivated state to the closed state upon repolarisation. This again involved movement of the charged S4 voltage sensor resulting in an inward transient being recorded (Piper et al., 2003b). This transient comprised of the closure of all channels that opened during the entire length of the pulse, and therefore was of a larger amplitude than the initial outward transient which comprised only of the channels which opened immediately after the depolarising pulse (see figure 6-2, *A*).

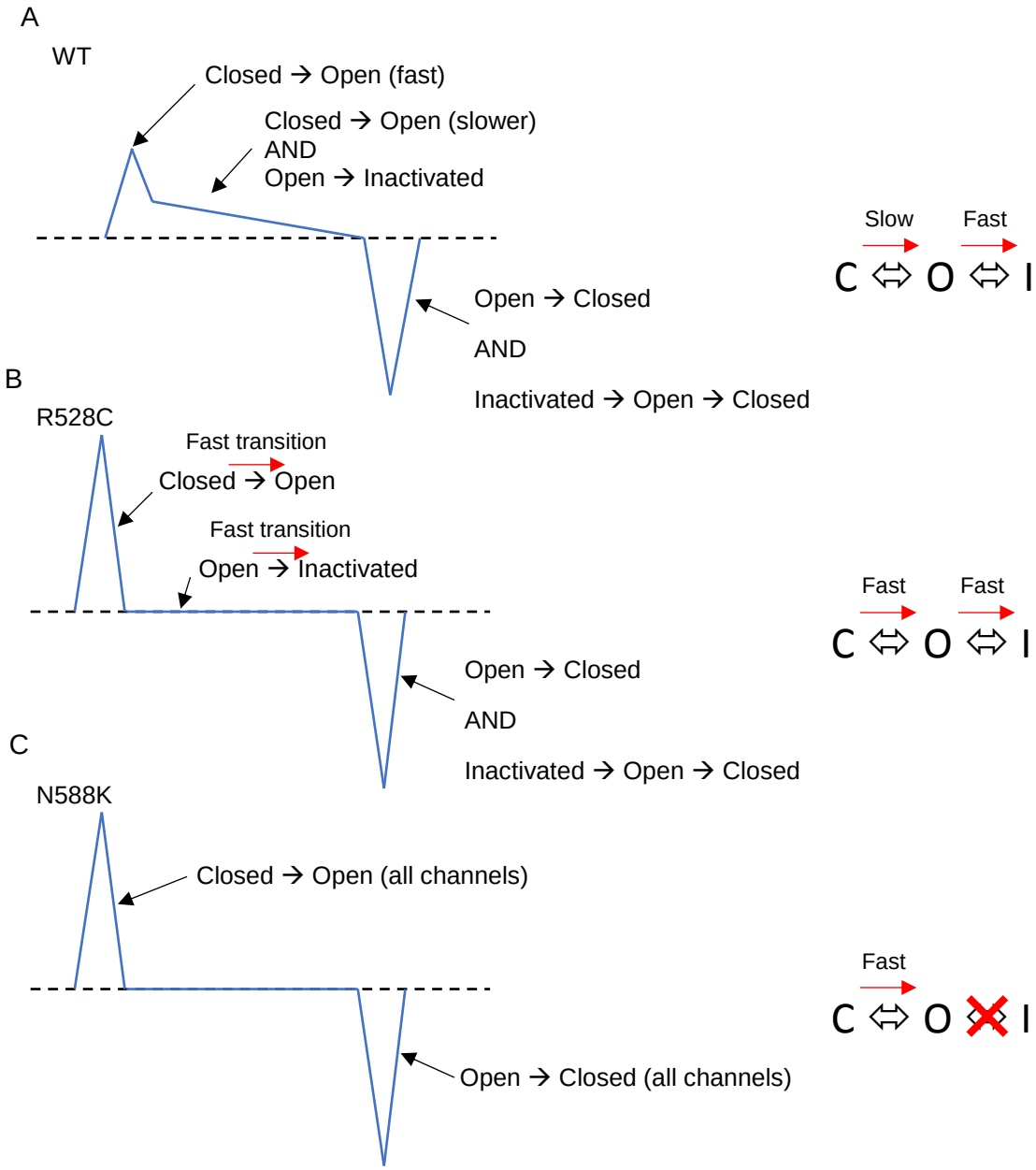

Figure 6-2. The transitions of the channel state during the on and off gating currents. *A,* in WT-hERG1a most channels opened upon depolarisation while some opened later during the pulse. Upon repolarisation all channels that were opened transitioned to the closed state, either from the inactivated or closed state. *B,* R528C-hERG1a channels quickly activated upon depolarisation due to the increased activation rate. During the pulse channels quickly transitioned into the inactivated state and remained in this state. Upon repolarisation, as in WT-hERG1a, all channels that were opened throughout the pulse transitioned to the closed state, either from the inactivated or closed state. *C,* N588K-hERG1a is inactivation deficient, therefore upon depolarisation channels quickly opened but did not transition into the inactivate state. Upon repolarisation all channels which opened at the beginning of the pulse transitioned into the closed state.

This was supported by the findings from the voltage protocol which increased the duration of the depolarising pulse used to elicit gating currents. The gating current ratio decreased in magnitude as the pulse duration increased, however the gating charge ratio for the same experiment showed no decrease in ratio with increasing pulse duration. The gating charge was

measured across the whole pulse duration and therefore accounted for both slow and fast channel openings. Consequently, the on gating charge was equivalent to the off gating charge at all pulse durations, resulting in the ratio being approximately unchanged throughout the experiment.

Though not statistically significant, the decrease in the current ratio indicated that more channels transitioned from the closed to the open state as the pulse duration increased, resulting in a larger amplitude off transient. When decreasing the length of the pulse the component comprising of the slowly opening channels was lost, resulting in more symmetric gating currents.

6.2.2 The symmetric gating current of R528C-hERG1a

The majority of gating currents were symmetric (78%) in the R528C-hERG1a mutant. The on gating current again represented channels that transitioned from the closed to open states, but R528C-hERG1a was found to have a faster activation rate compared with WT-hERG1a (see chapter 2). As a result, more of the channel population opened at the beginning of the depolarising pulse resulting in a large on gating current.

During the depolarising pulse channels then transitioned into the inactivated state; this transition has been shown (by a decreased τ of inactivation) to be faster in the R528C mutant than in WT-hERG1a channels (see chapter 2). As previously stated, the whole cell macroscopic current of R528C-hERG1a was shown to be significantly smaller than that of WT-hERG1a even when corrected for cell surface area. This can be interpreted as the R528C mutant not only transitioning to the inactivated state at a faster rate, but also preferentially staying in the non-conducting inactivated state. This faster transition into and preference to stay in the inactivated state resulted in fewer transitions from state to state during the depolarising pulse.

Upon repolarisation the current elicited only represented the channels which opened at the beginning of the pulse due to the accelerated activation rate. Therefore fewer channels opened during the depolarising pulse, resulting in an off gating current that was symmetric to the on gating current (see figure 6-2, *B*).

6.2.3 The symmetric gating current of N588K-hERG1a

The gating currents of the N588K-hERG1a mutant, like R528C-hERG1a, were predominately symmetric. The on gating current again represented the transition of the channels from the closed to open state. The N588K mutant is inactivation deficient at the range of membrane potentials used in the gating current protocol, therefore during the depolarising pulse there was

no further transition into the inactivated state. As a result, the channels remained in the open state until membrane repolarisation, which elicited an inward transient. This was equal to the outward transient and represented the transition of all channels from the open to the closed state (see figure 6-2, *C*).

6.3 AFM and ion channels

Though the original AFM aims of this project were not met, an image of a tetrameric structure on the membrane of a hERG1a-HEK293 cell remains a considerable achievement. Live mammalian cells have been successfully imaged using HS-AFM, however this was for the purposes of imaging morphological changes such as extensions of filopodia and endocytosis of vesicles which occur at a greater scale than that of a single ion channel (Shibata et al., 2017). Nevertheless, this achievement shows what is possible in terms of imaging live cells with flexible membranes given the right conditions and appropriate technological modifications.The use of AFM to study ion channels remains relevant even if the channels are not in their native state, given findings such as a possible gating mechanism of CNG channels (Marchesi et al., 2018). With continued advancements in the field of AFM, such as probe modifications, increasing speed of imaging as well as higher frequency feedback systems (therefore more able to compensate for the flexibility of the cell membrane), achievement of the AFM aims of this project could be expected in the not too distant future. This could be extended to other ion channels which have already been studied in reconstituted membranes or adsorbed onto a mica surface, and should help to support the conclusions reached in those studies.

6.4 Conclusion

The R528C and N588K mutations both affect the inactivation and relative permeability of the WT-hERG1a channel despite being located in distinct regions of the channel. This supports the hypothesis that there is a network of aromatic residues which transmits the movement of the S4 voltage sensor to the pore region and selectivity filter of the channel upon activation and deactivation of the channel. Furthermore, the differences in gating kinetics between WT-hERG1a, R528C-hERG1a and N588K-hERG1a as a result of altered channel movement can explain the tendency of WT gating currents to be asymmetric while the mutants tend towards symmetric gating currents.

Though there are many adjustments which must be made to the current technologies and methodologies (in terms of AFM and molecular biology being employed together), AFM

continues to be a powerful biological research tool. Faster scanning times, probe modifications and even improved fixation techniques will improve the ease and success of the imaging of biological samples, therefore AFM stands to provide a wealth of ion channel structural data in the future.

Bibliography

Anantharam, A., and Abbott, G.W. (2005). Does hERG Coassemble with a β Subunit? Evidence for Roles of MinK and MiRP1. Novartis Found Symp *266*: 100–117.

Andalib, P., Consiglio, J.F., Trapani, J.G., and Korn, S.J. (2004). The external TEA binding site and C-type inactivation in voltage-gated potassium channels. Biophys. J. *87*: 3148–3161.

Arcangeli, A., and Becchetti, A. (2017). hERG Channels: From Antitargets to Novel Targets for Cancer Therapy. Clin. Cancer Res. *23*: 3–5.

Armstrong, C.M. (1981). Sodium Channels and Gating Currents. Physiol. Rev. *61*: 664–683.

Balasuriya, D., D'sa, L., Talker, R., Dupuis, E., Maurin, F., Martin, P., et al. (2014). A Direct Interaction between the Sigma-1 Receptor and the hERG Voltage-gated K Channel Revealed by Atomic Force Microscopy and Homogeneous Time-resolved Fluorescence (HTRF). J. Biol. Chem. *289*: 32353–32363.

Bett, G.C.L., Dinga-Madou, I., Zhou, Q., Bondarenko, V.E., and Rasmusson, R.L. (2011a). A Model of the Interaction between N-type and C-type Inactivation in Kv1.4 Channels. Biophysj *100*: 11–21.

Bett, G.C.L., Zhou, Q., and Rasmusson, R.L. (2011b). Models of HERG gating. Biophys. J. *101*: 631–42.

Bezanilla, F. (2018). Gating currents. J. Gen. Physiol *150*: 911–932.

Bezanilla, F., Perozo, E., and Stefani, E. (1994a). Gating of Shaker K+ channels: II. The components of gating currents and a model of channel activation. Biophys. J. *66*: 1011–1021.

Bezanilla, M., Drake, B., Nudler, E., Kashlev, M., Hansma, P.K., and Hansma, H.G. (1994b). Motion and enzymatic degradation of DNA in the atomic force microscope. Biophys. J. *67*: 2454–2459.

Binnig, G., Quate' ', C.F., Gi, E.L., and Gerber, C. (1986). Atomic Force Microscope. Phys.

Rev. Lett. *56*: 930–934.

Bisset, D., and Chung, S.-H. (2008). Efficacy of external tetraethylammonium block of the KcsA potassium channel: Molecular and Brownian dynamics studies. Biochim. Biophys. Acta *1778*: 2273–2282.

Brugada, R., Hong, K., Dumaine, R., Cordeiro, J., Gaita, F., Borggrefe, M., et al. (2004). Sudden Death Associated with Short-QT Syndrome Linked to Mutations in HERG. Circulation *109*: 30–35.

Butler, A., Zhang, Y., Stuart, A.G., Dempsey, C.E., and Hancox, J.C. (2019). Functional and pharmacological characterization of an S5 domain hERG mutation associated with short QT syndrome. Heliyon *5*: e01429.

Casuso, I., Khao, J., Chami, M., Paul-Gilloteaux, P., Husain, M., Duneau, J.P., et al. (2012). Characterization of the motion of membrane proteins using high-speed atomic force microscopy. Nat. Nanotechnol. *7*: 525–529.

Catterall, W. (2000). From Ionic Currents to Molecular Review Mechanisms: The Structure and Function of Voltage-Gated Sodium Channels. Neuron *26*: 13–25.

Catterall, W.A. (2010). Ion Channel Voltage Sensors: Structure, Function, and Pathophysiology. Neuron *67*: 915–928.

Ceccarini, L., Masetti, M., Cavalli, A., and Recanatini, M. (2012). Ion Conduction through the hERG Potassium Channel. PLoS One *7*: e49017.

Cheng, Y.M., and Claydon, T.W. (2012). Voltage-dependent gating of hERG potassium channels. Front. Pharmacol. *3*: 1–17.

Chiesa, N., Rosati, B., Arcangeli, A., Olivotto, M., and Wanke, E. (1997). A novel role for HERG K+ channels: spike-frequency adaptation. J. Physiol. *501*: 313–318.

Choi, K.H., Song, C., Shin, D., and Park, S. (2011). HERG channel blockade by externally applied quaternary ammonium derivatives. Biochim. Biophys. Acta - Biomembr. *1808*: 1560–1566.

Chtcheglova, L.A., Atalar, F., Ozbek, U., Wildling, L., Ebner, A., and Hinterdorfer, P. (2008). Localization of the ergtoxin-1 receptors on the voltage sensing domain of hERG K + channel by AFM recognition imaging. Eur. J. Physiol. 247–254.

Codding, S.J., and Trudeau, M.C. (2019). The hERG potassium channel intrinsic ligand regulates N-and C-terminal interactions and channel closure. J. Gen. Physiol *151*: 478–488.

Colenso, C.K., Sessions, R.B., Zhang, Y.H., Hancox, J.C., and Dempsey, C.E. (2013). Interactions between Voltage Sensor and Pore Domains in a hERG K + Channel Model from Molecular Simulations and the Effects of a Voltage Sensor Mutation. J. Chem. Inf. Model. *53*: 1358–1370.

Cordeiro, J.M., Brugada, R., Wu, Y.S., Hong, K., and Dumaine, R. (2005). Modulation of IKr inactivation by mutation N588K in KCNH2: A link to arrhythmogenesis in short QT syndrome. Cardiovasc. Res. *67*: 498–509.

Crotti, L., Celano, G., Dagradi, F., and Schwartz, P.J. (2008). Congenital long QT syndrome. Orphanet J. Rare Dis. *3*:.

DeCoursey, T.E. (2018). Gating currents indicate complex gating of voltage-gated proton channels. Proc. Natl. Acad. Sci. U. S. A. *115*: 9057–9059.

Dou, Y., Macdonald, L.C., Wu, Y., and Fedida, D. (2017). The Fast Component of hERG Gating Charge: An Interaction between D411 in the S1 and S4 Residues. Biophys. J. *113*: 1979–1991.

Dufrêne, Y.F., Ando, T., Garcia, R., Alsteens, D., Martinez-Martin, D., Engel, A., et al. (2017). Imaging modes of atomic force microscopy for application in molecular and cell biology. Nat. NanotechnologyNOLOGY *12*: 295–307.

Elliott, D.J.S., Dondas, N.Y., Munsey, T.S., and Sivaprasadarao, A. (2009). Movement of the S4 segment in the hERG potassium channel during membrane depolarization. Mol. Membr. Biol. *26*: 435–47.

Es-Salah-Lamoureux, Z., Fougere, R., Xiong, P.Y., Robertson, G.A., and Fedida, D. (2010). Fluorescence-Tracking of Activation Gating in Human ERG Channels Reveals Rapid S4 Movement and Slow Pore Opening. PLoS One *5*:.

Farrelly, A.M., Ro, S., Callaghan, B.P., Khoyi, M.A., Fleming, N., Horowitz, B., et al. (2003). Expression and function of KCNH2 (HERG) in the human jejunum. Am. J. Physiol. - Gastrointest. Liver Physiol. *284*: G883–G895.

Fedida, D., Es-Salah-Lamoureux, Z., Dou, Y., and Wang, Z. (2012). hERG Activation Gating Is Rapid: Evidence from Gating-Current Recordings and MTSET Modification of the Voltage Sensor. Hear. Rhythm *9*: 1913–1914.

Ferrer, T., Rupp, J., Piper, D.R., and Tristani-Firouzi, M. (2006). The S4-S5 linker directly couples voltage sensor movement to the activation gate in the human ether-a'-go-go-related gene (hERG) K+ channel. J. Biol. Chem. *281*: 12858–12864.

Fougere, R.R., Es-Salah-Lamoureux, Z., Rezazadeh, S., Eldstrom, J., and Fedida, D. (2011). Functional characterization of the LQT2-causing mutation R582C and the associated voltage-dependent fluorescence signal. Hear. Rhythm *8*: 1273–1280.

Giudicessi, J.R., Wilde, A.A.M., and Ackerman, M.J. (2018). The genetic architecture of long QT syndrome: A critical reappraisal. Trends Cardiovasc Med *28*: 453–464.

Goodchild, S.J., and Fedida, D. (2014). Gating charge movement precedes ionic current activation in hERG channels. Channels (Austin). *8*: 84–9.

Goodchild, S.J., Macdonald, L.C., and Fedida, D. (2015). Sequence of gating charge movement and pore gating in HERG activation and deactivation pathways. Biophys. J. *108*: 1435–1447.

Gravel, A.E., Arnold, A.A., Dufourc, E.J., and Marcotte, I. (2013). An NMR investigation of the structure, function and role of the hERG channel selectivity filter in the long QT syndrome. Biochim. Biophys. Acta - Biomembr. *1828*: 1494–1502.

Grunnet, M., Goldin Diness, T., Schultz Hansen, R., and Olesen, S.-P. (2008). Characterization of the Short QT Mutation hERG-N588K Reveals a Mixed Gain-and Loss-of-Function. Cell. Physiol. Biochem. *22*: 611–624.

Gustina, A.S., and Trudeau, M.C. (2009). A recombinant N-terminal domain fully restores deactivation gating in N-truncated and long QT syndrome mutant hERG potassium channels. Proc. Natl. Acad. Sci. U. S. A. *106*: 13082–13087.

Gustina, A.S., and Trudeau, M.C. (2012). HERG potassium channel regulation by the N-terminal eag domain. Cell. Signal. *24*: 1592–1598.

Harchi, A. El, Melgari, D., Zhang, Y.H., Zhang, H., and Hancox, J.C. (2012). Action potential clamp and pharmacology of the variant 1 Short QT Syndrome T618I hERG K^+ channel. PLoS One *7*: e52451.

Heath, G.R., and Scheuring, S. (2019). Advances in high-speed atomic force microscopy (HS-AFM) reveal dynamics of transmembrane channels and transporters. Curr. Opin. Struct. Biol. *57*: 93–102.

Henderson, E., Haydon, P.G., and Sakaguchi, D.S. (1992). Actin filament dynamics in living glial cells imaged by atomic force microscopy. Science (80-.). *257*: 1944–1946.

Hill, W.G., Southern, N.M., MacIver, B., Potter, E., Apodaca, G., Smith, C.P., et al. (2005). Isolation and characterization of the Xenopus oocyte plasma membrane: A new method for studying activity of water and solute transporters. Am. J. Physiol. - Ren. Physiol. *289*: F217–

F224.

Hobro, A.J., and Smith, N.I. (2017). An evaluation of fixation methods: Spatial and compositional cellular changes observed by Raman imaging. Vib. Spectrosc. *91*: 31–45.

Hodgkin, A.L., and Huxley, A.F. (1952). A quantitative description of membrane current and its application to conduction and excitation in nerve. J. Physiol *117*: 500–544.

Hong, K., Bjerregaard, P., Gussak, I., and Brugada, R. (2005). Short QT syndrome and atrial fibrillation caused by mutation in KCNH2. J. Cardiovasc. Electrophysiol. *16*: 394–6.

Hoshi, T., and Armstrong, C.M. (2013). C-type inactivation of voltage-gated K+ channels: pore constriction or dilation? J. Gen. Physiol. *141*: 151–60.

Hoshi, T., Zagotta, W.N., and Aldrich, R.W. (1990). Biophysical and molecular mechanisms of Shaker potassium channel inactivation. Science (80-.). *250*: 533–538.

Ido, S., Kimiya, H., Kobayashi, K., Kominami, H., Matsushige, K., and Yamada, H. (2014). Immunoactive two-dimensional self-assembly of monoclonal antibodies in aqueous solution revealed by atomic force microscopy. Nat. Mater. *13*: 264–270.

Ido, S., Kimura, K., Oyabu, N., Kobayashi, K., Tsukada, M., Matsushige, K., et al. (2013). Beyond the Helix Pitch: Direct Visualization of Native DNA in Aqueous Solution. Am. Chem. Soc. Nano *7*: 1817–1822.

Jiang, M., Dun, W., and Tseng, G.-N. (1999). Mechanism for the effects of extracellular acidification on HERG-channel function. Hear. Circ. Physiol *46*: 1283–1292.

Jiang, M., Zhang, M., Maslennikov, I. V., Liu, J., Wu, D.M., Korolkova, Y. V., et al. (2005). Dynamic conformational changes of extracellular S5-P linkers in the hERG channel. J. Physiol. *569*: 75–89.

Jiang, Y., Lee, A., Chen, J., Cadene, M., Chait, B.T., and MacKinnon, R. (2002). The open pore conformation of potassium channels. Nature *417*: 523–526.

Kim, S.-O., Kim, J., Okajima, T., and Cho, N.-J. (2017). Mechanical properties of paraformaldehyde-treated individual cells investigated by atomic force microscopy and scanning ion conductance microscopy. Nano Converg. *4*: 1–8.

Krieg, M., Fläschner, G., Alsteens, D., Gaub, B.M., Roos, W.H., L Wuite, G.J., et al. (2019). Atomic force microscopy-based mechanobiology. Nat. Rev. Phys. *1*: 41–57.

Lal, S., Scarinci, N., Perez, P.L., Rocío Cantero, M. del, and Cantiello, H.F. (2018). Lipid bilayer-atomic force microscopy combined platform records simultaneous electrical and

topological changes of the TRP channel polycystin-2 (TRPP2). PLoS One *13*: e0202029.

Li, M., Liu, L.Q., Xi, N., and Wang, Y.C. (2015). Nanoscale monitoring of drug actions on cell membrane using atomic force microscopy. Acta Pharmacol. Sin. *36*: 769–782.

Li, Y., Ng, H.Q., Li, Q., and Kang, C.B. (2016). Structure of the Cyclic Nucleotide-Binding Homology Domain of the hERG Channel and Its Insight into Type 2 Long QT Syndrome. Sci. Rep. *6*: 1–10.

Liu, J., Zhang, M., Jiang, M., and Tseng, G.-N. (2003). Negative charges in the transmembrane domains of the HERG K channel are involved in the activation- and deactivation-gating processes. J. Gen. Physiol. *121*: 599–614.

Liu, X., Ping, H., and Zhang, C. (2014). Rapid establishment of a HEK 293 cell line expressing FVIII-BDD using AAV site-specific integration plasmids. BMC Res. Notes *7*: 1–6.

Loewe, A., Wilhelms, M., Fischer, F., Scholz, E.P., Dö Ssel, O., and Seemann, G. (2014). Arrhythmic potency of human ether-a `-go-go-related gene mutations L532P and N588K in a computational model of human atrial myocytes. Europace *16*: 435–443.

M Smith, G.A., Tsui, H.-W., Newell, E.W., Jiang, X., Zhu, X.-P., L Tsui, F.W., et al. (2002). Functional Up-regulation of HERG K Channels in Neoplastic Hematopoietic Cells. J. Biol. Chem. *24*: 18528–18534.

Marchesi, A., Gao, X., Adaixo, R., Rheinberger, J., Stahlberg, H., Nimigean, C., et al. (2018). An iris diaphragm mechanism to gate a cyclic nucleotide-gated ion channel. Nat. Commun. *9*: 1–11.

Mauerhöfer, M., and Bauer, C.K. (2016). Effects of Temperature on Heteromeric Kv11.1a/1b and Kv11.3 Channels. Biophys. J. *111*: 504–523.

McPate, M.J., Duncan, R.S., Milnes, J.T., Witchel, H.J., and Hancox, J.C. (2005). The N588K-HERG K+ channel mutation in the 'short QT syndrome': Mechanism of gain-in-function determined at 37°C. Biochem. Biophys. Res. Commun. *334*: 441–449.

Meer, G. Van, Voelker, D.R., and Feigenson, G.W. (2008). Membrane lipids: Where they are and how they behave. Nat. Rev. Mol. Cell Biol. *9*: 112–124.

Morais-Cabral, J.H., Zhou, Y., and MacKinnon, R. (2001). Energetic optimization of ion conduction rate by the K + selectivity filter.

Morais Cabral, J.H., Lee, A., Cohen, S.L., Chait, B.T., Li, M., and Mackinnon, R. (1998). Crystal structure and functional analysis of the HERG potassium channel N terminus: A eukaryotic PAS domain. Cell *95*: 649–655.

Müller, D.J., and Engel, A. (1997). The height of biomolecules measured with the atomic force microscope depends on electrostatic interactions. Biophys. J. *73*: 1633–1644.

Nerbonne, J.M., and Kass, R.S. (2005). Molecular Physiology of Cardiac Repolarization. Physiol. Rev. *85*: 1205–1253.

Noda, M., Ikeda, T., Kayano, T., Suzuki, H., Takeshima, H., Kurasaki, M., et al. (1986). Existence of distinct sodium channel messenger RNAs in rat brain. Nature *320*: 188–192.

Noda, M., Shimizu, S., Tanabe, T., Takai, T., Kayano, T., Ikeda, T., et al. (1984). Primary structure of Electrophorus electricus sodium channel deduced from cDNA sequence. Nature *312*: 121–127.

Perissinotti, L.L., Biase, P.M. De, Guo, J., Yang, P.C., Lee, M.C., Clancy, C.E., et al. (2018). Determinants of isoform-specific gating kinetics of hERG1 channel: Combined experimental and simulation study. Front. Physiol. *9*: 1–20.

Perrin, M.J., Subbiah, R.N., Vandenberg, J.I., and Hill, A.P. (2008). Human ether-a-go-go related gene (hERG) K+ channels: Function and dysfunction. Prog. Biophys. Mol. Biol. *98*: 137–148.

Piper, D., Sanguinetti, M., and Tristani-Firouzi, M. (2005a). Voltage Sensor Movement in the hERG K+ channel. Novartis Found Symp *266*: 46–52.

Piper, D.R., Hinz, W.A., Tallurri, C.K., Sanguinetti, M.C., and Tristani-Firouzi, M. (2005b). Regional specificity of human ether-a'-go-go-related gene channel activation and inactivation gating. J. Biol. Chem. *280*: 7206–7217.

Piper, D.R., Rupp, J., Sachse, F.B., Sanguinetti, M.C., and Tristani-Firouzi, M. (2008). Cooperative interactions between R531 and acidic residues in the voltage sensing module of hERG1 channels. Cell. Physiol. Biochem. *21*: 37–46.

Piper, D.R., Varghese, A., Sanguinetti, M.C., and Tristani-Firouzi, M. (2003a). Gating currents associated with intramembrane charge displacement in HERG potassium channels. Proc. Natl. Acad. Sci. U. S. A. *100*: 10534–9.

Piper, D.R., Varghese, A., Sanguinetti, M.C., and Tristani-Firouzi, M. (2003b). Gating currents associated with intramembrane charge displacement in HERG potassium channels. Proc. Natl. Acad. Sci. *100*: 10534–10539.

Ponce, A., Castillo, A., Hinojosa, L., Martinez-Rendon, J., and Cereijido, M. (2018). The expression of endogenous voltage-gated potassium channels in HEK293 cells is affected by culture conditions. Physiol Rep *6*: e13663.

Rangl, M., Miyagi, A., Kowal, J., Stahlberg, H., Nimigean, C.M., and Scheuring, S. (2016). Real-time visualization of conformational changes within single MloK1 cyclic nucleotide-modulated channels. Nat. Commun. *7*: 1–8.

Ridley, J.M., Milnes, J.T., Zhang, Y.H., Witchel, H.J., and Hancox, J.C. (2003). Inhibition of HERG K+ current and prolongation of the guinea-pig ventricular action potential by 4-aminopyridine. J. Physiol. *549*: 667–672.

Ruan, Y., Kao, K., Lefebvre, S., Marchesi, A., Corringer, P.-J., Hite, R.K., et al. (2018). Structural titration of receptor ion channel GLIC gating by HS-AFM. PNAS *115*: 10333–10338.

Ruan, Y., Miyagi, A., Wang, X., Chami, M., Boudker, O., and Scheuring, S. (2017). Direct visualization of glutamate transporter elevator mechanism by high-speed AFM. Proc. Natl. Acad. Sci. U. S. A. *114*: 1584–1588.

Salkoff, L., Butler, A., Wei, A., Scavarda, N., Giffen, K., Ifune, C., et al. (1987). Genomic organization and deduced amino acid sequence of a putative sodium channel gene in Drosophila. Science (80-.). *237*: 744–749.

Sanguinetti, M.C. (2004). Two components of cardiac delayed rectifier K+ current. Differential sensitivity to block by class III antiarrhythmic agents. J. Gen. Physiol. *96*: 195–215.

Sanguinetti, M.C., Jiang, C., Curran, M.E., and Keating, M.T. (1995a). A mechanistic link between an inherited and an acquird cardiac arrthytmia: HERG encodes the IKr potassium channel. Cell *81*: 299–307.

Sanguinetti, M.C., Jiang, C., Curran, M.E., and Keating, M.T. (1995b). A mechanistic link between an inherited and an acquired cardiac arrhythmia: HERG encodes the IKr potassium channel. Cell *81*: 299–307.

Sanguinetti, M.C., and Tristani-Firouzi, M. (2006). hERG potassium channels and cardiac arrhythmia. Nature *440*: 463–469.

Sasaki, S., McCully, J.D., Alessandrini, F., and LoCicero, J. (1995). Impact of initial flush potassium concentration on the adequacy of lung preservation. J. Thorac. Cardiovasc. Surg. *109*: 1090–1096.

Shibata, M., Uchihashi, T., Ando, T., and Yasuda, R. (2015). Long-tip high-speed atomic force microscopy for nanometer-scale imaging in live cells. Sci. Rep. *5*: 1–7.

Shibata, M., Watanabe, H., Uchihashi, T., Ando, T., and Yasuda, R. (2017). High-speed atomic force microscopy imaging of live mammalian cells. Biophys. Physicobiology *14*: 127–135.

Shinozaki, Y., Sumitomo, K., and Tanaka, A. (2014). Ligand-induced structural changes in a

membrane-reconstituted ion channel observed with atomic force microscopy. Appl. Phys. Express *7*: 1–3.

Sigel, E. (1990). Use of Xenopus Oocytes for the Functional Expression of Plasma Membrane Proteins. J. Membr. Biol *117*: 201–221.

Smith, P.L., Baukrowitz, T., and Yellen, G. (1996). The inward rectification mechanism of the HERG cardiac potassium channel. Nature *379*: 833–836.

Smith, P.L., and Yellen, G. (2002). Fast and Slow Voltage Sensor Movements in HERG Potassium Channels. J. Gen. Physiol *119*: 275–293.

Song, M., Raphaelli, K., Jones, M.L., Aliabadi-Zadeh, K., Leung, K.M., Crowley, D., et al. (2011). Clonal selection of high producing, stably transfected HEK293 cell lines utilizing modified, high-throughput FACS screening. J. Chem. Technol. Biotechnol. *86*: 935–941.

Splawski, I., Shen, J., Timothy, K.W., Lehmann, M.H., Priori, S., Robinson, J.L., et al. (2000). Spectrum of mutations in Long-QT Syndrome genes: KVLQT1, HERG, SCN5A, KCNE1, and KCNE2. Circulation *102*: 1178–1185.

Stefani, E., and Bezanilla, F. (1998). Cut-open oocyte voltage-clamp technique. Methods Enzymol. *293*: 300–18.

Stuhmer, W., Conti, F., Suzuki, H., Wang, X., Noda, M., Yahagi, N., et al. (1989). Structural parts involved in activation and inactivation of the sodium channel. Nature *339*: 597–603.

Su, T.P., Su, T.C., Nakamura, Y., and Tsai, S.Y. (2016). The Sigma-1 Receptor as a Pluripotent Modulator in Living Systems. Trends Pharmacol. Sci. *37*: 262–278.

Subbiah, R.N., Clarke, C.E., Smith, D.J., Zhao, J., Campbell, T.J., and Vandenberg, J.I. (2004). Molecular basis of slow activation of the human ether-a-go-go related gene potassium channel. J. Physiol. *558*: 417–31.

Subbiah, R.N., Kondo, M., Campbell, T.J., Vandenberg, J.I., Vandenberg, J., and Chang, V. (2005). Tryptophan scanning mutagenesis of the HERG K + channel: the S4 domain is loosely packed and likely to be lipid exposed. J Physiol *569*: 367–379.

Tammaro, P., Shimomura, K., and Proks, P. (2008). Xenopus Oocytes as a Heterologous Expression System for Studying Ion Channels with the Patch-Clamp Technique. Methods Mol. Biol. Potassium Channels *491*: 127–139.

Tao, X., Lee, A., Limapichat, W., Dougherty, D.A., and MacKinnon, R. (2010). A gating charge transfer center in voltage sensors. Science (80-.). *328*: 67–73.

Tristani-Firouzi, M., Chen, J., and Sanguinetti, M.C. (2002). Interactions between S4-S5 linker and S6 transmembrane domain modulate gating of HERG K+ channels. J. Biol. Chem. *277*: 18994–9000.

Trudeau, M.C., Warmke, J.W., Ganetzky, B., and Robertson, G.A. (1995). HERG, a human inward rectifier in the voltage-gated potassium channel family. Science *269*: 92–5.

Uchihashi, T., Higgins, M.J., Yasuda, S., Jarvis, S.P., Akita, S., Nakayama, Y., et al. (2004). Quantitative force measurements in liquid using frequency modulation atomic force microscopy. Appl. Phys. Lett. *85*: 3575–3577.

Vahabi, S., Nazemi Salman, B., and Javanmard, A. (2013). Atomic Force Microscopy Application in Biological Research: A Review Study. IJMS *38*: 76–83.

Vandenberg, J.I., Perozo, E., and Allen, T.W. (2017). Towards a Structural View of Drug Binding to hERG K+ Channels. Trends Pharmacol. Sci. *38*: 899–907.

Vandenberg, J.I., Perry, M.D., Perrin, M.J., Mann, S.A., Ke, Y., and Hill, A.P. (2012). hERG K(+) channels: structure, function, and clinical significance. Physiol. Rev. *92*: 1393–478.

Vandenberg, J.I., Torres, A.M., Campbell, T.J., and Kuchel, P.W. (2004). The HERG K + channel: progress in understanding the molecular basis of its unusual gating kinetics. Eur Biophys J. *33*: 89–97.

Vandenberg, J.I., Walker, B.D., and Campbell, T.J. (2001). HERG K + channels: Friend and foe. Trends Pharmacol. Sci. *22*: 240–246.

Varghese, A., TenBroek, E.M., Coles, J., and Sigg, D.C. (2006). Endogenous channels in HEK cells and potential roles in HCN ionic current measurements. Prog. Biophys. Mol. Biol. *90*: 26–37.

Wang, W., and MacKinnon, R. (2017). Cryo-EM Structure of the Open Human Ether-à-go-go-Related K+ Channel hERG. Cell *169*: 422–430.

Wang, Z., Dou, Y., Goodchild, S.J., Es-Salah-Lamoureux, Z., and Fedida, D. (2013). Components of gating charge movement and S4 voltage-sensor exposure during activation of hERG channels. J. Gen. Physiol. *141*: 431–43.

Warmke, J.W., Ganetzky, B., Hamilton, B., and Meyerowitz, E. (1994). A family of potassium channel genes related to eag in Drophila and mammals. Neurobiology *91*: 3438–3442.

Yang, C.-W., Hwang, I.-S., Chen, Y.F., Chang, C.S., and Tsai, D.P. (2007). Imaging of soft matter with tapping-mode atomic force microscopy and non-contact-mode atomic force microscopy. Inst. Phys. Publ. Nanotechnol. Nanotechnol. *18*: 1–8.

Yu, S.P., and Kerchner, G.A. (1998). Endogenous voltage-gated potassium channels in human embryonic kidney (HEK293) cells. J. Neurosci. Res. *52*: 612–7.

Zhang, M., Liu, J., Jiang, M., Wu, D.M., Sonawane, K., Guy, H.R., et al. (2005). Interactions between charged residues in the transmembrane segments of the voltage-sensing domain in the hERG channel. J. Membr. Biol. *207*: 169–181.

Zhang, M., Liu, J., and Tseng, G.-N. (2004). Gating charges in the activation and inactivation processes of the HERG channel. J. Gen. Physiol. *124*: 703–18.

Zhang, M., Wang, Y., Jiang, M., Zankov, D.P., Chowdhury, S., Kasirajan, V., et al. (2012). KCNE2 protein is more abundant in ventricles than in atria and can accelerate hERG protein degradation in a phosphorylation-dependent manner. Am. J. Physiol. - Hear. Circ. Physiol. *302*: 910–922.

Zhang, Y.H., Colenso, C.K., Sessions, R.B., Dempsey, C.E., and Hancox, J.C. (2011). The hERG K(+) channel S4 domain L532P mutation: characterization at 37°C. Biochim. Biophys. Acta *1808*: 2477–87.

Zhong, J., and Yan, J. (2016). Seeing is believing: atomic force microscopy imaging for nanomaterial research. RSC Adv. *6*: 1103–1121.

Zhou, P.Z., Babcock, J., Liu, L.Q., Li, M., and Gao, Z.B. (2011). Activation of human ether-a-go-go related gene (hERG) potassium channels by small molecules. In Acta Pharmacologica Sinica, pp 781–788.

Zhou, Z., Gong, Q., Ye, B., Fan, Z., Makielski, J.C., Robertson, G.A., et al. (1998). Properties of HERG channels stably expressed in HEK 293 cells studied at physiological temperature. Biophys. J. *74*: 230–41.